POLITECNICO
MILANO 1863

School of Industrial and Information Engineering
Master of Science in Nuclear Engineering

Modelling and validating fission gas release, pore migration and oxygen redistribution in MOX fuel

Supervisors:

Prof. Lelio Luzzi
Dr. Davide Pizzocri
Tommaso Barani

Thesis by:
Filippo Verdolin Matr.883229

ACADEMIC YEAR 2018-2019

ACKNOWLEDGMENTS

I would like to express my gratitude to all the people who gave a contribution to make this thesis work possible.

First of all I would like to thank my Supervisor, Prof. Lelio Luzzi, for his teachings and the great opportunity he gave me for this work. I am glad for being part of his research group during these months.

I am really grateful to my assistant supervisors, Dr. Davide Pizzocri and Tommaso Barani. They helped me a lot during these month with their professional suggestions, their encouragements and their patience. Their passion for the research rubbed off on me.

I would like to say 'thank you' also to Dr. Stephen Novascone who supervised me during my internship at Idaho National Laboratory (INL) in the U.S. He made me part of his team, teaching me many things and I appreciated it.

I wish to thank Dr. Giovanni Pastore too, for his brilliant suggestions and support during the months spent in the U.S.

I would like to thank also my friend and colleague Riccardo Genoni for providing his useful thesis work in order to generate all the sample images for the study of the bubble equivalent number.

This thesis work was made possible by the collaboration between the Nuclear Reactors Group of the Department of Energy of Politecnico di Milano, the BISON team of Idaho National Laboratory (INL) and the I-NERI initiative. This manuscript has been authored by a contractor of the U.S. Government under Contract DE-AC07-05ID14517. It has been funded by the U.S. Department of Energy – Nuclear Energy Office (DOE-NE) and by the Advanced Fuel Campaign (AFC) of the Nuclear Technology Research and Development Program.

Finally, I would like to thank the most important people of my life: my parents and my brother. I will never be grateful enough. Thank you for having always believed in me and for being close in the most difficult moments. Thanks also to my old friends and to all the friends that I met during these years of journey.

ABSTRACT

The mixed oxide fuels (MOX) are candidate fuels for fast reactors of Generation IV. The conditions achieved in the fast reactors call for the need to investigate and model new, or more emphasized, processes involving the fuel. In this work, some of them will be analyzed and they are: the Fission Gas Release (FGR), the pore migration and the oxygen redistribution. These phenomena are generated or emphasized by the high temperatures and high burnups achieved in fast reactor MOX. In this thesis, I studied the physical limititations of the phenomena that involve the FGR, like the grain-face bubble growth and the consequent coalescence, introducing a lower bound to the number density of grain-face bubbles. These considerations have been extended to the current model for the fission gas behaviour present in the fuel performance code BISON, developed by Idaho National Laboratory (INL), where I spent six months of internship. Hence, this extension to the model has been validated against integral irradiation experiments using BISON. Also the model available in BISON for the pore migration has been validated against irradiation experimental data. It was possible also to validate some cases of offset restructuring. Last, but not least, a model for the oxygen redistribution has been implemented in the code, and it has been validated as well.

The results of the performed validations are encouraging for all the analyzed phenomena, and they can lead to further improvements of the models and specially to more validations.

SOMMARIO

Il combustibile ad ossidi misti di uranio e plutonio MOX (Mixed OXide) è uno dei possibili candidati per i reattori veloci di quarta generazione. Le condizioni raggiunte nei reattori veloci portano alla necessità di investigare e modellare nuovi, o più accentuati, processi che avvengono nel combustibile, se comparati a quanto succede in reattori termici ad acqua leggera. Tra tali fenomeni, quelli che sono analizzati in questo lavoro sono il rilascio dei gas di fissione (FGR), la ristrutturazione del combustibile e la redistribuzione dell'ossigeno. Questi sono tutti fenomeni dovuti o accentuati dagli alti gradienti e livelli di temperatura e di *burnup* raggiunti nelle condizioni operative dai combustibili per reattori veloci. In questa tesi ho studiato alcuni fenomeni fisici che determinano il comportamento dei gas di fissione, in particolare l'evoluzione delle bolle inter-granulari, determinata dalla loro crescita e coalescenza. Il modello considerato ed esteso in questo lavoro è quello disponibile in BISON. Questo è un codice di *performance* del combustibile, sviluppato dall'INL (Idaho National Laboratory) negli Stati Uniti, dove ho trascorso sei mesi di *internship* per questo lavoro. Il modello è stato esteso introducendo una soglia fisica sul minimo numero di bolle inter-granulari ottenibili tramite coalescenza, quindi ho testato e validato il codice BISON rispetto ad esperimenti integrali d'irraggiamento. Per quanto riguarda la ristrutturazione del combustibile, il modello per la migrazione dei pori presente in BISON è stato anch'esso validato rispetto ad esperimenti integrali d'irraggiamento, alcuni dei quali presentavano una ristrutturazione eccentrica e sfalsata rispetto all'asse della barretta di combustibile analizzata. Infine è stato implementato e validato in BISON un modello per la redistribuzione dell'ossigeno. I risultati delle varie validazioni eseguite sono molto incoraggianti per tutti i fenomeni studiati e mettono in luce i miglioramenti ottenuti tramite gli sviluppi modellistici apportati al codice BISON in questo lavoro di tesi.

ESTRATTO IN ITALIANO

Introduzione

Negli ultimi anni lo studio di fenomeni che coinvolgono il combustibile nucleare ha fatto enormi progressi nel settore dei reattori ad acqua leggera, i più impiegati attualmente al mondo. Tuttavia lo sviluppo dei reattori di quarta generazione comporta nuove problematiche rispetto ai reattori ad acqua leggera delle generazioni precedenti. Uno dei combustibili candidati per i reattori veloci, una delle tipologie di questa nuova generazione, è il MOX: ovvero un combustibile ceramico composto da ossido di uranio e di plutonio.
Le condizioni di temperatura e bruciamento (*burnup*) raggiunte nei reattori veloci portano alla necessità di investigare e modellare i nuovi, o più accentuati, processi che avvengono nel combustibile rispetto ai fenomeni normalmente incontrati nel combustibile per reattori termici ad acqua leggera. Tra questi, quelli che verranno analizzati in questo lavoro sono: il rilascio dei gas di fissione (FGR - *fission gas release*), la ristrutturazione del combustibile e la redistribuzione dell'ossigeno. Questi sono tutti fenomeni generati o enfatizzati (per esempio il FGR) dagli alti livelli di temperatura e di *burnup* presenti nel MOX per reattori veloci.
In questa tesi ho studiato alcuni fenomeni fisici che determinano il comportamento dei gas di fissione, in particolare l'evoluzione delle bolle inter-granulari, determinata dalla loro crescita e coalescenza. Il modello considerato ed esteso in questo lavoro è quello proposto da Pastore et al. [36, 37] e disponibile in BISON, un codice di *performance* del combustibile sviluppato dall'Idaho National Laboratory (INL) negli Stati Uniti, dove ho trascorso sei mesi di *internship* per questo lavoro. Alla luce dell'estensione proposta in questa tesi, il codice BISON è stato anche validato rispetto ad esperimenti integrali di irraggiamento in reattore.

Per quanto riguarda la ristrutturazione del combustibile, ho validato il modello di Novascone et al. [32] per la migrazione dei pori presente in BISON, simulando esperimenti di irraggiamento in reattore, alcuni dei quali presentavano una ristrutturazione eccentrica rispetto all'asse della barretta di combustibile analizzata. Quest'ultimi casi

sono stati simulati facendo ricorso alle potenzialità di BISON di poter sfruttare *mesh* non assialsimmetriche.

Infine, in questo lavoro ho implementato in BISON il modello di redistribuzione dell'ossigeno presentato da Lassmann [26], sempre validandolo rispetto ad uno dei casi sperimentali presi in considerazione in questa tesi.
I casi presi in esame in questo lavoro riguardano tutti MOX per reattori veloci al sodio. La barretta di combustibile L09 dell'esperimento FO-2 è il primo caso analizzato. Tale barretta, come illustrato da Gilpin et al. [12] e Teague et el. [45], è stata irraggiata nel reattore veloce americano FFTF (Fast Flux Test Facility) ed in seguito è stata sottoposta a varie analisi sperimentali, tra le quali *puncturing* per la misura del FGR e ceramografie, effettuate a varie altezze della colonna di combustibile, per realizzare studi riguardo alla ristrutturazione.
Un altro caso esaminato riguarda il *test* B14 eseguito nel reattore giapponese JOYO, che essendo di breve durata (appena 68 ore [27]), ha permesso lo studio solamente della migrazione dei pori e la validazione della redistribuzione dell'ossigeno grazie ai dati forniti da Ikusawa et al. [13].
Infine, sono stati analizzati gli esperimenti MK-I e MK-II sempre provenienti dal reattore JOYO per quanto riguardo il rilascio dei gas di fissione, considerando i dati riportati da Shimada et al. [41] e Karahan [16].

Modellazione

Per quanto riguarda il rilascio di gas di fissione, in questa sezione verranno esposte le principali caratteristiche del modello di Pastore et al. [36, 37] per il comportamento dei gas di fissione in combustibile UO_2 per reattori ad acqua leggera. In seguito verranno esposte le problematiche incontrate con combustibili MOX per reattori veloci e, una volta analizzate tali questioni, verranno proposte delle modifiche al modello sulla base dei fenomeni fisici coinvolti.

Secondo il modello di Pastore et al. [36, 37], il primo passaggio del processo che porta al rilascio di atomi di gas di fissione è il loro comportamento all'interno del grano di combustibile. Gli atomi qui generati possono diffondere a bordo grano o dare origine ad una popolazione di bolle (tipicamente nanometriche), con le quali interagiscono tramite i meccanismi di cattura e risoluzione. Il gas che diffonde a bordo grano dà origine ad un'ulteriore popolazione di bolle, responsabile del rigonfiamento gassoso a bordo grano.

La diffusione dei gas di fissione dall'interno del grano di combustibile ai bordi di

grano in geometria sferica e unidimensionale è descritta come segue:

$$\frac{\partial C}{\partial t} = D_{\text{eff}} \frac{1}{r^2} \frac{\partial}{\partial r} \left(r^2 \frac{\partial C}{\partial r} \right) + \beta \tag{E.1}$$

dove C (atomi m^{-3}) è la concentrazione di gas intra-granulare, t (s) il tempo, r (m) la coordinata radiale in geometria sferica, β (atomi m^{-3} s^{-1}) il tasso di generazione di gas, D_{eff} (m^2 s^{-1}) il coefficiente efficace di diffusione del gas [42].

Il fenomeno di crescita (o restringimento) delle bolle sulle facce di grano è descritto da Pastore et al. [36, 37] mutuando il modello di Speight e Beere [43], che identifica nell'assorbimento (o emissione) di vacanze il responsabile di questo evento. Il tasso di assorbimento/emissione di vacanze è calcolato come segue:

$$\frac{dn_v}{dt} = \frac{2\pi D_v \delta_g}{k_B S T} \left(p - p_{\text{eq}} \right) \tag{E.2}$$

dove n_v (vacanze bolla^{-1}) è il numero di vacanze per bolla, D_v (m^2 s^{-1}) è il coefficiente di diffusione delle vacanze nei bordi di grano, δ_g (m) è lo spessore efficace dei bordi di grano ai fini della diffusione, k_B (J K^{-1}) è la costante di Boltzmann, T (K) la temperatura, S (-) è un parametro adimensionale che dipende dalla frazione del grano coperta dalle bolle (*fractional coverage*), p e p_{eq} (Pa), rispettivamente, la pressione del gas nella bolla e la pressione di equilibrio meccanico.

La crescita delle bolle sulle facce di grano induce il processo di coalescenza, cioè porta queste ad intersecarsi ed unirsi, aumentandone le dimensioni e riducendone il numero. Come spiegato da White [48], questo fenomeno è strettamente connesso al tasso di incremento dell'area delle bolle proiettata sulla faccia del grano, A_{gf} (m^2). Questo procedimento è descritto come segue:

$$\frac{dN}{dt} = -2N^2 \left(\frac{dA_{\text{gf}}}{dt} \right) \tag{E.3}$$

dove N (bolle m^{-2}) è il numero di bolle sulla faccia del grano per unità di superficie. Quando le bolle ai bordi di grano diventano abbastanza grandi e numerose, la faccia del grano può essere considerata come percolata e i gas di fissione vengono rilasciati nel volume libero della barra di combustibile. Nel modello di Pastore et al. [36, 37] questo è rappresentato mediante il principio di saturazione delle facce di grano: dopo che il *fractional coverage* $F = NA_{\text{gf}}$ ha raggiunto il livello di saturazione F_{sat}, un'ulteriore crescita delle bolle è compensata dal rilascio di gas in modo da mantenere costante la condizione di saturazione:

$$\begin{aligned} \frac{dn_{\text{fgr}}}{dt} &= 0 \quad \text{if} \quad F < F_{\text{sat}} \\ \frac{dn_{\text{fgr}}}{dt} &= n \frac{N}{A_{\text{gf}}} \frac{dA_{\text{gf}}}{dt} \quad \text{if} \quad F = F_{\text{sat}} \end{aligned}$$

dove n_{fgr} (atomi m^{-2}) è il numero di atomi di gas rilasciati nel volume libero della barretta di combustibile e n_g (atomi bolla^{-1}) il numero di atomi di gas di fissione per bolla sulla faccia di grano.

Dati sperimentali di rilascio dei gas fissione in combustibile irraggiato ad alte temperature e/o alti *burnup* mostrano come questa grandezza possa raggiungere valori molto elevati in tali condizioni (ad esempio, [28, 8]). Questi valori di temperatura e di *burnup* sono spesso raggiunti da combustibili MOX irraggiati in reattori veloci e vanno oltre le normali condizioni di esercizio dei reattori ad acqua leggera.

Il modello presentato da Pastore et al. [36] è stato finora validato solo con casi di UO_2 per reattori ad acqua leggera. Siccome i fenomeni come la crescita delle bolle a bordo grano e la coalescenza sono enfatizzati dalle alte temperature, ci si può aspettare che per combustibili MOX irraggiati in reattori veloci il modello necessiti di alcuni miglioramenti ed ulteriori validazioni. Per quanto riguarda la parte modellistica, si è partiti dalla considerazione che tali processi abbiano un limite fisico. Infatti, la coalescenza porta ad un minor numero di bolle, ma di più grandi dimensioni e la cui crescita è strettamente limitata dalla temperatura (Eq. E.2). Tuttavia il modello di Pastore et al. [36, 37] propone un limite di 10^{10} bolle m^{-2}, che risulta essere eccessivamente basso (e quindi non raggiungibile) sia per le condizioni presenti in reattori ad acqua leggera sia nei casi analizzati in questo lavoro. Per questa ragione, in questo lavoro, è stata proposta una formulazione per dare una descrizione fisica a questo limite. Quindi, il limite del numero di bolle a bordo grano per unità di superficie, N_{lim} (bolle m^{-2}) è:

$$N_{\text{lim}} = \frac{1}{2}\frac{N_{\text{eq}} N_{\text{face}}}{4\pi a^2} \tag{E.4}$$

dove N_{face} (facce grano^{-1}) è il numero medio di facce in un grano (questo valore è circa di 14 facce grano^{-1}), a (m) il raggio del grano sferico equivalente e N_{eq} (bolle faccia^{-1}) il numero medio di bolle su una faccia di grano, chiamato numero equivalente di bolle (*bubble equivalent number*). Per determinare un range ragionevole per N_{eq} è stato eseguito un esperimento numerico con le seguenti caratteristiche:

- Sono state generate 1000 immagini quadrate rappresentative delle facce di grano.
- Per ogni faccia di grano è stata ipotizzata una dimensione di 10x10 μm^2.
- Su ogni faccia di grano, sono stati generati dei cerchi di raggio R, campionati da una distribuzione uniforme $R(\mu\text{m}) \sim \mathcal{U}[0, 1]$.
- In ogni faccia di grano sono stati contati gli agglomerati di cerchi non connessi tra loro, ovvero il numero effettivo di bolle (N_{eq}).

Nella Fig. E.1a, N_{eq} è riportato in funzione del *fractional coverage* F, con ogni punto che rappresenta una delle 1000 immagini generate. Il numero di pori effettivi diminuisce gradualmente con l'aumentare del *fractional coverage*, a causa della formazione di aggregazioni di bolle. Come esempio, Fig. E.1b riporta una delle immagini generate, con un *fractional coverage* $F = 0.43$ e un *bubble equivalent number* $N_{\text{eq}} = 29$.

Dalla Fig. E.1a, in condizioni di saturazione, cioè quando $F = F_{\text{sat}} = 0.5$, N_{eq} giace in un range di 0-20 bolle faccia^{-1}. In questo lavoro, ho assunto $N_{\text{eq}} = 10$. Il fattore 1/2 è introdotto nell'Eq. E.4, perché una bolla su una faccia di grano è condivisa da due grani confinanti. Inoltre può essere notato che N_{lim} proposto in questo lavoro è in accordo con le osservazioni sperimentali [48].

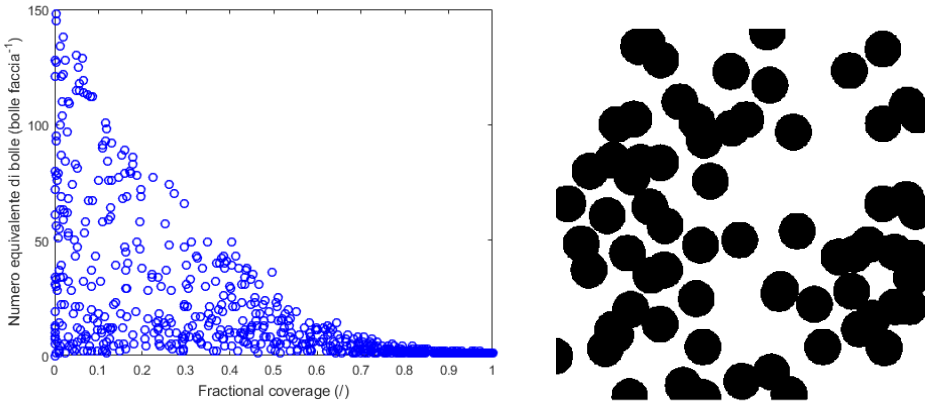

(a) **(b)**

Figure E.1: Risultati dell'esperimento numerico casuale usato per derivare il numero equivalente di bolle per faccia di grano. Sulla sinistra (a) è riportato N_{eq} ottenuto come una funzione del *fractional coverage*, mentre sulla destra (b) è presente una delle immagini generate, con un *fractional coverage* $F = 0.43$ e un *bubble equivalent number* $N_{\text{eq}} = 29$.

Un'altra problematica riscontrata con casi di MOX per reattori veloci riguarda il modello di crescita dei grani di Ainscough et al. [2] implementato in BISON. A causa delle alte temperature raggiunte in questi esperimenti, il modello predice valori non fisici per il raggio dei grani (circa 100 μm). Per via della mancanza di un modello in grado di descrivere la crescita dei grani in queste condizioni, per questo lavoro si è deciso di utilizzare valori costanti per i raggi di grano.

Riguardo al fenomeno della ristrutturazione del combustibile, esso è essenzialmente dovuto alla combinazione di temperature molto elevate (sopra i 1800 K) e

ai forti gradienti termici lungo il raggio delle pastiglie (centinaia di K mm^{-1}) che si verificano nell'esercizio del combustibile ossido nei reattori veloci [33, 35]. In tali condizioni, i pori presenti nel combustibile sono messi in moto e tramite un procedimento di evaporazione/condensazione migrano verso la zona centrale della pastiglia. Questo processo porta al cosiddetto *restructuring* del combustibile, dando luogo a zone contraddistinte da differenti microstrutture. Queste regioni sono caratterizzate da un vuoto centrale, una zona ad altissima densità in cui la microstruttura è composta da grani colonnari in direzione radiale, una regione ad alta densità con grani sferici equiassiali ed infine un'area periferica rimasta invariata rispetto alla stato di fabbricazione.

In questo lavoro sono stati seguiti i passaggi del modello presentato da Novascone et al. [32] per descrivere il fenomeno della migrazione dei pori. In questo modello la migrazione è innescata dal gradiente di temperatura e viene descritta usando un'equazione alle derivate parziali che caratterizza la diffusione dei pori come segue:

$$\frac{\partial P}{\partial t} + \nabla \cdot (P v_P \nabla T - \nu \nabla P) = 0 \tag{E.5}$$

dove T (K) è la temperatura, P (/) è la frazione di porosità, v_P (m^2 s^{-1} K^{-1}) la velocità dei pori, ν (m^2 s^{-1}) è il coefficiente efficace di diffusione dei pori. La velocità dei pori nell'Eq. E.5 usata in questo lavoro si riferisce all'espressione proposta da Sens [40]:

$$v_P = c_0(c_1 + c_2 T + c_3 T^2 + c_4 T^3) T^{-5/2} \times \Delta H p_0 \exp\left(-\frac{\Delta H}{RT}\right) \tag{E.6}$$

dove T (K) è la temperatura e R (J mol^{-1} K^{-1}) è la costante universale dei gas. L'equazione dipende anche dalla pressione di vapore dell'UO_2 p_0 (Pa) e dal calore di vaporizzazione ΔH (J mol^{-1}). I fattori c_1, c_2, c_3 e c_4 sono costanti provenienti da misure sperimentali, riportati in tabella E.1. Nella fonte originale dove viene riportato il modello [32], il gradiente di temperatura viene collassato direttamente nell'espressione della velocità dei pori, mentre qui si sono voluti scrivere separatamente per enfatizzare la dipendenza della migrazione dei pori dal gradiente di temperatura (Eq. E.5).

Table E.1: Lista dei parametri del modello.

Simbolo	Definizione	Valore	u.d.m.	Referenza
c_0	Parametro del modello	5×10^{-16}		[40]
c_1	Parametro del modello	0.988		[40]
c_2	Parametro del modello	6.395×10^{-6}		[40]
c_3	Parametro del modello	3.543×10^{-9}		[40]
c_4	Parametro del modello	3×10^{-12}		[40]
p_0	Pressione di vapore dell'UO_2	33708.5	Pa	[40]
ΔH	Calore di vaporizzazione	5.98×10^{5}	J mol^{-1}	[40]
ν	Coefficiente di diffusione efficace dei pori	1×10^{-12}	m^2 s^{-1}	[32]

Come visto per gli altri processi analizzati, anche la ridistribuzione dell'ossigeno è governata dalla temperatura, sia in termini di valore assoluto sia in termini del suo gradiente. In seguito a questo fatto, alcuni costituenti del combustibile possono muoversi da una regione ad un'altra secondo processi di diffusione allo stato solido. Tra gli elementi interessati da tale fenomeno, l'ossigeno presente nel combustibile ceramico tende a migrare radialmente lungo la pastiglia. Il trasporto di ossigeno è quindi guidato dalla diffusione termica e può occorrere attraverso le vacanze (combustibile ipo-stechiometrico, tipico per i MOX) e gli interstiziali (combustibile iper-stechiometrico).

Nel combustibile per reattori ad acqua leggera, il rapporto di partenza tra atomi di ossigeno (rapporto O/M) e di metallo è prossimo al valore stechiometrico di 2.00. Per MOX veloci questo livello iniziale è leggermente inferiore, perché, in virtù degli alti *burnups* raggiunti in questi reattori, il contenuto di ossigeno nel combustibile aumenta, siccome la fissione può essere considerata come un processo ossidante [44]. In queste condizioni, quando il rapporto O/M aumenta oltre il 2.00, la sovrabbondanza di ossigeno può portare, una volta effettuato il contatto tra combustibile e guaina, alla corrosione della guaina dall'interno [20, 21, 22]. Nonostante ciò, nel modello usato per questo lavoro non verrà considerato l'effetto ossidante dovuto alla fissione.

In questa sezione verranno illustrati i tratti principali del modello di ridistribuzione dell'ossigeno presentato da Lassmann [26] ed implementato in BISON in questo lavoro. La ridistribuzione dell'ossigeno è modellata applicando il concetto di diffusione di Fick e Soret:

$$\frac{\partial c}{\partial t} + \nabla \cdot N_{\text{ox}} D_{\text{ox}} \left(\nabla c + c \frac{Q}{RT^2} \nabla T \right) = 0 \tag{E.7}$$

dove c (/) è la frazione degli atomi interstiziali o delle vacanze di ossigeno, T (K) la temperatura, R (J mol^{-1} K^{-1}) la costante universale dei gas, N_{ox} (atomi m^{-3}) il

numero totale di atomi d'ossigeno per unità di volume, D_{ox} ($m^2\ s^{-1}$) il coefficiente di diffusione degli atomi interstiziali o delle vacanze di ossigeno e Q ($J\ mol^{-1}$) il calore di trasporto molare efficace (*molar effective heat of transport*). Il coefficiente di diffusione proposto da Lassmann [26] è calcolato mediante la seguente correlazione:

$$D_{\mathrm{ox}} = 1.39 \times 10^{-6} \exp \frac{-75900}{RT} \tag{E.8}$$

Siccome c e Q hanno differenti espressioni in base alla stechiometria del combustibile (ipo- o iper-stechiometrico), entrambi i casi verranno descritti. Definendo x la deviazione stechiometrica:

$$\begin{aligned} x &= \frac{O}{U+Pu} - 2 \\ x &= -2c_v \quad \text{(caso ipo-stechiometrico)} \\ x &= c_i \qquad \text{(caso iper-stechiometrico)} \end{aligned} \tag{E.9}$$

c_v e c_i sono le frazioni degli atomi interstiziali e delle vacanze di ossigeno, rispettivamente. Per il caso ipo-stechiometrico il calore di trasporto dell'ossigeno (Eq. E.7) dipende dalla valenza del plutonio V_{Pu}:

$$\begin{aligned} Q_v &= -8.12 \times 10^{-4} exp(4.85 V_{\mathrm{Pu}}) \quad \text{for} \quad V_{\mathrm{Pu}} < 3.3 \\ Q_v &= -3.96 \times 10^{6} + 2.37 \times 10^{6} V_{\mathrm{Pu}} - 3.6 \times 10^{5} V_{\mathrm{Pu}}^2 \quad \text{per} \quad 3.3 \leq V_{\mathrm{Pu}} < 4.0 \end{aligned} \tag{E.10}$$

V_{Pu} è la valenza media degli ioni di plutonio e può essere descritta come:

$$V_{\mathrm{Pu}} = 4 + 2 \cdot \frac{x}{q} = 4 - 4 \cdot \frac{c}{q} \tag{E.11}$$

dove q (/) è il rapporto tra plutonio e atomi di metallo pesante. Questo termine è definito da Karahan [16] come:

$$q = \frac{q_0}{1 - Bu} \tag{E.12}$$

dove q_0 (/) è il rapporto iniziale tra plutonio e atomi di metallo pesante e Bu (FIMA) il *burnup*. Nel caso iper-stechiometrico il calore di trasporto dell'ossigeno è funzione della valenza di uranio V_U:

$$Q_i = -3.5 \times 10^{34} exp(-17 V_U) \quad \text{per} \quad V_U \geq 4.0 \tag{E.13}$$

V_U è la valenza media degli ioni di uranio e può essere descritta come:

$$V_U = 4 + 2 \cdot \frac{x}{1 - q} = 4 + 2 \cdot \frac{c}{1 - q} \tag{E.14}$$

Risultati

In questa Sezione verranno esposti i risultati delle validazioni dei modelli riguardanti i fenomeni analizzati.

Per il FGR sono presentati i risultati delle validazioni eseguite simulando con BISON gli esperimenti FO-2 del reattore americano FFTF, MK-I e MK-II del reattore giapponese JOYO. Entrambi sono reattori veloci al sodio e il combustibile utilizzato è di tipo MOX. Come mostrato nella Fig. E.2 sono stati esaminati due differenti casi:

- Nel primo viene considerata la versione attuale di BISON, senza alcuna limitazione[1] sui processi di crescita delle bolle e di coalescenza;
- Nel secondo, invece, sono riportate le simulazioni eseguite tenendo conto del limite inferiore per il numero di bolle a bordo grano N_{lim} (Eq. E.4), dipendente dal raggio del grano e proposto in questo lavoro, con il coefficiente di diffusione per i gas di fissione presentato da Turnbull et al. [15].

La Fig. E.2 mostra che introducendo N_{lim}, secondo l'Eq. E.4, la previsione del rilascio di gas di fissione si avvicina di più ai dati sperimentali. Infatti senza questo limite ai bordi di grano si vanno a formare poche bolle e di dimensioni eccessive, riducendo così drasticamente il livello di rilascio di gas. Questi risultati sono quindi in accordo con quanto aspettato, perché la limitazione introdotta descrive meglio il limite fisico di questi processi che occorrono durante le condizioni operative di reattori veloci utilizzanti combustibile MOX.

[1] Per semplicità, in questo lavoro ci si riferisce con "BISON senza alcuna limitazione" alla versione standard di BISON avente il limite di 10^{10} bolle m^{-2} [37]. Questa decisione è stata presa perché tale limite non è mai stato raggiunto in nessuno dei casi analizzati.

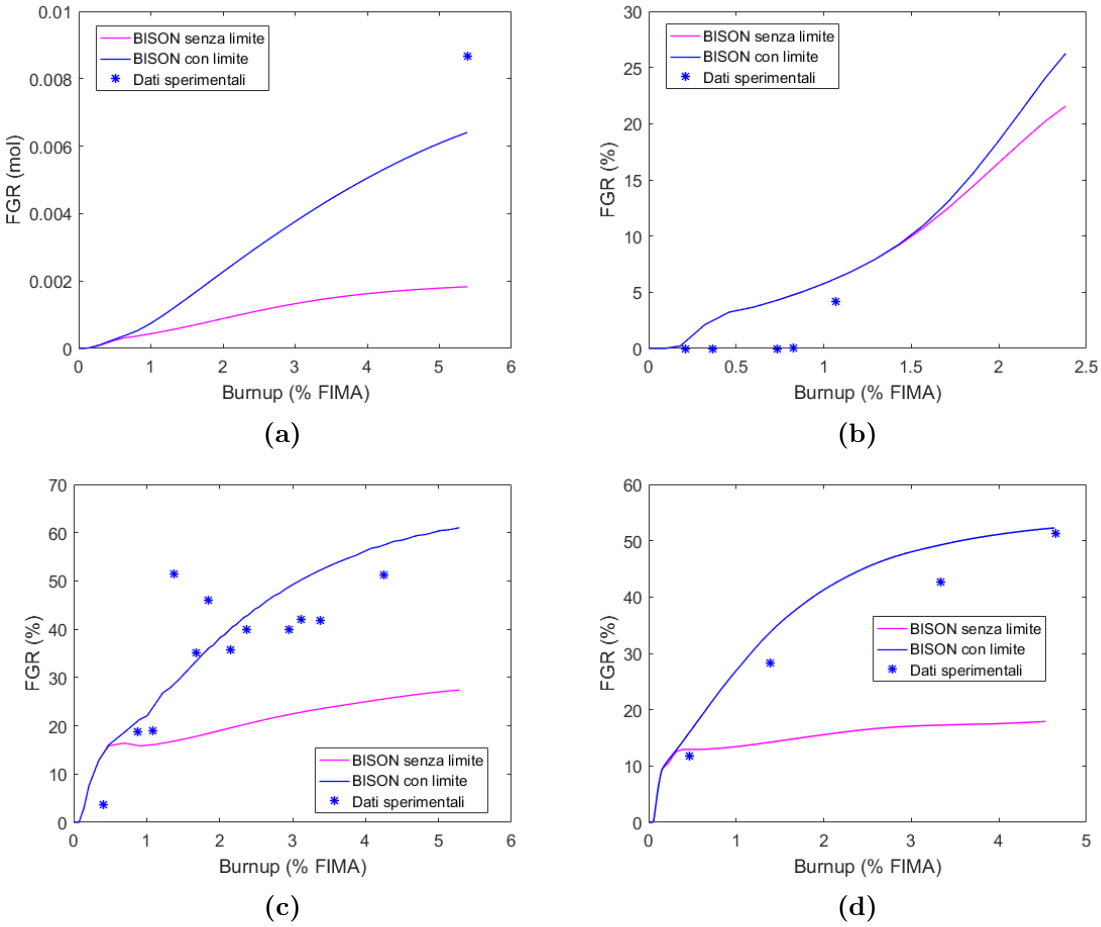

Figure E.2: Risultati per il rilascio di gas di fissione. In ogni figura sono esposti i due casi analizzati: quello relativo alla versione attuale di BISON (linea porpora) e quello considerante il limite introdotto nell'Eq. E.4 (linea blu). I risultati sono così suddivisi: in (a) quelli per la barretta L09; in (b) e (c) per l'esperimento MK-I a 50 MW e a 75 MW, rispettivamente; ed infine in (d) quelli riguardanti il nocciolo MK-II.

Il modello di migrazione dei pori è stato validato simulando con BISON gli esperimenti di irraggiamento FO-2 del reattore americano FFTF e B14 del reattore giapponese JOYO, e così predicendo la formazione del vuoto centrale. La Fig. E.3 mostra il confronto di tutti i campioni (sia quelli soggetti alla tomografia computerizzata a raggi X ($X - ray\ CT$) che soggetti ad analisi distruttive) con i risultati delle simulazioni in un intervallo di $\sigma \pm 20\%$. In queste simulazioni ho voluto studiare l'impatto sui risultati che ha la soglia di porosità per considerare un vuoto come

tale. La Fig. E.3a si riferisce alla stessa soglia usata da Novascone et al. [32] ($P > 0.3$); mentre nella Fig. E.3b è stata usata $P > 0.75$. Si può osservare che tra i due risultati non ci sono molte differenze in quanto il gradiente di porosità è molto ripido nel bordo tra vuoto centrale e zona ristrutturata. Tuttavia, siccome la condizione $P > 0.75$ rispecchia di più i dati sperimentali, è stato deciso di utilizzarla in tutte le seguenti simulazioni.

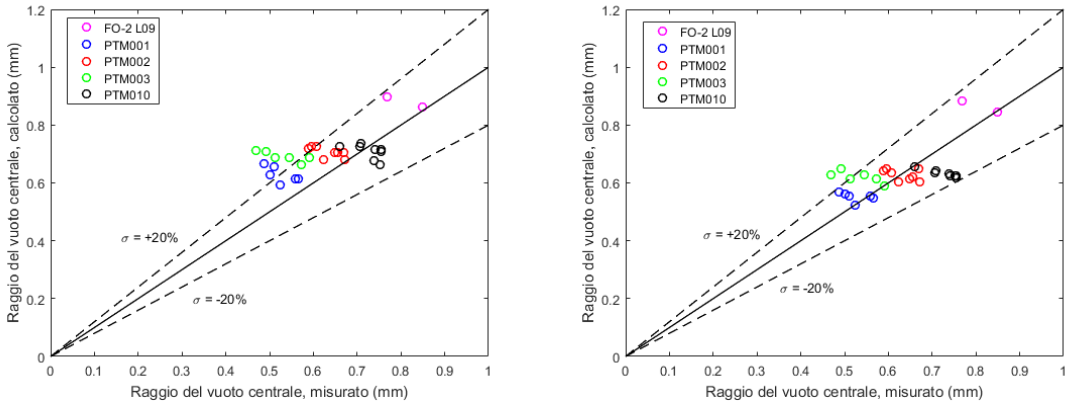

Figure E.3: Raggio del vuoto centrale (mm) misurato verso calcolato per gli esperimenti FO-2 e B14. Entrambe le figure mostrano tutti i campioni (sia quelli soggetti alla tomografia computerizzata a raggi X che soggetti ad analisi distruttive) confrontati con i risultati delle simulazioni in un intervallo di $\sigma \pm 20\%$. L'impatto sui risultati che ha la soglia di porosità per considerare un vuoto come tale, è stato analizzato come segue: la Fig. (a) si riferisce alla stessa soglia usata da Novascone et al. [32] ($P > 0.3$); mentre (b) utlizza $P > 0.75$ come soglia.

Nella Fig. E.4 è possibile osservare il gradiente di porosità. In figura è segnata, in base alle misure fornite da Gilpin et al. [12], anche la delimitazione tra la regione ristrutturata e quella invariata. La linea nera tratteggiata si riferisce alla misura sperimentale del vuoto centrale, mentre quella rossa tratteggiata delimita la regione ristrutturata da quella invariata. Come mostrato in queste figure, riferite alla fine fine di ogni simulazione, BISON sembra descrivere questo fenomeno con buoni risultati. Come ci si aspettava, il profilo di porosità è coerente col gradiente di temperatura a cui fa riferimento (Fig. E.4b).

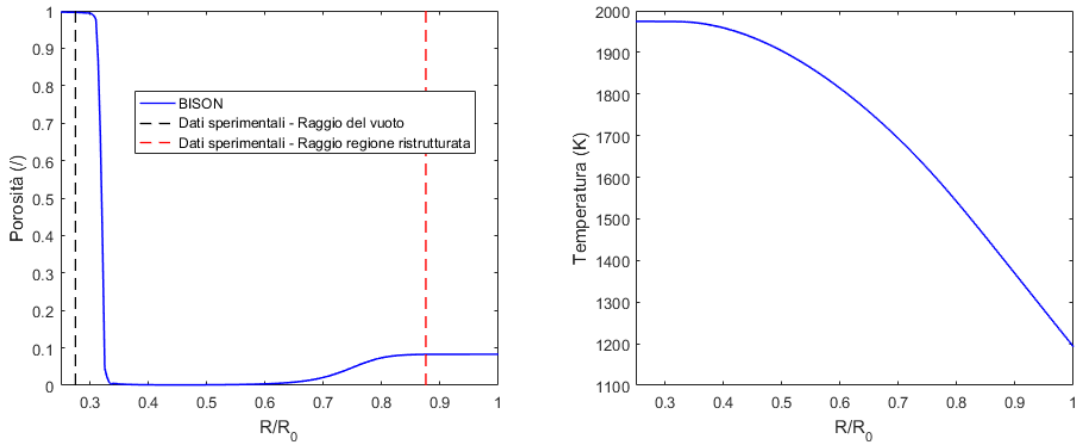

(a) **(b)**

Figure E.4: Risultati della simulazione integrale della barretta L09. I profili di porosità (a) e temperatura (b), rispetto alla dimensione radiale relativa, si riferiscono al campione H (mezzeria). R_0 indica il raggio esterno della pastiglia. La linea nera tratteggiata si riferisce alla misura sperimentale del vuoto centrale (raggio interno pre-irraggiamento è 0.685 mm). La linea rossa tratteggiata, invece, delimita la regione ristrutturata da quella invariata [12]. Ogni curva inizia dal raggio interno del combustibile anulare.

Come mostrato dalle ceramografie dell'esperimento B14 riportate da Maeda et al. [27] le barrette con un'intercapedine tra guaina e combustibile (*gap*) iniziale maggiore (PTM002 e PTM010) presentano una ristrutturazione eccentrica nei campioni presi dalla parte superiore della colonna di combustibile (Fig. 5.3d and Fig. 5.3h). In modo da riprodurre questo effetto con BISON, è stata utilizzata una griglia di calcolo (*mesh*) bidimensionale avente una forma di metà disco. Per evitare problemi di convergenza, è stato necessario rifinire di molto la *mesh* riguardante il combustibile (50 elementi nella direzione radiale e 200 in quella tangenziale).

La Fig. E.5 mostra i risultati delle simulazioni per riprodurre il vuoto centrale fuori dall'asse delle barrette PTM002 e PTM010.

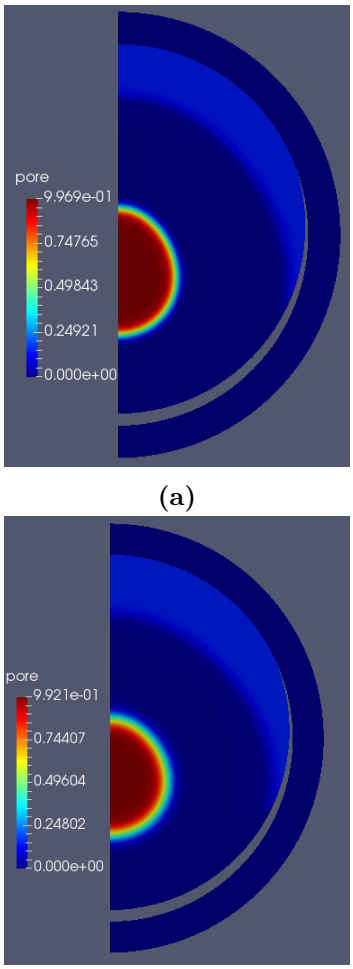

Figure E.5: Risultati dei casi di $offset$ per le barrette PTM002 (a) e PTM010 (b) nelle sezioni a +97 mm e a +99 mm dalla mezzeria dell'altezza attiva, rispettivamente. Entrambe le figure mostrano il profilo di porosità nel combustibile dopo la ristrutturazione.

La Tabella E.2 mostra il confronto tra valori misurati e calcolati per l'$offset$ del vuoto centrale per le barrette PTM002 e PTM010. L'eccentricità dal foro centrale è stata normalizzata rispetto al diametro del combustibile e si può osservare che il modello predice in maniera soddisfacente la dimensione del vuoto, ma l'entità della sfasatura dal centro necessita di ulteriori studi.

Table E.2: $Offset$ del vuoto centrale per le barrette PTM002 e PTM010: misurato verso calcolato.

		PTM002	PTM010
Misurato	Diametro del vuoto centrale (mm)	1.19	1.32
	Offset/Diametro del combustibile (/)	0.03	0.035
Calcolato	Diametro del vuoto centrale (mm)	1.249	1.31
	Offset/Diametro del combustibile (/)	0.08	0.085

Riguardo alla ridistribuzione dell'ossigeno, dopo aver implementato in BISON il modello descritto da Lassmann [26], si è deciso di testarlo con due semplici esempi unidimensionali, in modo da considerare entrambi i casi possibili di combustibile (ipo- e iper-stechiometrico).
La Fig. E.6 mostra il risultato dei due esempi: il primo riguardante un combustibile ipo-stechiometrico (Fig. E.6a, tipico per un MOX) e il secondo rispetto ad un caso iper-stechiometrico (Fig. E.6b). In queste simulazioni è stato utilizzato un tipico valore per un MOX impiegato in reattori veloci per la frazione iniziale di plutonio q_0, corrispondente a 25 Pu/(U+Pu) at%. Le figure mostrano un comportamento molto simile a quello previsto dalla letteratura [33].

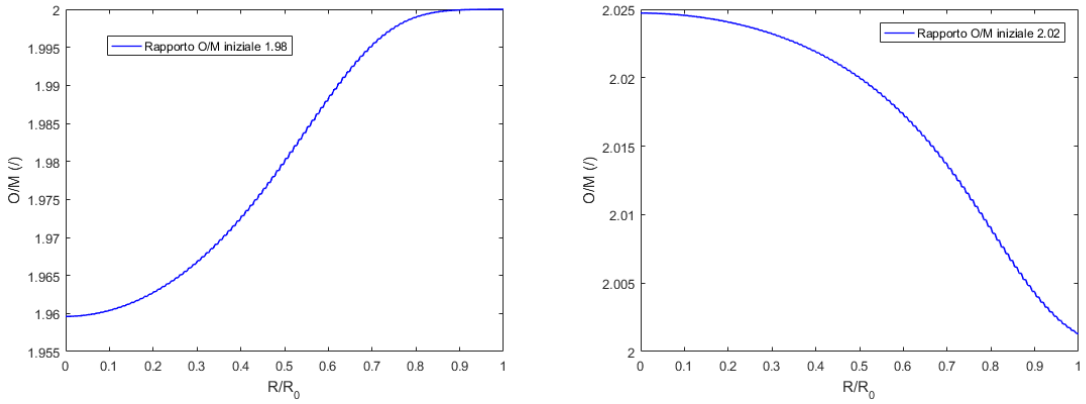

(a) **(b)**

Figure E.6: (a) Caso iper-stechiometrico (O/M>2); (b) caso ipo-stechiometrico (O/M<2). In entrambi gli esempi è stato considerata una pastiglia solida con un q_0 pari a 25 Pu/(U+Pu) at%.

In tutti gli esperimenti analizzati finora in questo lavoro solo il *test* B14 fornisce dati utili [13] per una validazione del modello di redistribuzione dell'ossigeno. Questi risultati sono mostrati nella Fig. E.7. Siccome i pochi dati provenienti da Ikusawa et al. [13] confrontano il rapporto O/M con il potenziale dell'ossigeno, per eseguire questa validazione è necessario estrapolare il potenziale dell'ossigeno dalle simulazioni. Per conseguire a questo compito si è presa in considerazione la seguente equazione, fornita da Kato et al. [19] che mette in relazione il rapporto O/M con la pressione parziale dell'ossigeno p_{O_2}:

$$O/M = 2 + \left[exp\left(-\frac{22.8 + 84.5 C_{Pu}}{R} \right) exp\left(\frac{105000}{RT} \right) (p_{O_2})^{1/2} \right] - K^{-1/5} \qquad \text{(E.15)}$$

dove il terzo termine K è definito come:

$$K = \left\{ exp\left(\frac{44 + 55.8C_{\mathrm{Pu}}}{R}\right) exp\left(-\frac{376000}{RT}\right) (p_{\mathrm{O_2}})^{-1/2} \right\}^{-5} + \left\{ \left[exp\left(\frac{68.8 + 131.3C_{\mathrm{Pu}}}{R}\right) exp\left(-\frac{515000}{RT}\right) \right]^{1/2} (p_{\mathrm{O_2}})^{-1/4} \right\}^{-5} + \left\{ \left[2exp\left(\frac{153.5 + 96.5C_{\mathrm{Pu}} + 331C_{\mathrm{Pu}}^2}{R}\right) exp\left(-\frac{891000}{RT}\right) \right]^{1/3} (p_{\mathrm{O_2}})^{-1/3} \right\}^{-5} + \left\{ \left[exp\left(\frac{111.2 + 20C_{\mathrm{Pu}}}{R}\right) exp\left(-\frac{445000}{RT}\right) \right]^{1/2} (p_{\mathrm{O_2}})^{-1/4} \right\}^{-5} + \left(\frac{C_{\mathrm{Pu}}}{2}\right)^{-5}$$

Nelle Eqs. E.15-E.16 T (K) è la temperatura, R (J mol^{-1} K^{-1}) la costante universale dei gas e C_{Pu} il contenuto di plutonio, definito come:

$$C_{\mathrm{Pu}} = \frac{Pu}{U + Pu + Am} + 2.5\frac{Am}{U + Pu + Am} \tag{E.16}$$

Infine, per calcolare il potenziale dell'ossigeno $\Delta\overline{G}_{\mathrm{O_2}}$ (J mol^{-1}), si può considerare la seguente formulazione:

$$\Delta\overline{G}_{\mathrm{O_2}} = RTln\left(p_{\mathrm{O_2}}\right) \tag{E.17}$$

Nella Fig. E.7, in accordo con Ikusawa et al. [13], sono stati presi in considerazione due tipi di combustibile MOX: il primo contenente americio (66 wt% of U, 31.6 wt% of Pu and 2.4 wt% of Am) e l'altro con solo uranio e plutonio (70 wt% of U and 30 wt% of Pu).

I due risultati, ottenuti con BISON e mostrati nella Fig. E.7 (cerchio verde e cerchio nero), si riferiscono a due campioni posti ad un raggio normalizzato di 0.33 ad una temperatura di 1673 K (la stessa dell'esperimento eseguito da Ikusawa et al. [13]).
I risultati sono coerenti con i dati sperimentali (Fig. E.7) perchè la simulazione eseguita con il combustibile contenente americio presenta un valore più elevato di potenziale di ossigeno, visto che questo attinide minore tende ad incrementare questo parametro. Questa caratteristica può essere osservata anche guardando l'Eq. E.16.

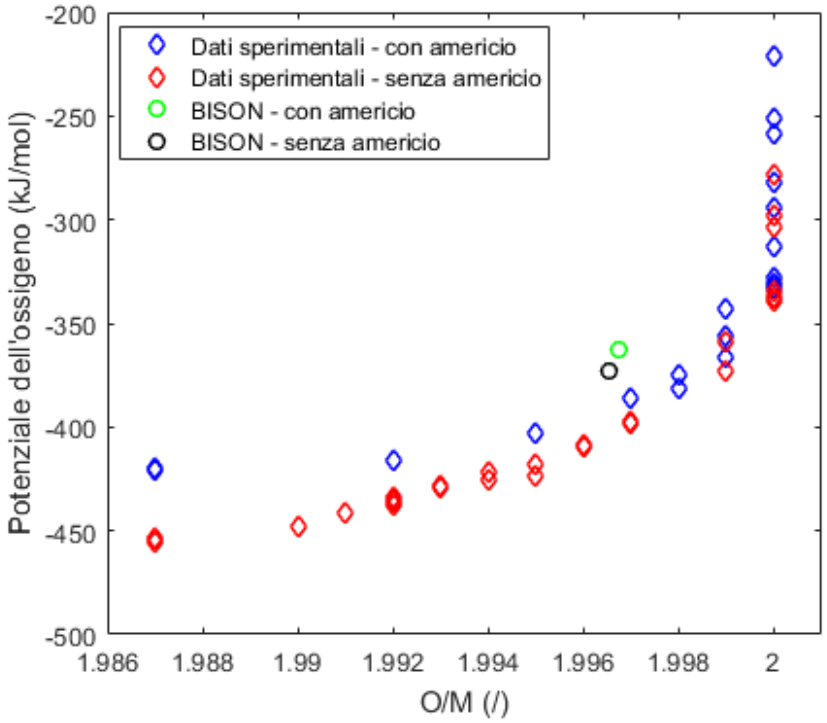

Figure E.7: Risultati per il potenziale d'ossigeno nell'esperimento B14 e validazione del modello di redistribuzione dell'ossigeno implementato in BISON con i dati provenienti da Ikusawa et al. [13]. Sono stati presi in considerazione due tipi di combustibile MOX: il primo contenente americio (66 wt% of U, 31.6 wt% of Pu and 2.4 wt% of Am) e l'altro con solo uranio e plutonio (70 wt% of U and 30 wt% of Pu).

Conclusioni e sviluppi futuri dei modelli

In questo lavoro ho analizzato tre importanti fenomeni che avvengono nel combustibile MOX sotto le rigide condizioni operative dei reattori veloci.

Per il rilascio di gas di fissione ho proposto un'estensione al corrente modello presente in BISON. Quindi ho focalizzato il mio lavoro sull'implementazione di questo miglioramento nel codice e alla sua seguente validazione rispetto esperimenti di irraggiamento.
I risultati ottenuti con il limite proposto nel'Eq. E.4 sono incoraggianti. Ciò è confermato dalle validazioni integrali di combustibile MOX per reattori veloci analizzate

in questo lavoro.
I prossimi sforzi possono essere investiti nella validazione di nuovi casi e in un ulteriore miglioramento al modello di Pastore et al. [36, 37]. Per esempio, in futuro si potrebbe tener conto dell'effetto dell'eterogeneità dei combustibili MOX, dovuto alla presenza di agglomerati di plutonio, sul rilascio di gas. Questo potrebbe essere fatto integrando, al presente modello, gli studi di Koo et al. [24] e di Ishida e Korei [14]. Inoltre, potrebbe essere necessario lo sviluppo che permetta la descrizione della crescita dei grani ad elevate temperature, soprattutto per definire la regione dei grani colonnari. Finora i grani sono sempre stati considerati come sfere, ma questa approssimazione è valida solo per la regione più esterna e per quella caratterizzata da grani equiassiali.

Per quanto riguarda la ristrutturazione, il lavoro si è focalizzato principalmente sulla validazione. Il modello di Novascone et al. [32] attualmente implementato in BISON non era mai stato validato rispetto ad esperimenti integrali di irraggiamento. Inoltre ho avuto l'occasione di analizzare il comportamento del modello di fronte ad un caso di ristrutturazione eccentrica e sfalsata rispetto all'asse di simmetria della barretta. I risultati mostrati dalla Fig. E.3 sono promettenti. A causa del ripido gradiente di porosità che delimita la regione del vuoto centrale (Fig. E.4), è necessario utilizzare *mesh* ad alta densità e ciò è una grande limitazione al modello di elementi finiti utilizzato. Inoltre, essendo stata la validazione della ristrutturazione eccentrica solo un primo tentativo, i risultati sembrano molto incoraggianti. Il modello è in grado di predire in maniera soddisfacente la dimensione del vuoto, ma l'entità dello sfalsamento dal centro necessita di ulteriori studi (Tabella E.2). Come prospettiva futura, potranno essere investigate altre correlazioni per la velocità dei pori, in quanto è una delle quantità analizzate più soggetta ad incertezza, per poi essere confrontati con i risultati ottenuti con la correlazione data da Sens [40] usata in questo lavoro.

Per la ridistribuzione dell'ossigeno BISON necessitava di un modello in grado di descrivere questo fenomeno. Ho concentrato i miei sforzi nell'implementare il modello di Lassmann [26] all'interno del codice. Dopo averlo testato in semplici esempi monodimensionali, l'ho validato rispetto ai dati provenienti dall'esperimento B14 [13]. La maggior difficoltà incontrata in questo ambito è stata trovare dati sperimentali utili alla validazione, ciononostante questo primo tentativo è incoraggiante ed utile ai fini di ulteriori investigazioni. Inoltre, in vista di future prospettive, l'Eq. E.7 può essere migliorata tenendo conto di altri due termini:

- Un termine sorgente s (atomi m^{-3} s^{-1}) che considera la fissione di uranio e plutonio come un processo ossidante, siccome i prodotti di fissione non possono legare tutti gli atomi di ossigeno liberati;

- Un termine J (atomi m^{-2} s^{-1}) che rappresenti il flusso di ossigeno dal combustibile alla guaina, siccome quando avviene il contatto chimico tra i due, l'ossigeno (e altri prodotti di fissione) possono penetrare nella guaina dall'interno.

Quindi dopo queste considerazioni, anche esposte da Kleykamp [20, 21, 22], l'Eq. 3.8 diverrebbe:

$$\frac{\partial c}{\partial t} + \nabla \cdot N_{\mathrm{ox}} D_{\mathrm{ox}} \left(\nabla c + c \frac{Q}{RT^2} \nabla T \right) - \nabla J \left(T_{\mathrm{clad}}, Bu \right) + s \left(T, Bu \right) = 0 \qquad \text{(E.18)}$$

Contents

List of Tables

List of Figures

Figure Page

List of acronyms

AFC Advanced Fuel Campaign

CT Computed Tomography

DOE Department Of Energy

EFPD Equivalent Full Power Days

FFTF Fast Flux Test Facility

FIMA Fissions per Initial Metal Atoms

FGR Fission Gas Release

FR Fast Reactor

I-NERI International Nuclear Energy Research Initiative

INL Idaho National Laboratory

LWR Light Water Reactor

MAMOX Minor Actinide MOX

MOX Mixed OXide

O/M Oxygen-to-Metal

SCRAM Safety Control Rod Ax Man

SGHWR Steam Generating Heavy-Water Reactor

UKAEA UK Atomic Energy Authority

UO_2 Uranium Dioxide

US United States

List of symbols

A_{gf}	Grain-face bubbles projected area (m^2)
a	Spherical grain radius (m)
b	Resolution parameter (s^{-1})
Bu	Burnup (FIMA)
C	Intra-granular gas concentration (as single atoms and in the bubbles) (atoms m^{-3})
C_{Pu}	Plutonium content (/)
c	Atomic fraction of interstitial atoms or oxygen vacancies (/)
c_i	Atomic fraction of interstitial oxygen atoms (/)
c_v	Atomic fraction of oxygen vacancies (/)
D	2-dimensional (linear intercept) average grain diameter (μm)
D_1	First term of Turnbull single atom diffusion coefficient ($\mathrm{m}^2\ \mathrm{s}^{-1}$)
D_2	Second term of Turnbull single atom diffusion coefficient ($\mathrm{m}^2\ \mathrm{s}^{-1}$)
D_3	Third term of Turnbull single atom diffusion coefficient ($\mathrm{m}^2\ \mathrm{s}^{-1}$)
D_{eff}	Effective gas diffusion coefficient ($\mathrm{m}^2\ \mathrm{s}^{-1}$)
D_m	Limiting grain size (μm)
D_{ox}	Diffusion coefficient of interstitial atoms or oxygen vacancies ($\mathrm{m}^2\ \mathrm{s}^{-1}$)
D_s	Single atom diffusion coefficient ($\mathrm{m}^2\ \mathrm{s}^{-1}$)
D_v	Vacancy diffusion coefficient in grain boundaries ($\mathrm{m}^2\ \mathrm{s}^{-1}$)
E	Young's modulus (Pa)

F	Fractional coverage (/)
F_{sat}	Saturation fractional coverage (/)
g	Trapping parameter (s^{-1})
J	Flux of oxygen term (atoms m^{-2} s^{-1})
k	Rate constant of the model (μm^2 h^{-1})
k_B	Boltzmann constant (J K^{-1})
N	Number density of grain-face bubbles per unit surface (bubbles m^{-2})
N_{eq}	Bubble equivalent number (bubbles $face^{-1}$)
N_{face}	Average number of faces in a grain (face $grain^{-1}$)
N_{lim}	Lower limit for the bubble number density at the grain boundary (bubbles m^{-2})
N_{ox}	Total number of oxygen atoms per unit volume (atoms m^{-3})
n	Number of fission gas atoms per bubble (atoms $bubble^{-1}$)
n_{fgr}	Number of gas atoms released to the fuel rod free volume (atoms m^{-2})
n_v	Number of vacancies per bubble (vacancies $bubble^{-1}$)
P	Fractional porosity (/)
p	Grain-face bubble pressure (Pa)
p_0	UO_2 vapor pressure (Pa)
p_{eq}	Grain-face bubble equilibrium pressure (Pa)
p_{O_2}	Oxygen partial pressure (atm)
Q	Molar effective heat of transport (J mol^{-1})

Q_i	Heat of transport of the oxygen interstitial atoms (J mol^{-1})
Q_v	Heat of transport of the oxygen vacancies (J mol^{-1})
q	Fraction of plutonium (/)
q_0	Initial fraction of plutonium (/)
R	Universal gas constant (J $mol^{-1}K^{-1}$)
r	Radial co-ordinate in the spherical geometry (m)
S	Model parameter (-)
s	Oxygen source term (atoms m^{-3} s^{-1})
T	Temperature (K)
T_{clad}	Cladding temperature (°C)
t	Time (s)
V	Fuel volume (m^3)
V_{gf}	Grain-face bubble volume (m^3)
V_{Pu}	Average valence of plutonium ions (-)
V_U	Average valence of uranium ions (-)
$\vec{v}$	Pore velocity (m s^{-1})
x	Deviation from stoichiometry (-)
α	Thermal expansion coefficient (K^{-1})
β	Gas generation rate (atoms m^{-3} s^{-1})

$\Delta\overline{G}_{O_2}$	Free energy of formation of oxygen in the fuel (J mol^{-1})
ΔH	Heat of vaporization (J mol^{-1})
$\Delta V/V$	Fuel swelling (/)
δ_g	Thickness of diffusion layer in grain boundaries (m)
ν	Poisson's ratio (-)
ν_p	Effective porosity diffusion coefficient (m^2 s^{-1})
Ω	Atomic (vacancy) volume (m^3)
ω	Van der Waals covolume of fission gas atom (m^3)

CHAPTER 1. INTRODUCTION

Mixed Oxide fuels (MOX) – uranium and plutonium mixed oxide fuels – are already used in many Light Water Reactors (LWRs) in France and probably they will be also widely utilized in the Generation IV Fast Reactors (FRs) in the next years. Nowadays, a lot of experience has been already achieved with the most classic oxide fuel, the Uranium Dioxide (UO_2), but a wider knowledge about the MOX fuels is required. For this purpose, in the last years, many experiments have been performed on MOX fuels in test fast reactors around the world.
This kind of fuel has been already studied and used in commercial LWRs and it will be taken advantage more efficiently in Generation IV fast reactors thanks to its higher burn-up potential. Also, being a ceramic fuel, it has high melting point, but a low thermal conductivity.
In fast reactors, the MOX fuels are subjected to harsh operative conditions, namely: high temperatures, that could be above 2000 K and high burnup, that could reach values of 10% (Fissions per Initial Metal Atoms) FIMA.
Due to those extreme conditions new phenomena take place in the ceramic fuel, which usually do not occur in the LWRs due to their lower temperatures and burnup [10, 28, 39]. These phenomena could have many different effects on the fuel performance. In this work, I will analyze (i) the enhancement of the fission gas release (FGR), (ii) the restructuring and the consequent central void formation, and (iii) the oxygen redistribution.
In this thesis, I studied the physical limitations of the phenomena that involve the FGR, like the grain-face bubble growth and the coalescence. These considerations have been extended to the model for the fission gas behaviour presented by Pastore et al. [36, 37]. This feature has been, in the first instance, tested against the UKAEA Winfrith SGHWR database (UK Atomic Energy Authority, Steam Generating Heavy-Water Reactor), by Baker [5, 6]. Afterwards, this extension has been validated against integral irradiation experiments using the American fuel performance code BISON. This code has been developed by Idaho National Laboratory (INL), where I spent six months of internship.

Regarding the pore migration, I validated against integral irradiation experiments the model presented by Novascone et al. [32]. It was possible also to validate some cases of offset restructuring.

Lastly, I implemented in the BISON code and validated also the model presented by Lassmann [26] for the oxygen redistribution.
All the cases taken into account for integral validations concern sodium fast reactors. The fuel pin L09 from the FO-2 experiment is the first case analyzed. This rod, as explained by Gilpin et al. [12] and Teague et al. [45], has been irradiated in the

American reactor FFTF (Fast Flux Test Facility). It has been punctured, in order to let the FGR analysis, and afterwards cut at three elevations to perform ceramographies for the restructuring study. Another examined case is the B14 test, performed in the Japanese reactor JOYO. Since the irradiation time of this experiment was very short (just 68 hours [27]), it was possible (thanks to the data from Ikusawa et al. [13]) to focus the study only on the pore migration and on the oxygen redistribution, neglecting the fission gas release effects. The last experiments concern the MK-I and MK-II cores irradiated in the JOYO reactor. Shimada et al. [41] and Karahan [16] provide all the data useful for the validation of the fission gas release.

The thesis is organized as follows: Chapters 2, 3 and 6 are subdivided in three sections: the first one for the fission gas release, the second one for the pore migration, and the last one for the oxygen redistribution.
In Chapter 2, the current models and definitions of these three phenomena are illustrated, while in Chapter 3, I present the development of these models.

The modified model for the fission gas release is tested in LWR conditions to demonstrate the maintained predictive capability of the modified model in these conditions (Chapter 4).

All the integral irradiation experiments are detailed in Chapter 5 and the models for the discussed phenomena are validated against those experiments in Chapter 6. The main conclusions are drawn in Chapter 7.

1.1 The BISON code

BISON [50] is a finite-element based, engineering-scale nuclear fuel performance code developed at the Idaho National Laboratory (INL, USA). The code is applicable to both steady and transient fuel behavior, and can be used to analyze 1D spherically symmetric, 2D axisymmetric or 3D geometries. The governing relations of BISON consist of fully-coupled partial differential equations for thermo-mechanics and species conservation, and include constitutive laws for both nonlinear kinematics and nonlinear material behavior.

CHAPTER 2. PHYSICAL PHENOMENA ANALYZED

In this Chapter, the main features of the three physical phenomena taken into account (fission gas release, pore migration and oxygen redistribution) are analyzed.

2.1 Fission gas release

Fission gas atoms generated in the fuel grains diffuse towards the grain boundaries through repeated trapping in and irradiation-induced resolution from nanometer-size intra-granular gas bubbles [36, 37]. Although a part of the gas atoms that reach the grain boundaries is dissolved back to the grain interior by irradiation, the majority of the gas diffuses into grain-face gas bubbles, giving rise to grain-face swelling. Bubble growth brings about bubble coalescence and inter-connection, eventually leading to the formation of a tunnel network through which a fraction of the gas is released to the fuel rod free volume.

2.1.1 Diffusion based model

The model, developed by Pastore et al. [36, 37], incorporates the fundamental features of fission gas behavior, among which are gas diffusion and precipitation in grains, growth and coalescence of gas bubbles at grain faces, thermal, athermal, steady-state, and transient gas release. Through a direct description of the grain-face gas bubble development, the fission gas swelling and release are calculated as inherently coupled processes, on a physical basis.

Fission gas diffusion [36, 37] from within the fuel grain (assumed as spherical) to the grain boundary in one-dimensional spherical geometry is described as follows:

$$\frac{\partial C}{\partial t} = D_{\text{eff}} \frac{1}{r^2} \frac{\partial}{\partial r} \left(r^2 \frac{\partial C}{\partial r} \right) + \beta \tag{2.1}$$

where C (atoms m^{-3}) is the intra-granular gas concentration (as single atoms and in the bubbles), t (s) is the time, r (m) is the radial co-ordinate in the spherical geometry, β (atoms m^{-3} s^{-1}) is the gas generation rate, D_{eff} (m^2 s^{-1}) is the effective gas diffusion coefficient [42, 36, 37]. The diffusion coefficient D_{eff} is given by: the intra-granular

gas atom diffusion coefficient D_s (m^2 s^{-1}); the rate of gas atom trapping into intragranular bubbles g (s^{-1}) (trapping parameter) and by the rate of gas atom resolution from bubbles back into the lattice b (s^{-1}) (resolution parameter); and it is expressed with the following relationship:

$$D_{\text{eff}} = \frac{b}{b+g} D_s. \tag{2.2}$$

A direct description of the grain-face bubble development can define both fission gas swelling and thermal release for the grain-boundary gas behaviour analysis. The major assumptions [37] and features of the analysis are the following:

- An initial number density of grain-face bubbles is considered, and further nucleation during the irradiation is neglected (one-off nucleation, [48]);
- The absorption rate of gas at the grain-face bubbles is assumed to equal the arrival rate of gas at the grain boundaries [33, 48];
- Grain-face bubbles are considered to have, at any instant, equal size and equal lenticular shape of circular projection with semi-dihedral angle of 50° [49];
- Grain-face bubble growth (or shrinkage) is considered, taking into account the inflow of gas atoms from within the grains and concomitant absorption (or emission) of vacancies from the grain boundaries.

The bubble growth/shrinkage rate is calculated as:

$$\frac{dV_{\text{gf}}}{dt} = \omega \frac{dn}{dt} + \Omega \frac{dn_v}{dt} \tag{2.3}$$

where V_{gf} (m^3) is the bubble volume, ω (m^3) the Van der Waals covolume of a fission gas atom, n (atoms bubble^{-1}) the number of fission gas atoms per bubble, Ω (m^3) the atomic (vacancy) volume in the bubble, and n_v (vacancies bubble^{-1}) the number of vacancies per bubble. The model of Speight and Beere [43] is applied for the calculation of the vacancy absorption/emission rate at the lenticular bubble:

$$\frac{dn_v}{dt} = \frac{2\pi D_v \delta_g}{k_B S T} (p - p_{\text{eq}}) \tag{2.4}$$

where D_v (m^2 s^{-1}) is the vacancy diffusion coefficient in grain boundaries, δ_g (m) is the thickness of the diffusion layer in grain boundaries, k_B (J K^{-1}) the Boltzmann constant, T (K) the temperature, and S (-) is a dimensionless parameter that depends on the fraction of grain faces covered by bubbles, that is the fractional coverage [48].

The pressure of the gas in the bubble, p (Pa), is calculated based on the Van der Waals equation of state as:

$$p = \frac{k_B T}{\Omega} \frac{n}{n_v} \tag{2.5}$$

The mechanical equilibrium pressure, p_{eq} (Pa), is given by the sum of the bubble surface tension force and the hydrostatic stress in the surrounding medium. Grain-face bubble coalescence is described using the improved model of White, develped by Pastore et al. [36, 37]. The variation rate due to coalescence of the bubble number density, N (bubbles m^{-2}), is calculated as a function of the variation rate of the bubble projected area on the grain face, A_{gf} (m^2) (obtained from Eq. 2.3):

$$\frac{dN}{dt} = -2N^2 \left(\frac{dA_{\text{gf}}}{dt} \right). \tag{2.6}$$

Observations [48] of lightly irradiated fuel reveal large numbers of small, discrete, lenticular bubbles on the planar boundaries (faces), Fig. 2.1. With further irradiation, the size of the bubbles increase and their numbers decrease, Fig. 2.2. Considering these remarks, a lower bound for the bubble density N will be discuss in Section 3.1.

The swelling due to the grain-face gas bubbles is calculated [23, 4] as:

$$\frac{\Delta V}{V} = \frac{1}{2} \frac{3}{a} N V_{\text{gf}} \tag{2.7}$$

where V (m^3) is the fuel volume, a (m) the spherical grain radius, and $3/a$ represents the grain surface to volume ratio.
When the bubbles on the grain boundaries become enough large and numerous, the grain-face is considered as percolated and the fission gas will be released to the fuel rod free volume through free pathways made of interconnected bubbles. Only FGR following bubble interconnection pathways is considered by the model. This is underpinned by a principle of grain-face saturation: after the fractional coverage $F = NA_{\text{gf}}$ has reached the saturation value F_{sat} further bubble growth is compensated by gas release in order to maintain the constant coverage condition:

$$\begin{aligned} \frac{dn_{\text{fgr}}}{dt} &= 0 \quad \text{if} \quad F < F_{sat} \\ \frac{dn_{\text{fgr}}}{dt} &= n \frac{N}{A_{\text{gf}}} \frac{dA_{\text{gf}}}{dt} \quad \text{if} \quad F = F_{\text{sat}} \end{aligned} \tag{2.8}$$

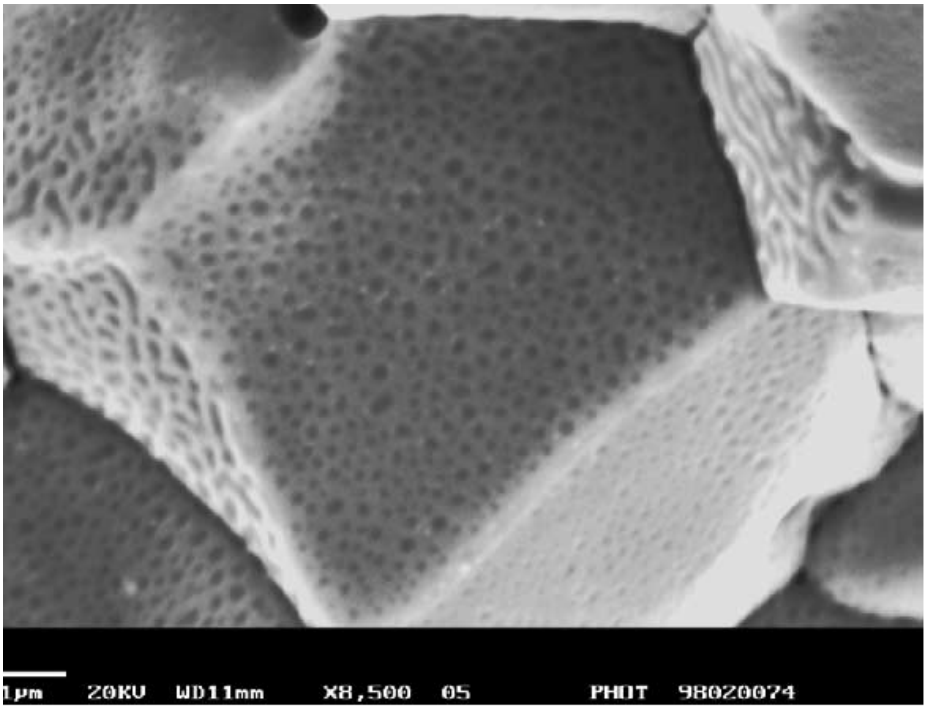

Figure 2.1: Early stage, lightly irradiated fuel (13 GWd t^{-1} U), of grain-face bubble development and the bubble density is high with little evidence of departures from circular bubbles [48].

where n_{fgr} (atoms m^{-2}) is the number of gas atoms released to the fuel rod free volume. Note that fission gas release and swelling are described as inherently coupled phenomena, as fission gas release from the grain faces counteracts bubble growth and thereby fission gas swelling. The saturation point is assumed as a constant with a value of $F_{\text{sat}} = 0.5$ [48, 36, 37].

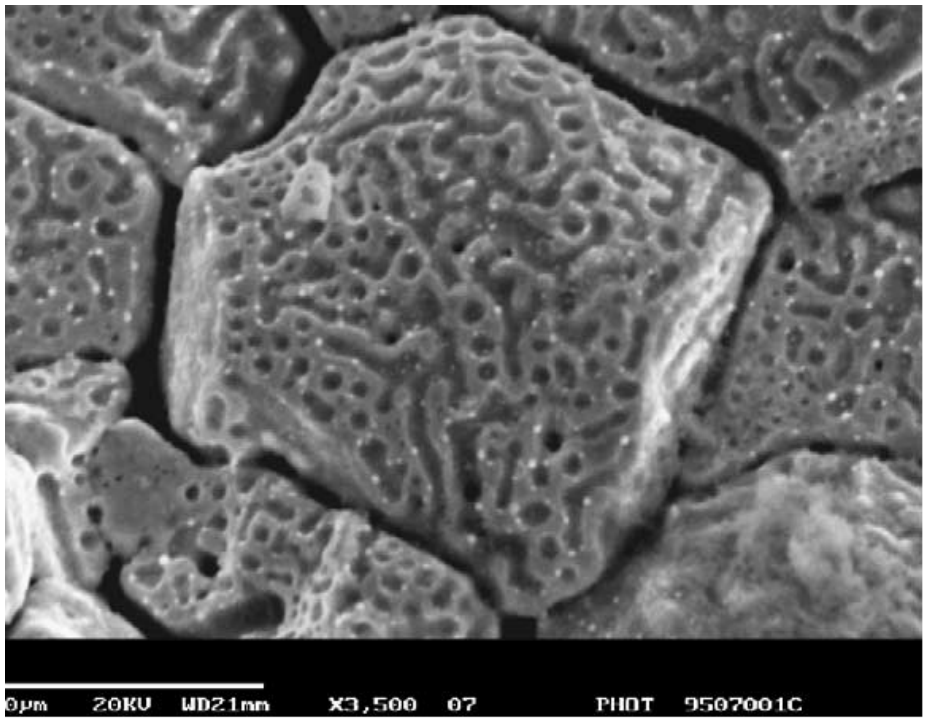

Figure 2.2: Advanced development of grain-face porosity under high level of irradiation:extensive bubble coalescence and lower bubble density [48].

2.2 Pore migration

Oxide nuclear fuels (UO_2 and MOX) [35, 33] have outstanding high temperature capabilities under irradiation. A temperature gradient is formed along the radius of the fuel pellet, with the hottest region at the center of the pellet and coolest near the cladding because of the inherent low thermal transport capabilities of the ceramic fuels. The fuel cannot quickly and efficiently manage heat, so this behaviour acts as an annealing process, and it leads to a grain growth and restructuring process.
After start-up and attainment of full-power and nominal operating fuel temperature, ceramic fuel (UO_2 and MOX) experiences meso-scale restructuring, which has a profound effect on the bulk properties of the fuel. Here, restructuring means that the fuel pellet develops distinct regions. Going from the center of the fuel outward in sequence, these regions are characterized by a central hole, a region of increased density, then a region with aligned grains and un-restructured grains, Figs 2.3 and 2.4. These regions form radial iso-surfaces due to restructuring of the fuel, which depends on temperature and its gradient [32].

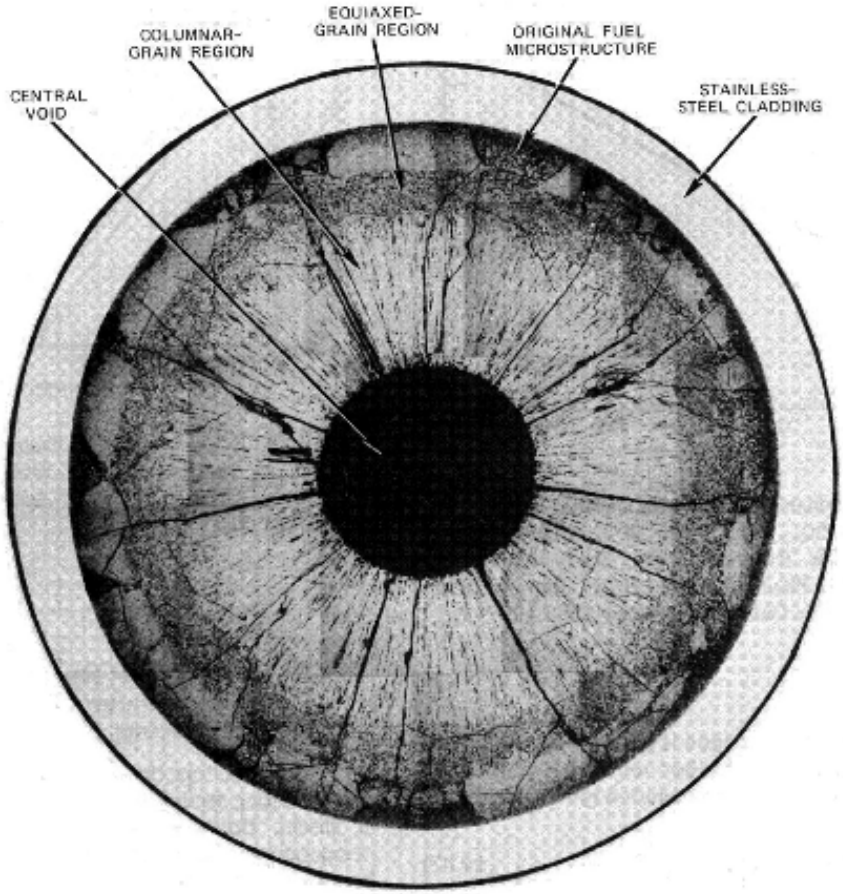

Figure 2.3: Micrograph from Olander [33] showing central void, restructured, and original fuel .

The central void [35] forms from the accumulation of voids and pores present in the fuel along a thermal gradient. Specifically within the columnar grain region of an irradiated fuel pellet, the pores migrate up the temperature gradient toward the center at varying rates depending on their starting size. The smallest spherical pores are highly mobile, being able to quickly and easily move through the restructured region. Intermediate sized pores become flat and elongated as they travel towards the fuel centers, leaving streaks at the tips of the voids as they travel. These "lenticular" voids are the most readily identifiable porosity feature in the irradiated MOX fuels due to their distinct shape. The largest voids, usually starting as fabricated porosity in the fresh fuel, are the least stable of the three regimes, creating the appearances of long streaks radially pointing toward the fuel center.

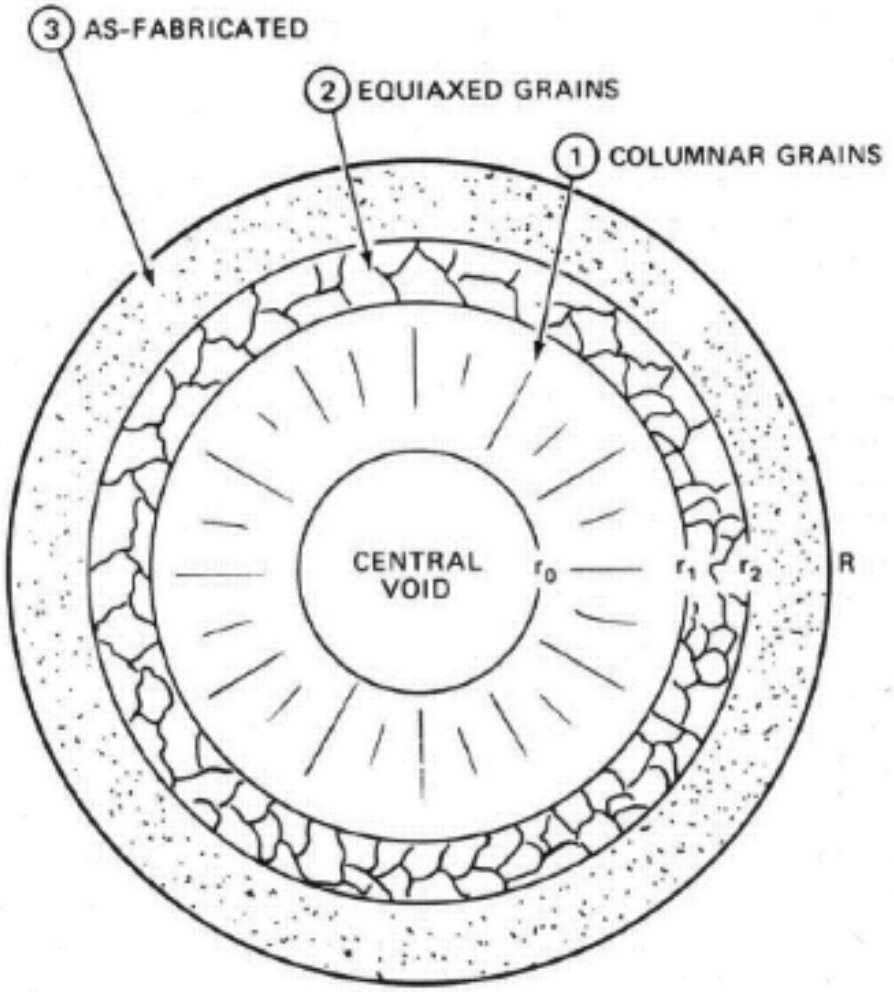

Figure 2.4: Diagram of microscale features where equiaxed and columnar grain regions are distinguished [33].

2.3 Oxygen redistribution

The fuel in a reactor [33] is subject to very steep temperature gradients, and it is also very likely that communication between regions of different temperature is made possible by cracks or interconnected porosity within the ceramic body. Introduction

of paths for transport via the gas phase means that the components of the fuel present in the vapor can readily move from one region to another. Oxygen tends to migrate radially through the fuel.
The oxygen transport is driven by a solid state thermal diffusion and it occurs via vacancies (hypo-stoichiometric fuel, usually fast MOX) and interstitials (hyper-stoichiometric fuel). Some results [38] show that the heat of oxygen transport depends on the plutonium and uranium valencies for hypo- and hyper-stoichiometric oxides respectively.

CHAPTER 3. MODEL DEVELOPMENT

In this Chapter, the development of the models for fission gas release, pore migration and oxygen redistribution is presented.

3.1 Fission gas release

It has been demonstrated by Colle et al. [8] and by Maeda et al. [28] that the fission gas release can reach high values at high temperatures and high burnup conditions. In particular Colle et al. [8] defines three stages for the release due to the temperature effect: i.) (near) surface release or venting from pre-existing open grain boundaries at usually T $<$ 1200 K (stage I); ii.) release due to the diffusion of gas after re-solution from bubbles and venting of intergranular pores in a temperature range from 1550 K to 1750 K (stage II); iii.) at very high temperatures the release comes from the surviving intragranular bubbles (stage III). These ranges of temperature and burnup are often achieved by fast MOX fuels irradiated in fast reactors and on the other side these values go far beyond the operational conditions for a LWR.

The model presented by Pastore et al. [36, 37] is currently the default option in BISON and it has been widely validated in LWR UO_2 cases so far. Since phenomena like grain-face bubble growth and the coalescence are emphasized at high temperatures it is expected that for MOX fuels irradiated in fast reactors this model needs an improvement and further validations. Nevertheless, these processes have a physical limit: the coalescence leads to fewer but bigger bubbles and their growth is strictly limited by the temperature (Eq. 2.4). As a consequence of bubble growth, the bubble number density progressively strongly decreases governed by Eq. 2.6. However, physically, there should be a limit to the coalescence process, i.e., the number density of grain-face bubbles cannot decrease below a lower bound when the extensive interlinkage of the grain boundaries is achieved. In a simplified approach, this limit can be interpreted as a lower bound to the number density of grain-face bubbles. In the original BISON model, such a lower bound was set to a constant value of 10^{10} bubbles m^{-2} [37]. However, this limit is of low importance for LWR fuel calculations, where it is normally not attained. On the contrary, for the analysis of higher temperature fuel such as fast reactor MOX, where bubble growth and coalescence proceed more rapidly, the limit becomes highly important in determining the calculated FGR and gaseous swelling. In this work, I propose a physically grounded approach to the determination of this lower bound for the number density of grain-face bubbles. Namely,

the limit number density of grain-face bubbles per unit surface, N_{lim} (bubbles m^{-2}) is:

$$N_{\text{lim}} = \frac{1}{2}\frac{N_{\text{eq}}N_{\text{face}}}{4\pi a^2} \tag{3.1}$$

where N_{face} (faces grain^{-1}) is the average number of faces in a grain (this value is assumed as 14 in this work), a (m) is the radius of a spherical grain and N_{eq} (bubbles face^{-1}), the bubble equivalent number, is the average number of bubbles on a grain face.

In order to determine a range of reasonable values for the bubble equivalent number, a numerical random experiment has been performed, generating:

- 1000 square images representative of the grain-faces.
- Each grain face is assumed of size 10x10 μm^2.
- On each grain face, single-sized circles of radius R, sampled from an uniform distribution $R(\mu\text{m}) \sim \mathcal{U}[0, 1]$, have been generated superposing.
- In each grain face, the number of effective bubbles, i.e., the number of not-connected clusters of circles, is counted.

In Fig. 3.1a, the number of effective bubbles is reported as a function of the fractional coverage F, with each point representing one of the 1000 images generated. The number of effective pores gradually decreases with the increase of the fractional coverage, because of the formation of clusters. For sake of example, Figure 3.1b reports one of the images generated, with fractional coverage $F = 0.43$ and a number of effective bubbles $N_{\text{eq}} = 29$.

From Fig. 3.1a, in conditions of saturation, i.e., when $F = F_{\text{sat}} = 0.5$, N_{eq} is in the range 0-20 bubbles face^{-1}. In this work, I assume $N_{\text{eq}} = 10$. The last remark is the factor 1/2 in Eq. 3.1, which accounts for the fact that a grain-face bubble is shared by two neighbouring grains.

Furthermore, it should be noted that N_{lim} proposed in this work is compatible with experimental observations of saturated grain boundaries, see Ref. [48].

The inclusion in the BISON fission gas behaviour model of a lower bound to the inter-granular bubble density bounds the coalescence process and by consequence the maximum size of grain-face bubbles. Consequently, once the lower limit for the number density of bubbles is achieved, any further bubble growth is compensated by FGR by virtue of Eq. 2.8. Consequently, both bubble number density and size remain constant at this point. Note that in the current model, given the same fractional

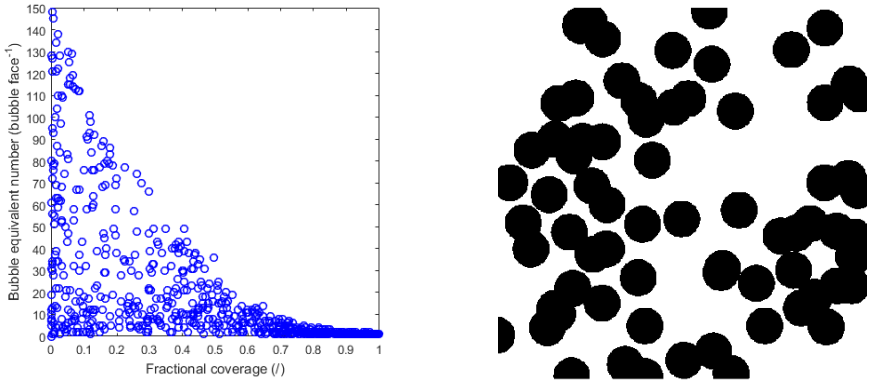

(a) **(b)**

Figure 3.1: Results of the random numerical experiment used to derive the number of equivalent bubbles per grain face. On the left (a) I report the bubble equivalent number obtained as a function of the fractional coverage, while on the right (b) I report a sample image of a pattern of bubbles covering a grain face as obtained by the random process.

coverage, the fewer the bubbles the larger the volume they occupy and the higher the total gas atoms they retain [36, 37]. Hence, FGR after the attainment of the limit is expected to be higher compared to the situation where coalescence continues.

It should be noted that, after the attainment of the lower limit in the number density of grain-face bubbles, the model representation becomes a stronger simplification of the actual behavior. Essentially, at this point the grain-face bubble population is assumed to reach a stationary situation where further evolution is prevented. Also, after extensive interlinkage, bubbles form elongated or vermicular structures [48], so that the basic model assumption of circular bubbles becomes stronger in itself. However, the concept of a stationary situation is considered reasonable as an attempt to consider behavior after extensive bubble interlinkage within the current model framework and in a physically meaningful way. As a final physical justification for the introduction in the model of such a lower bound, it should be observed that without any limitation[2] the evolution of grain-face bubbles ignores the fact that bubbles are constrained on a single grain face, and can in principle allow for interconnection between bubbles belonging to different grain faces.

[2]For the sake of simplicity, in this work, I refered to the standard version of BISON that considers the limit of 10^{10} bubbles m^{-2}, using the terms 'BISON without any limitations'. I took this simplification because in the conditions of all the cases analyzed in this work, the number density of grain-face bubbles never reaches the limit proposed by Pastore et al. [37].

Moreover, since in fast reactors the fission rate is higher, the diffusion coefficient for fission gas atoms proposed by Turnbull et al. [15] is taken into account. The default intra-granular diffusion coefficient for fission gasses used in BISON was provided by Turnbull et al. [46] negletting the contribution of the athermal term (D_3):

$$D_s = D_1 + D_2 + D_3 \tag{3.2}$$

where D_1 ($m^2\ s^{-1}$) is the thermal component that depends just on temperature, D_2 ($m^2\ s^{-1}$) the enhanced term that is a function of both temperature and the fission rate and D_3 ($m^2\ s^{-1}$) is the athermal component that has a dependence only on the fission rate. It has been decided to use the coefficient proposed by Turnbull et al. [15] because this diffusion coefficient emphasizes the enhanced and the athermal components dependent on the fission rate.

Another problem found with fast reactor MOX cases pertains to the grain growth model by Ainscough et al. [2] implemented in BISON. When a polycrystalline material is subject to high temperatures, larger grains tend to grow at the expense of the smaller ones. As a consequence, the latter gradually disappear, thus reducing the total number of grains per unit volume and increasing the average grain size. This phenomenon is known as grain growth. The granular structure of the fuel affects physical processes such as fission gas behavior.
Hence, this empirical model [2] is implemented in BISON for computing the grain growth in UO_2 fuel. According to this model, the kinetics of grain growth is described by the equation:

$$\frac{dD}{dt} = k\left(\frac{1}{D} - \frac{1}{D_m}\right) \tag{3.3}$$

where D (μm) is the 2-dimensional (linear intercept) average grain diameter, t (h) the time, k ($\mu m^2\ h^{-1}$) the rate constant, and D_m (μm) is the limiting grain size. The rate constant is given as

$$k = 5.24 \cdot 10^7\ exp(\frac{-2.67 \cdot 10^5}{RT}) \tag{3.4}$$

where R (J mol^{-1} K^{-1}) is the universal constant of the gas. The limiting grain size is a function of the temperature such that:

$$D_m = 2.23 \cdot 10^3\ exp(-7620/T) \tag{3.5}$$

Due to the high temperatures reached in fast reactor MOX cases, the model predicts un-physical values for the grain radius, i.e., about 100 μm. Hence, because of the lack

of a model able to describe the grain growth for these conditions, for this work it has been decided to use constant values for the grain radius. An investigation about the effects of the grain radius on the limit described in Eq. 3.1 is performed in Section 6.1.

3.2 Pore migration

As described by Novascone et al. [32], the temperature gradient triggers the motion of the pores. The model takes into account a partial differential equation that characterizes the advection-diffusion of pores (conservation of pores):

$$\frac{\partial P}{\partial t} + \nabla \cdot (P v_P \nabla T - \nu \nabla P) = 0 \tag{3.6}$$

where T (K) is the temperature, P (/) is the fraction of porosity, v_P (m^2 s^{-1} K^{-1}) is the pore velocity, ν (m^2 s^{-1}) is the effective porosity diffusion coefficient to represent pore migration via surface and bulk diffusion. The pore velocity v_P in Eq. 3.6 is a highly uncertain quantity, and it has been subjected to a considerable amount of prior studies [33, 30, 40, 16, 34, 9, 25, 47]. In this work, with reference to Novascone et al [32], I used the expression provided by Sens [40]:

$$v_P = c_0(c_1 + c_2 T + c_3 T^2 + c_4 T^3) T^{-5/2} \times \Delta H p_0 \exp\left(-\frac{\Delta H}{RT}\right) \tag{3.7}$$

where T (K) is temperature and R (J mol^{-1} K^{-1}) is the universal gas constant. This model is based on vapor pressure driving pore migration. The exponential Arrhenius term depends on the UO_2 vapor pressure and it is multiplied by a factor p_0 (Pa) and by the heat of vaporization ΔH (J mol^{-1}). The factors c_1, c_2, c_3 and c_4 are constant coefficients coming from experimental measurements. All these parameters are summarized in Table 3.1. In Novascone et al. [32], the temperature gradient is included in the pore velocity term, but here, the temperature gradient is written separately to emphasize the dependence of pore migration on temperature gradient (Eq. 3.6).

Table 3.1: List of the model parameters.

Symbol	Definition	Value	u.o.m.	Reference
c_0	Model parameter	5×10^{-16}		[40]
c_1	Model parameter	0.988		[40]
c_2	Model parameter	6.395×10^{-6}		[40]
c_3	Model parameter	3.543×10^{-9}		[40]
c_4	Model parameter	3×10^{-12}		[40]
p_0	UO_2 vapor pressure	33708.5	Pa	[40]
ΔH	Heat of vaporization	5.98×10^{5}	J mol^{-1}	[40]
ν	Effective porosity diffusion coefficient	1×10^{-12}	m^2 s^{-1}	[32]

3.3 Oxygen redistribution

For uranium oxide fuels the initial oxygen-to-metal ratio is very close to 2.00. For fast MOX reactors, the fabrication value is slightly lower – hypo-stoichiometric – because, with very high burnup levels targeted in fast reactors, the content of oxygen in the fuel increases, since the fission can be considered as an oxidative process [44]. In these conditions, when the O/M ratio increases beyond 2.00, the overabundance of oxygen can lead to a diffusion of this element from the fuel to cladding when the contact is established, causing a corrosion of the cladding from the inside [20, 21, 22]. Nevertheless, in the model used for this work the effect of oxidation production due to the fission is not considered.

In this Section, the model for the oxygen redistribution proposed by Lassmann [26] has been implemented in the BISON code. Oxygen redistribution is modeled by applying the concept of Fick and Soret diffusion:

$$\frac{\partial c}{\partial t} + \nabla \cdot N_{\text{ox}} D_{\text{ox}} \left(\nabla c + c \frac{Q}{RT^2} \nabla T \right) = 0 \tag{3.8}$$

where c (/) is the atomic fraction of interstitial atoms or oxygen vacancies, T (K) is the temperature, R (J mol^{-1} K^{-1}) is the gas constant, N_{ox} (atoms m^{-3}) is the total number of oxygen atoms per unit volume, D_{ox} (m^2 s^{-1}) is the diffusion coefficient of interstitial atoms or oxygen vacancies and Q (J mol^{-1}) is the molar effective heat of transport. The diffusion coefficient, taken according to Lassmann [26], is:

$$D_{\text{ox}} = 1.39 \times 10^{-6} \exp \frac{-75900}{RT} \tag{3.9}$$

Since c and Q have different expressions depending on the stoichiometry of the fuel (hypo- or hyper-stoichiometric), both the cases were described and implemented in BISON. Being x the deviation of from the stoichiometry:

$$x = \frac{O}{U + Pu} - 2 \tag{3.10}$$

$$x = -2c_v \quad \text{(hypo-stoichiometric case)} \tag{3.11}$$

$$x = c_i \qquad \text{(hyper-stoichiometric case)} \tag{3.12}$$

c_v and c_i are the atomic fraction of oxygen vacancies and interstitial atoms, respectively. For the hypo-stoichiometric case the heat of oxygen transport from Eq. 3.8 depends on the valence of plutonium V_{Pu}:

$$Q_v = -8.12 \times 10^{-4} exp(4.85 V_{\mathrm{Pu}}) \quad \text{for} \quad V_{\mathrm{Pu}} < 3.3 \tag{3.13}$$

$$Q_v = -3.96 \times 10^6 + 2.37 \times 10^6 V_{\mathrm{Pu}} - 3.6 \times 10^5 V_{\mathrm{Pu}}^2 \quad \text{for} \quad 3.3 \leq V_{\mathrm{Pu}} < 4.0 \tag{3.14}$$

V_{Pu} is the average valence of plutonium ions and it can be described as:

$$V_{\mathrm{Pu}} = 4 + 2 \cdot \frac{x}{q} = 4 - 4 \cdot \frac{c}{q} \tag{3.15}$$

where q (/) is the plutonium to heavy metal atoms ratio. It is defined by Karahan [16] as:

$$q = \frac{q_0}{1 - Bu} \tag{3.16}$$

where q_0 (/) is the initial plutonium to heavy metal atoms ratio and Bu (FIMA) the burnup.
In the hyper-stoichiometric case the heat of oxygen transport is a function of the valence of uranium V_U:

$$Q_i = -3.5 \times 10^{34} exp(-17 V_U) \quad \text{for} \quad V_U \geq 4.0 \tag{3.17}$$

V_U is the average valence of uranium ions and it can be described as:

$$V_U = 4 + 2 \cdot \frac{x}{1 - q} = 4 + 2 \cdot \frac{c}{1 - q}. \tag{3.18}$$

CHAPTER 4. MODEL TEST AS STAND-ALONE WITH BISON

In this Chapter, the extension for the fission gas release model (Section 3.1) is tested against the experimental database provided by Baker [5, 6].

In this Chapter, I present the introdution of Eq. 3.1 in BISON simulating the experiments performed by Baker [5, 6]. In this experiment the fuel pins, have been irradiated in the UKAEA's Winfrith SGHWR up to a burnup of ∼1% and the samples examined by Baker [5, 6] lay in the temperature range from 1273 K up to 2073 K. Therefore these values represent both operational conditions for UO_2-LWR (up to about 1600 K) and more critical ones (beyond 1700 K), where this last range, instead, is closer to operational circumstances for fast MOX reactors.

The experimental data from [5, 6] correspond to local information, i.e., small fuel samples. In order to simulate it with BISON, a single-cube mesh has been used. Every simulation has been performed at a different temperature (starting from 1273 K up to 2073 K) and assuming a constant grain radius of 5 μm, corresponding to a N_{lim} of 2×10^{11} bubbles m^{-2}.

Figs. 4.1 and 4.2 report all the results at each of the considered temperatures for the variables of most interest, namely: the fission gas release FGR (%), the number density of grain boundary bubbles per unit surface N (bubbles m^{-2}) and the volumetric swelling at the grain boundary (%).

At lower temperatures Fig. 4.1), since N does not reach the proposed limit, the resulting FGR and volumetric swelling at the grain boundary are the same for both the cases (Fig. 4.1a-Fig. 4.1o). In Fig. 4.2, as temperature raises (from 1773 K and so on), the lower bound for the bubble number density at the grain boundary proposed in this work is reached (Fig. 4.2b, Fig. 4.2e, Fig. 4.2h and Fig. 4.2k) and this implies a higher FGR and a lower volumetric swelling at the grain boundary compared to the case without the limit (Fig. 4.2a, Fig. 4.2c, Fig. 4.2d, Fig. 4.2f, Fig. 4.2g, Fig. 4.2i, Fig. 4.2j, Fig. 4.2l). In fact, due to the higher temperatures (comparable to ranges for fast MOX), the associated pronounced bubble growth and coalescence can lead to the attainment of the lower bound for the number density of grain boundary bubbles systematically. These results highlight the importance of the proposed model modification at temperatures comparable to fast reactor fuel conditions.

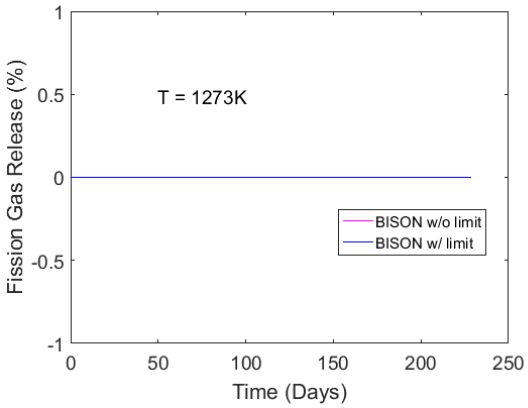
Fission Gas Release (%)
T = 1273K
BISON w/o limit
BISON w/ limit
Time (Days)

(a)

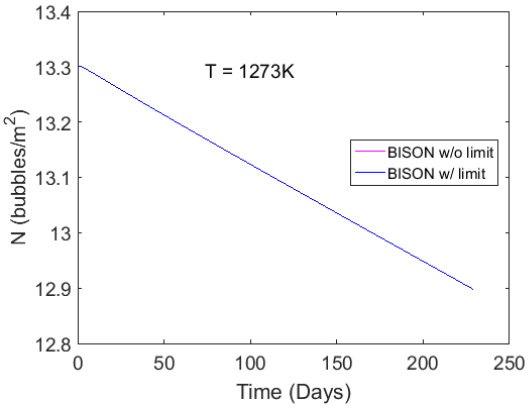
N (bubbles/m^2)
T = 1273K
BISON w/o limit
BISON w/ limit
Time (Days)

(b)

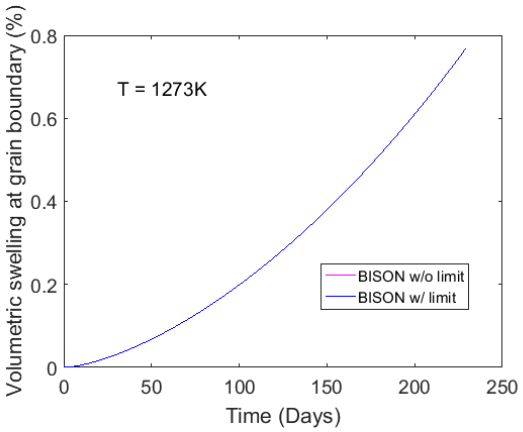
Volumetric swelling at grain boundary (%)
T = 1273K
BISON w/o limit
BISON w/ limit
Time (Days)

(c)

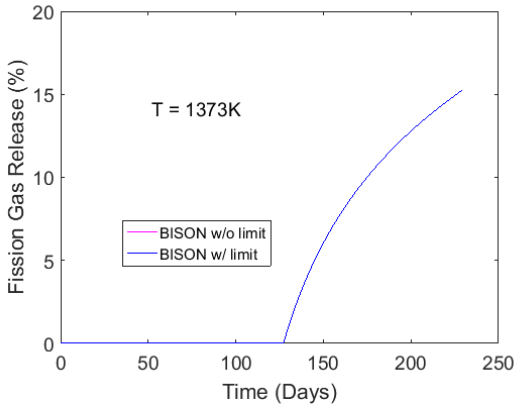
Fission Gas Release (%)
T = 1373K
BISON w/o limit
BISON w/ limit
Time (Days)

(d)

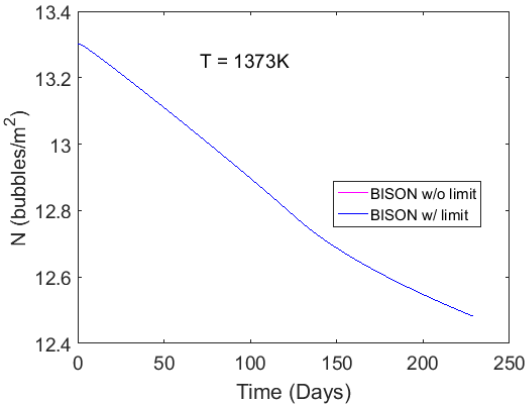
N (bubbles/m^2)
T = 1373K
BISON w/o limit
BISON w/ limit
Time (Days)

(e)

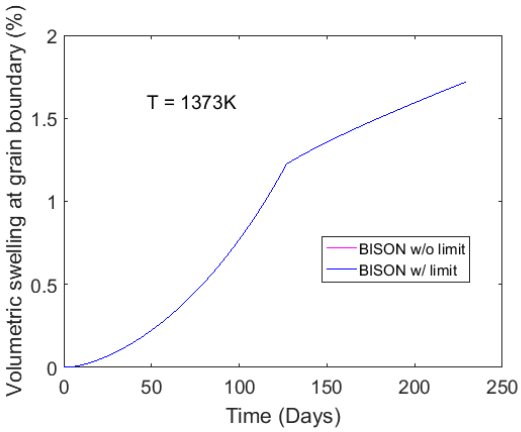
Volumetric swelling at grain boundary (%)
T = 1373K
BISON w/o limit
BISON w/ limit
Time (Days)

(f)

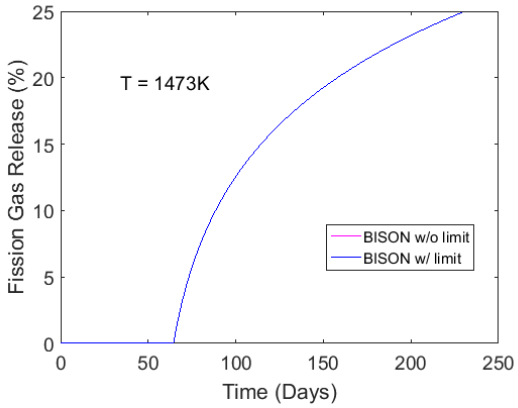
T = 1473K
Fission Gas Release (%)
Time (Days)
BISON w/o limit
BISON w/ limit
0
5
10
15
20
25
0
50
100
150
200
250

(g)

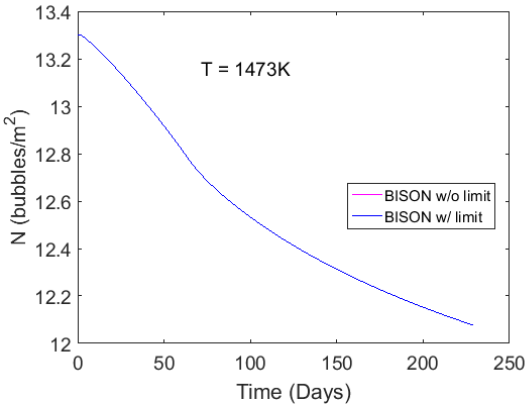
T = 1473K
N (bubbles/m^2)
Time (Days)
BISON w/o limit
BISON w/ limit
12
12.2
12.4
12.6
12.8
13
13.2
13.4
0
50
100
150
200
250

(h)

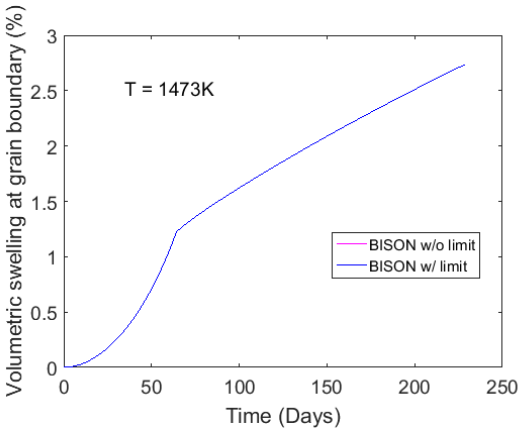
T = 1473K
Volumetric swelling at grain boundary (%)
Time (Days)
BISON w/o limit
BISON w/ limit
0
0.5
1
1.5
2
2.5
3
0
50
100
150
200
250

(i)

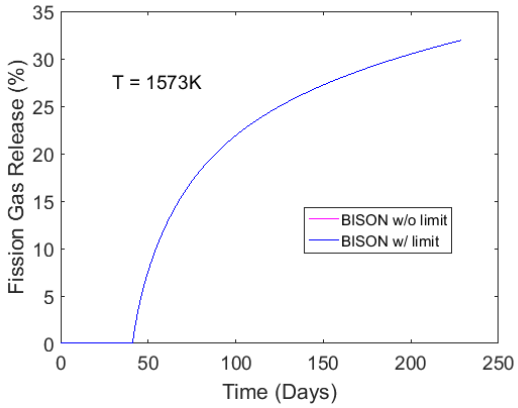
T = 1573K
Fission Gas Release (%)
Time (Days)
BISON w/o limit
BISON w/ limit
0
5
10
15
20
25
30
35
0
50
100
150
200
250

(j)

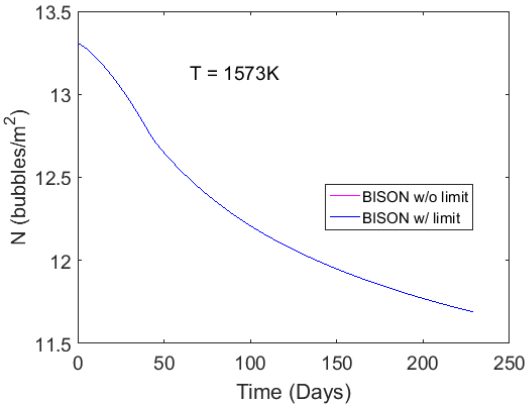
T = 1573K
N (bubbles/m^2)
Time (Days)
BISON w/o limit
BISON w/ limit
11.5
12
12.5
13
13.5
0
50
100
150
200
250

(k)

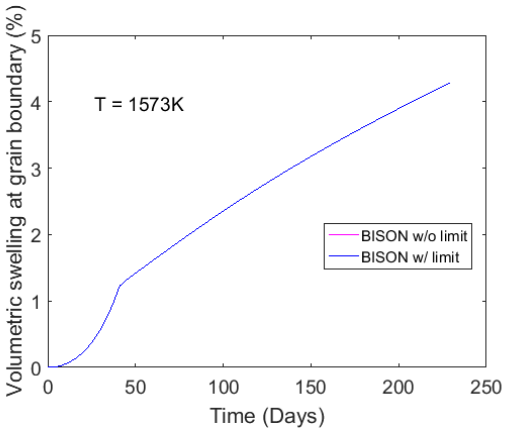
T = 1573K
Volumetric swelling at grain boundary (%)
Time (Days)
BISON w/o limit
BISON w/ limit
0
1
2
3
4
5
0
50
100
150
200
250

(l)

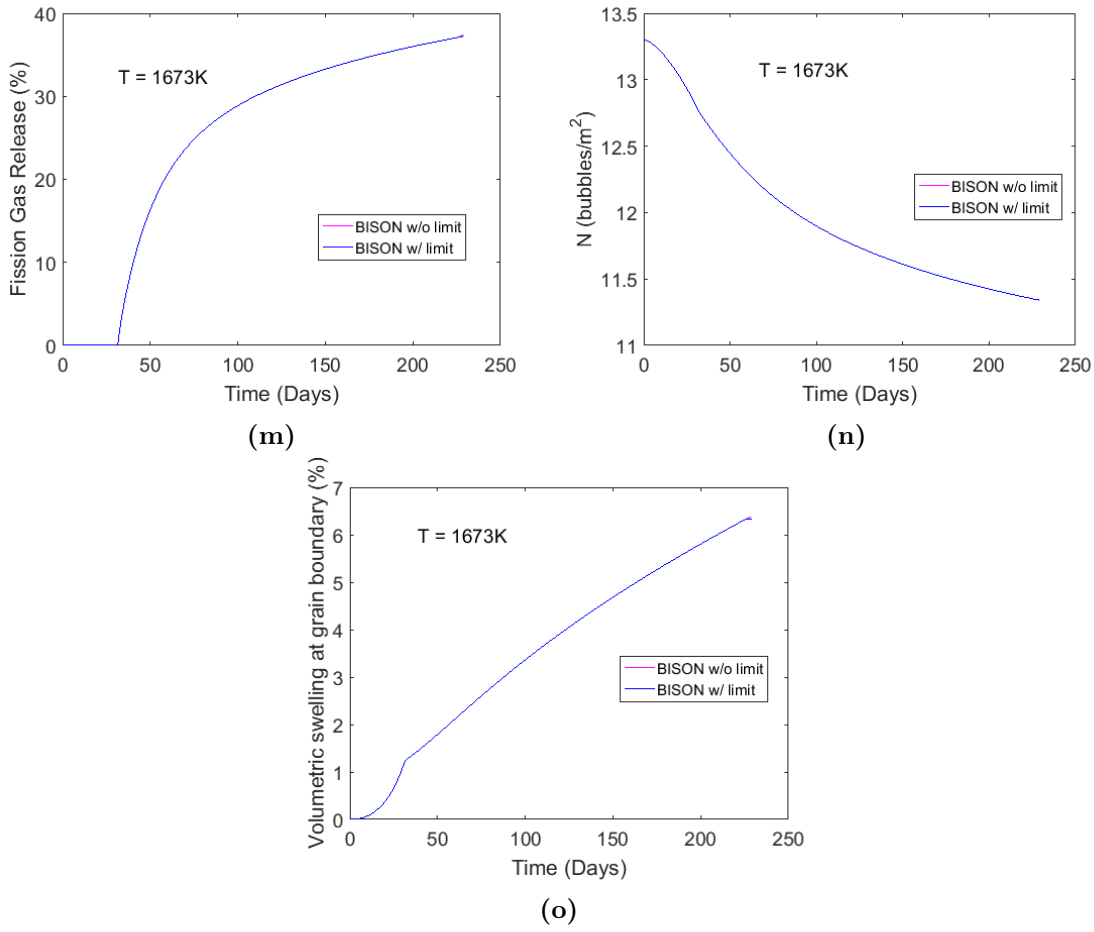

Figure 4.1: Stand-alone simulations on UO_2 from the Baker database ([5] and [6]) performed with BISON in a range of temperatures from 1273 K up to 1673 K. For every temperature the fission gas release FGR (%), the number density of bubbles at the grain boundary per unit surface N (bubbles m^{-2}) and the volumetric swelling at the grain boundary (%) evolution as function of the time are reported. The plots related to N are expressed with a semilogarithmic scale. In every figure the purple lines, corresponding to the standard BISON version, cannot be distinguished from the blue ones (with a N_{lim} of $2{\times}10^{11}$ bubbles m^{-2}, coming from Eq. 3.1), because they are overlapped.

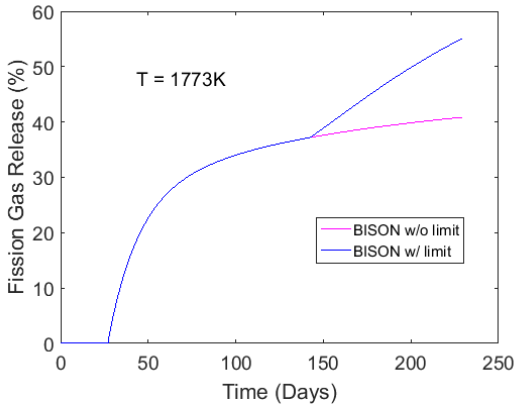
T = 1773K
Fission Gas Release (%)
Time (Days)
BISON w/o limit
BISON w/ limit
0
10
20
30
40
50
60
0
50
100
150
200
250

(a)

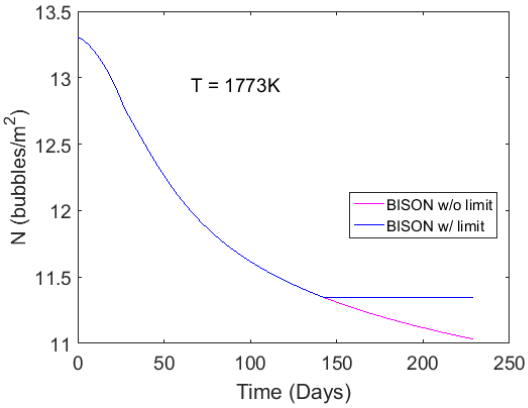
T = 1773K
N (bubbles/m^2)
Time (Days)
BISON w/o limit
BISON w/ limit
11
11.5
12
12.5
13
13.5
0
50
100
150
200
250

(b)

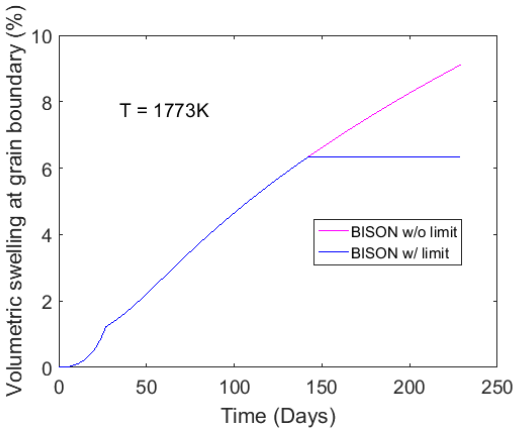
T = 1773K
Volumetric swelling at grain boundary (%)
Time (Days)
BISON w/o limit
BISON w/ limit
0
2
4
6
8
10
0
50
100
150
200
250

(c)

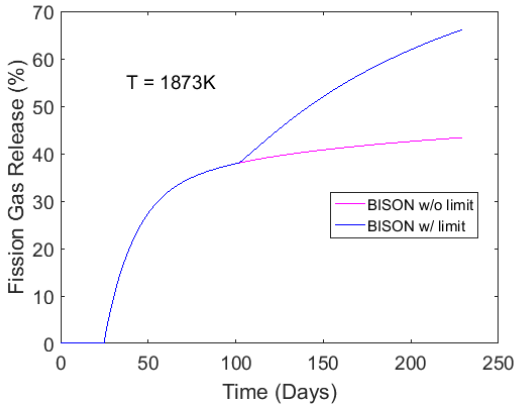
T = 1873K
Fission Gas Release (%)
Time (Days)
BISON w/o limit
BISON w/ limit
0
10
20
30
40
50
60
70
0
50
100
150
200
250

(d)

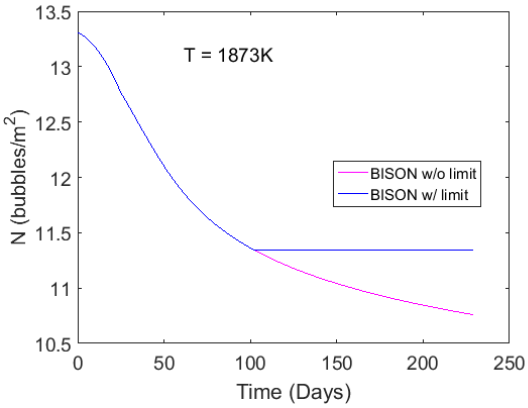
T = 1873K
N (bubbles/m^2)
Time (Days)
BISON w/o limit
BISON w/ limit
10.5
11
11.5
12
12.5
13
13.5
0
50
100
150
200
250

(e)

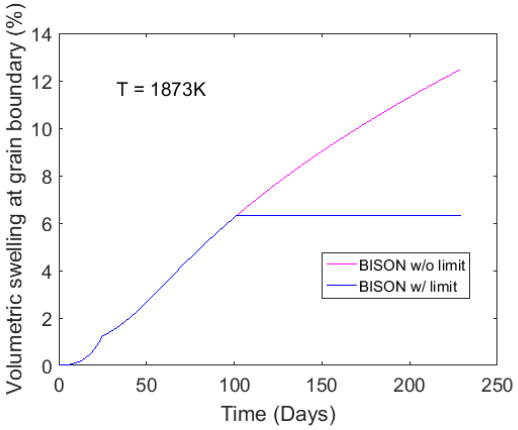
T = 1873K
Volumetric swelling at grain boundary (%)
Time (Days)
BISON w/o limit
BISON w/ limit
0
2
4
6
8
10
12
14
0
50
100
150
200
250

(f)

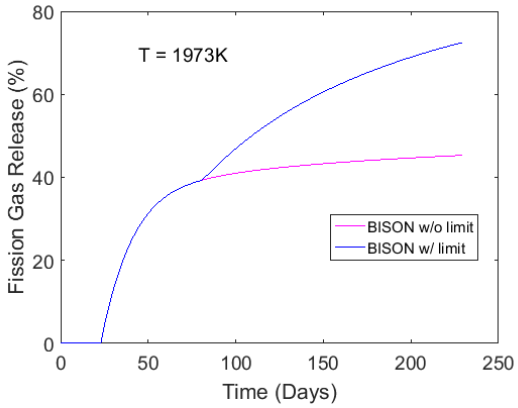
T = 1973K
Fission Gas Release (%)
Time (Days)
BISON w/o limit
BISON w/ limit
0
20
40
60
80
0
50
100
150
200
250

(g)

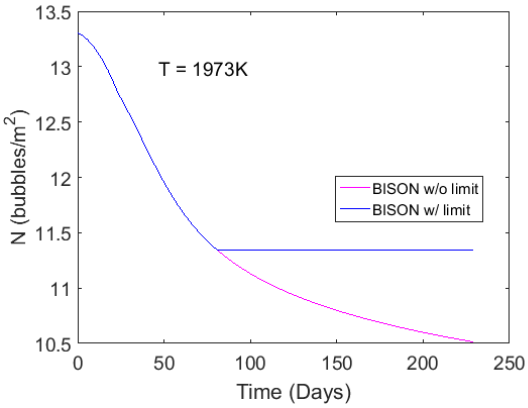
T = 1973K
N (bubbles/m^2)
Time (Days)
BISON w/o limit
BISON w/ limit
10.5
11
11.5
12
12.5
13
13.5
0
50
100
150
200
250

(h)

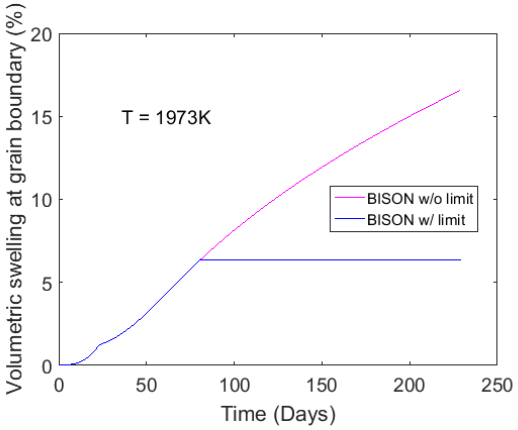
T = 1973K
Volumetric swelling at grain boundary (%)
Time (Days)
BISON w/o limit
BISON w/ limit
0
5
10
15
20
0
50
100
150
200
250

(i)

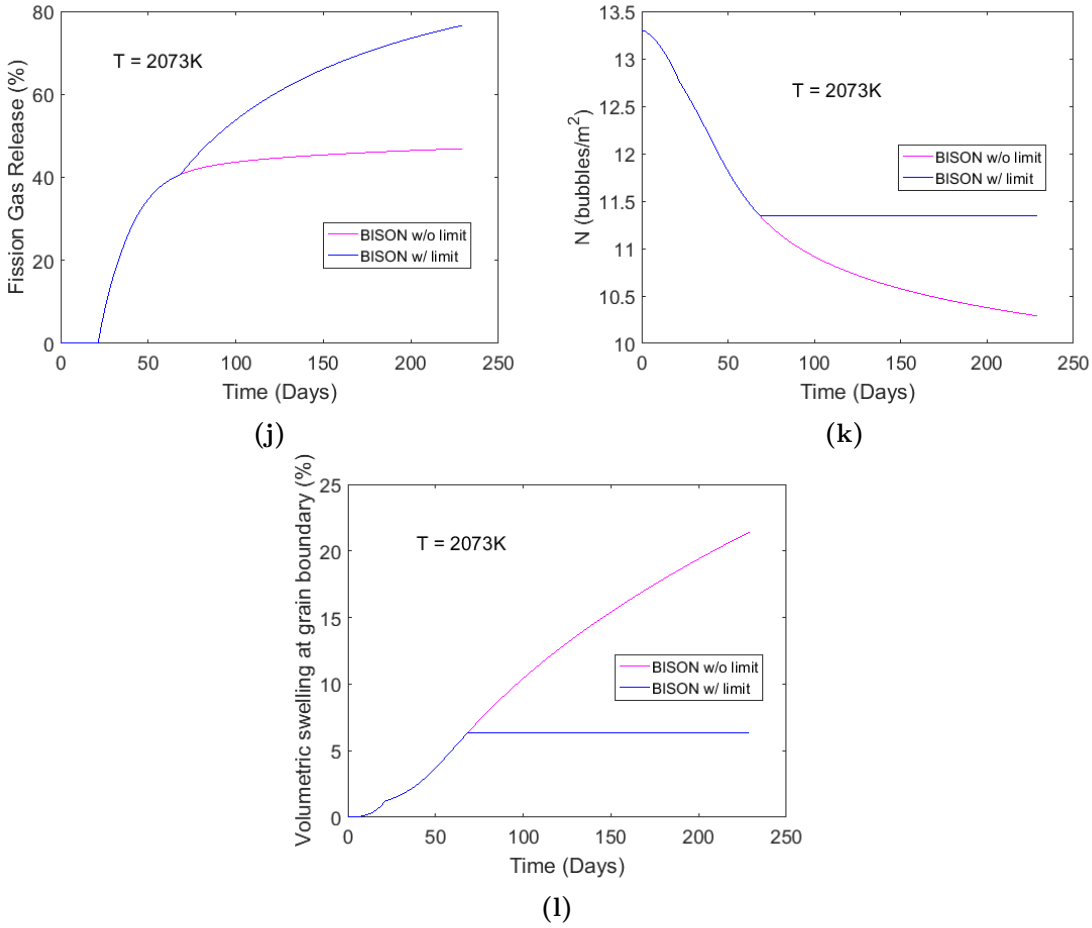

Figure 4.2: Stand-alone simulations on UO_2 from the database [5] and [6] performed with BISON in a range of temperatures from 1773 K up to 2073 K. For every temperature the fission gas release FGR (%), the number density of bubbles at the grain boundary per unit surface N (bubbles m^{-2}) and the volumetric swelling at the grain boundary (%) evolution as function of the time are reported. The plots related to N are expressed with a semilogarithmic scale in order to highlight the differences between the two cases analyzed. The purple line refers to the standard BISON version without any limitation on bubble growth and coalescence processes; the blue line corresponds to the case that uses the lower bound for the bubble number density at the grain boundary N_{lim} (Eq. 3.1), corresponding to a value of $2{\times}10^{11}$ bubbles m^{-2}.

CHAPTER 5. INTEGRAL FUEL ROD ANALYSES WITH BISON

In this Chapter, I briefly summarize the main features of the irradiation experiments FO-2, B14, MK-I and MK-II simulated with BISON.

The FO-2 assembly has been irradiated in the Fast Flux Test Facility (FFTF), a sodium fast reactor, for 312 Equivalent Full Power Days (EFPD) [12] between December 22, 1984 and April 25, 1986 to a peak burn-up of $\sim 6\%$ FIMA and a peak fast fluence of 9.9×10^{22} n cm^{-2} (E $>$ 0.1 MeV) [45]. The considered power history is a simplified history at a linear heat rate of 38.8 kW m^{-1} based on the data from Teague et al. [45]. This test uses the alloy HT-9 as cladding material. The FO-2 assembly is composed by 169 fuel pins of twelve different types. The fuel was manufactured with co-precipitated (U,Pu)O_2 powder, ensuring a uniform plutonium distribution throughout the pellets [45]. The annular fuel pin L09 was destructively examined. This pin was punctured and it was cut at three different elevations (sample H, sample J and sample L), Fig. 5.1.

The B14 experiment has been performed in the Japanese experimental sodium fast reactor JOYO for just 68 hours of irradiation time, from May 8 to 11 2007 [27]. As shown in Fig. 5.2, the irradiation has been performed in three steps: a first preconditioning up to 92 MW_{th}, held for 24 hours, a second preconditioning at 102 MW_{th} for 24 hours and final transient of 10 minutes where the power has been increased up to 125 MW_{th}, followed by a quick shut down performed by manual SCRAM [27]. The B14 assembly is composed by 4 solid fuel pins: PTM001, PTM002, PTM003 and PTM010. These pins were non-destructively examined by X-ray computer tomography (CT). They have been also destructively examined, Fig. 5.3. Ceramography specimens were taken from two axial positions: the former at a medium level (about +30 mm from the core mid plane), and the latter at the upper axial level of the fuel column (about +100 mm from the core mid plane).
MK-I core has been irradiated in the Japanese experimental fast reactor JOYO at 50 MW_{th} and at 75 MW_{th} from 1977 to 1981 [41], up to a burnup of $\sim 2.5\%$ FIMA and $\sim 5\%$ FIMA, respectively.
MK-II core was irradiated in the JOYO reactor from 1983 to 1986, up to a burnup of $\sim 5\%$ FIMA.
JOYO was the first sodium cooled reactor leading the FBR development program in Japan. The MK-I and MK-II cores are composed by a maximum of 80 and 67 driver assemblies, respectively, surrounded by stainless steel reflectors.
More details about the power histories and other information for the experiments

FO-2 and MK can be obtained consulting Teague et al. [45] and Shimada et al. [41], respectively. The specifications for these experiments are summarized in Table 5.1.

Table 5.1: Fuel pin specifications and irradiation data.

Rod	FO-2 L09	PTM001	PTM002	PTM003	PTM010	MK-I at 50MW	MK-I at 75MW	MK-II
Fuel Data								
Fuel	MOX	MAMOX[1]				MOX		
Pu content (wt%)	26.0	32	32	32	32	18	18	30
Am content (wt%)	-	2.4	2.4	2.4	2.4	-	-	-
Oxygen-to-metal ratio	1.96	1.98	1.98	1.96	2.00	1.98	1.98	1.98
Pellet outer diameter (mm)	5.59	5.56	5.56	5.56	5.56	5.4	5.4	4.63
Pellet inner diameter (mm)	1.397	-	-	-	-	-	-	-
Fuel stack height (mm)	914	400	400	400	400	600	600	550
Pellet density (%TD)	91.7	85	85	85	85	93.5	93.5	93
Fuel Rod								
Cladding material	HT-9	PNC316				316SS		
Cladding outer diameter (mm)	6.858	6.5	6.5	6.5	6.5	6.3	6.3	5.5
Cladding thickness (mm)	0.533	0.47	0.47	0.47	0.47	0.35	0.35	0.35
Gap width (μm)	101.6	160	210	160	210	100	100	100
Nominal plenum height (mm)	1057	685	685	685	685	600	600	550
Fill gas composition	He	He (91%) and Kr (9%)				He	He	He
Fill gas pressure (MPa)	0.1	0.1	0.1	0.1	0.1	0.3	0.3	0.3
Linear heat rate (kW m^{-1})	38.8[2]	[3]	[3]	[3]	[3]	21	32	40
Max. Burnup (% FIMA)	~ 6	~ 0.05	~ 0.05	~ 0.05	~ 0.05	~ 2.5	~ 5	~ 5

[1] Minor Actinide MOX: Am-bearing MOX
[2] Simplified power history from Teague et al.[45]
[3] See Fig. 5.2

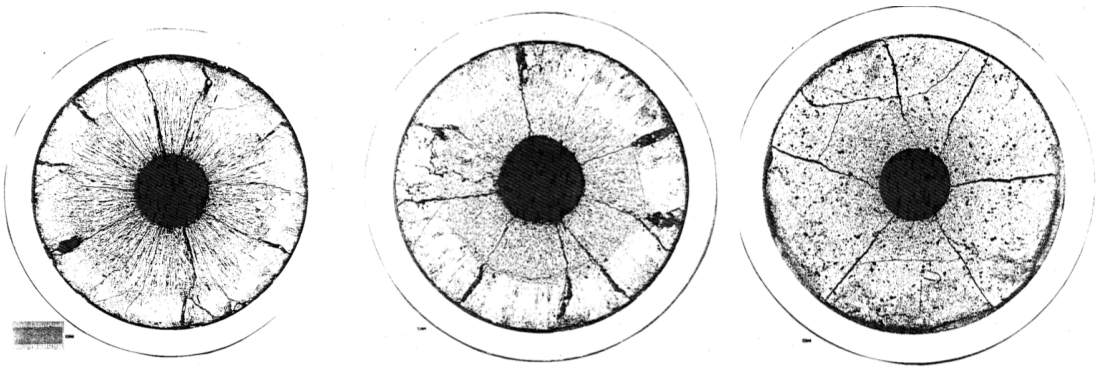

(a) **(b)** **(c)**

Figure 5.1: Ceramograhy specimens for L09: (a) Sample H located at 43.2 cm from the bottom of the fuel, (b) sample J located at 68.6 cm from the bottom of the fuel and (c) sample L located at 91.3 cm from the bottom of the fuel. Provided by Gilpin et al. [12].

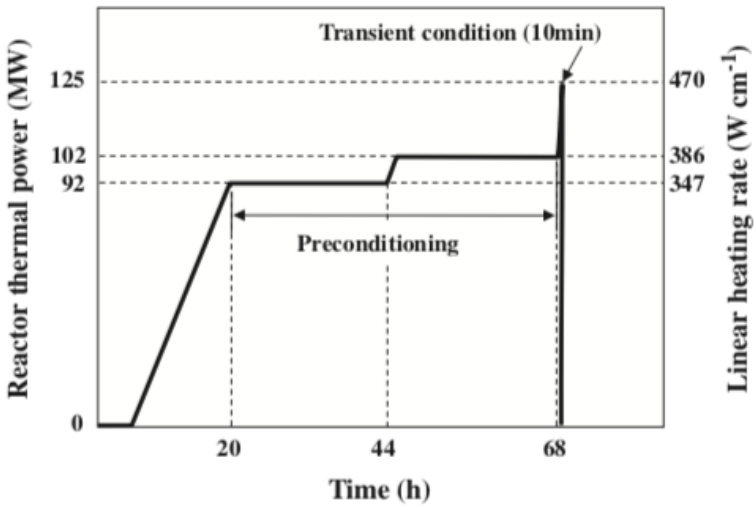

Figure 5.2: B14 schematic diagram of irradiation history of reactor thermal power and linear heating rate for fuel pins provided by Maeda et al. [27]. The experiment consists in 24 hours of a first preconditioning at 92 MW_{th}, followed by other 24 hours of preconditioning at 102 MW_{th} and with a final transient of 10 minutes at 125 MW_{th}.

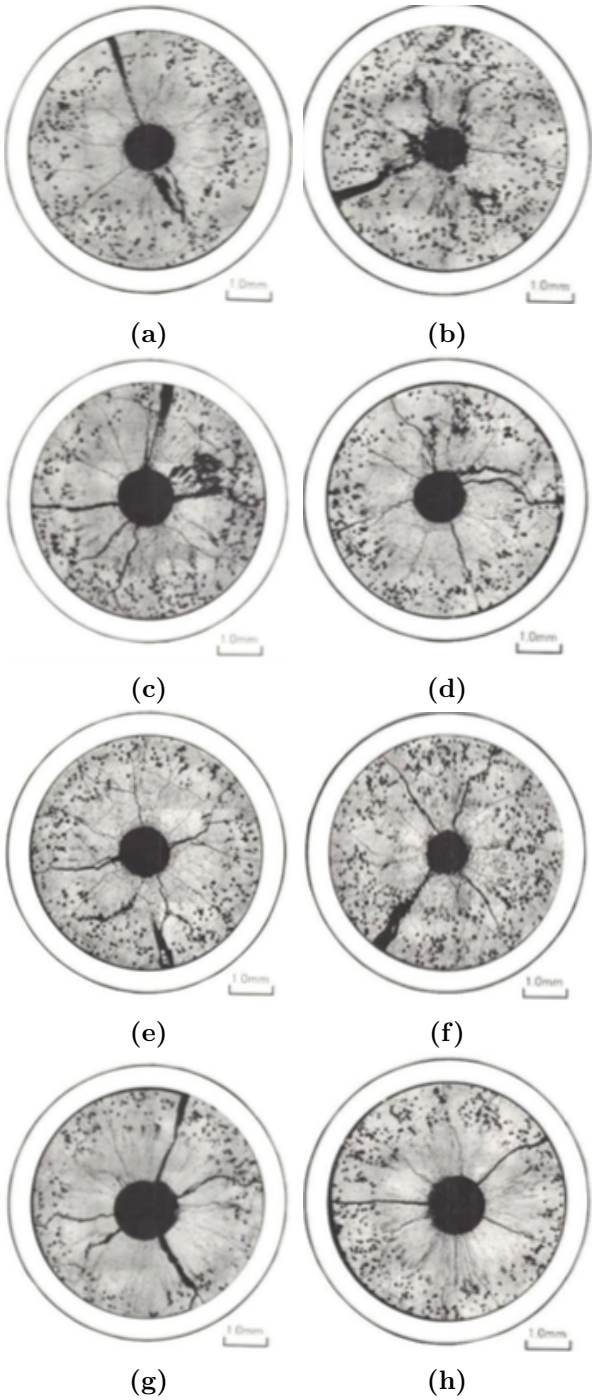

Figure 5.3: Ceramographs from: PTM001 (gap size of 160 μm, initial (Oxygen-to-Metal) O/M ratio 1.98) at +33 mm (a) and +97 mm (b) from the mid plane; PTM002 (initial gap size of 210 μm, initial O/M ratio 1.98) at +27 mm (c) and +97 mm (d) from the mid plane; PTM003 (gap size of 160 μm, initial O/M ratio 1.96) at +33 mm (e) and +97 mm (f) from the mid plane; and PTM010 (gap size of 210 μm, initial O/M ratio 2) at +25 mm (g) and +97 mm (h) from the mid plane [27].

CHAPTER 6. CALCULATION RESULTS

In this Chapter, the calculation results for the fission gas release, pore migration and oxygen redistribution are presented.

6.1 Fission gas release

In this Section, the calculations results, obtained with BISON, are presented. It is the first time that this fuel performance code is validated against fast MOX cases. In Figs. 6.1-6.4 two different cases have been examined:

- A first one that considers the standard BISON version without any limitation on bubble growth and coalescence processes;
- A second case that takes into account the lower limit for the bubble number density at the grain boundary N_{lim} (Eq. 3.1) dependent on the grain radius proposed in this work with the diffusion coefficient for fission gasses presented by Turnbull et al. [15].

As shown in Figs. 6.1-6.4, one can observe that introducing N_{lim} according to Eq. 3.1 the fission gas release prediction is closer to the experimental data. These results are in agreement with what we were expecting, and indicate that the limitation introduced describes better the physical limit of processes that occur on one hand at extreme conditions for UO_2-LWR and on the other hand at typical operational conditions for fast reactor MOX fuel.

In order to discuss the effect of grain-size on the results, I propose a sensitivity analysis with an analytical approach. This analysis was performed with reference to the model illustrated by Pastore et al. [36, 37].

With the purpose of seeing the effects to the final release due to the perturbation, generated adding a quantity δC of gas, it is necessary to linearize the equations

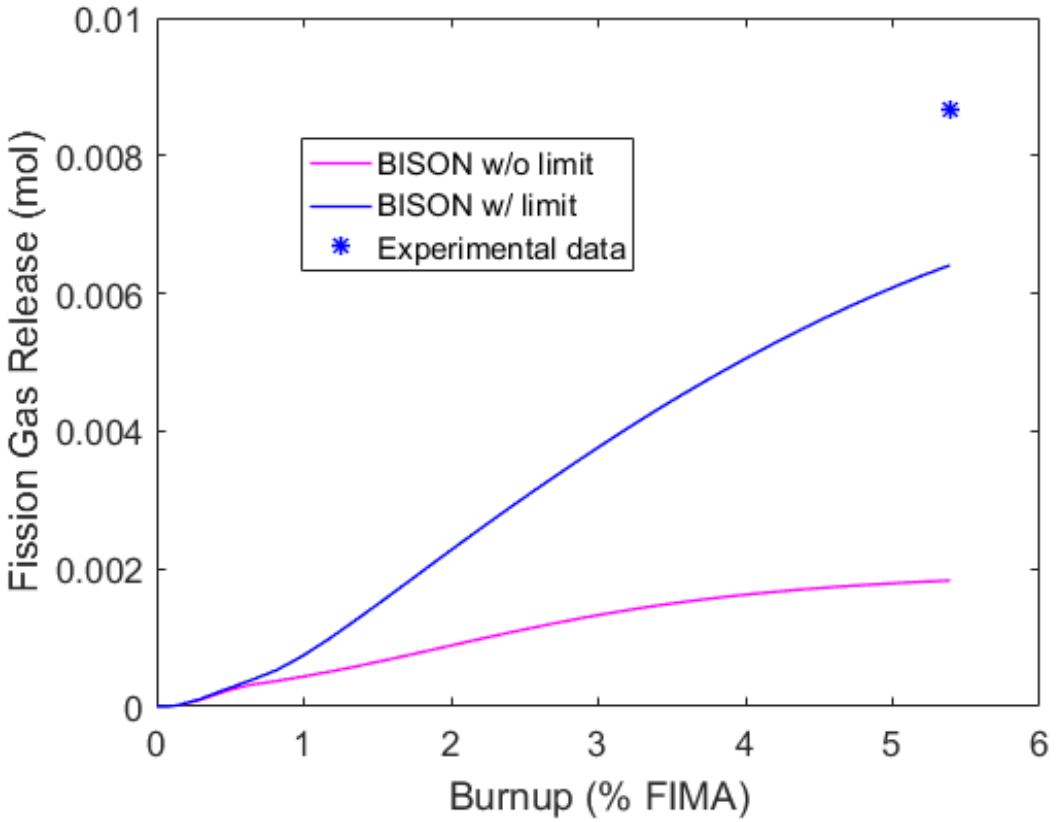

Figure 6.1: *FGR* during the irradiation for the fuel pin L09 from the FO-2 assembly irradiated in the FFTF reactor. The *FGR* is not expressed in percentage because Gilpin et al. [12] provides just the volume and the composition of the gasses after puncturing. A constant grain radius of 10 μm has been assumed. The purple line refers to the standard BISON version without any limitation on bubble growth and coalescence processes; the blue line corresponds to the case that uses the lower limit for the bubble number density at the grain boundary N_{lim} (Eq. 3.1), corresponding to a value of 5.6×10^{10} bubbles m^{-2}.

(presented by Pastore et al. [36, 37] and seen in Section 2.1) that govern the fission gas behaviour. Hence, once linearized, Eq. 2.1 that describes the intra-granular diffusion becomes:

$$\frac{\partial \delta C}{\partial t} = D_{\text{eff}} \frac{1}{a} \frac{\partial^2 \delta C}{\partial r^2}\Big|_a \tag{6.1}$$

Eq. 6.1 shows an inverse proportionality between the diffusion phenomenon and the grain radius a. In fact, the larger the grain, the longer the average diffusion path to

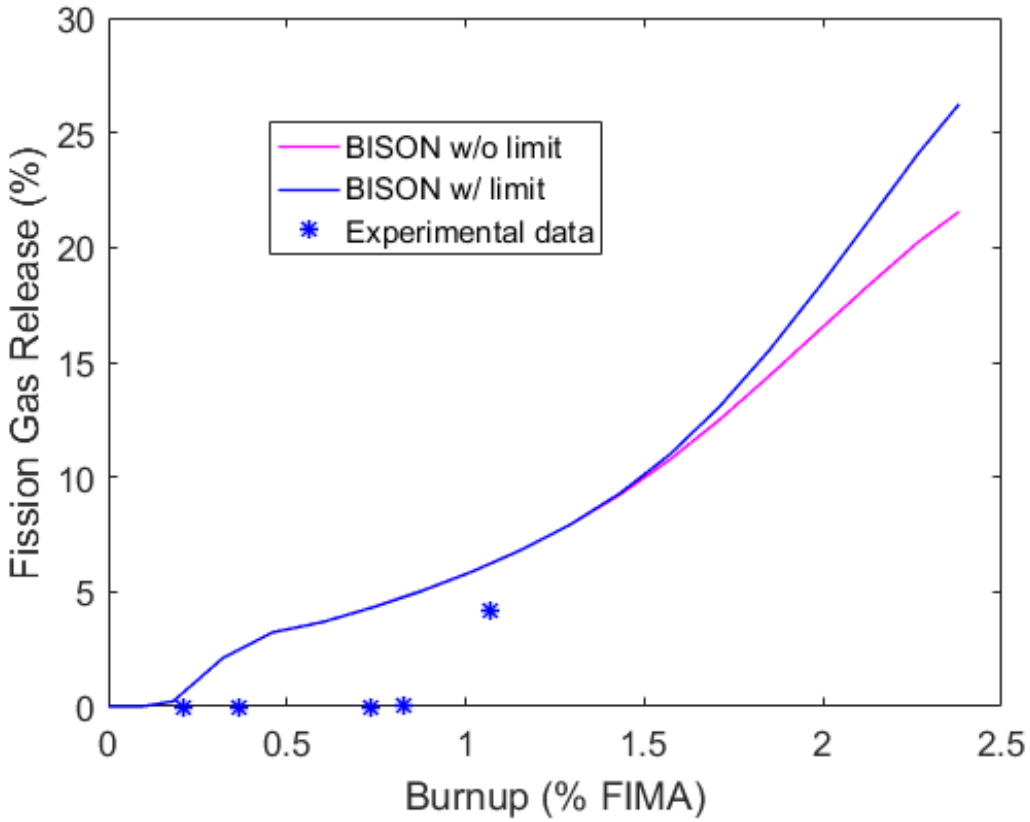

Figure 6.2: *FGR* during the irradiation for MK-I core irradiated at 50 MW in the JOYO reactor. Experimental data from Shimada et al. [41] and Karahan [16]. A constant grain radius of 8 μm has been assumed. The purple line refers to the standard BISON version without any limitation on bubble growth and coalescence processes; the blue line corresponds to the case that uses the lower limit for the bubble number density at the grain boundary N_{lim} (Eq. 3.1), corresponding to a value of $8.7{\times}10^{10}$ bubbles m^{-2}.

the grain boundary.

After linearizing all the equations governing the grain boundary gas behaviour (Eqs. 2.4-2.8) presented by Pastore et al. [36, 37], referring to the fractional coverage $F = F_{\text{sat}} = 0.5$ (/) as stationary steady state point, and adding a δC as perturbation to the system, one obtains:

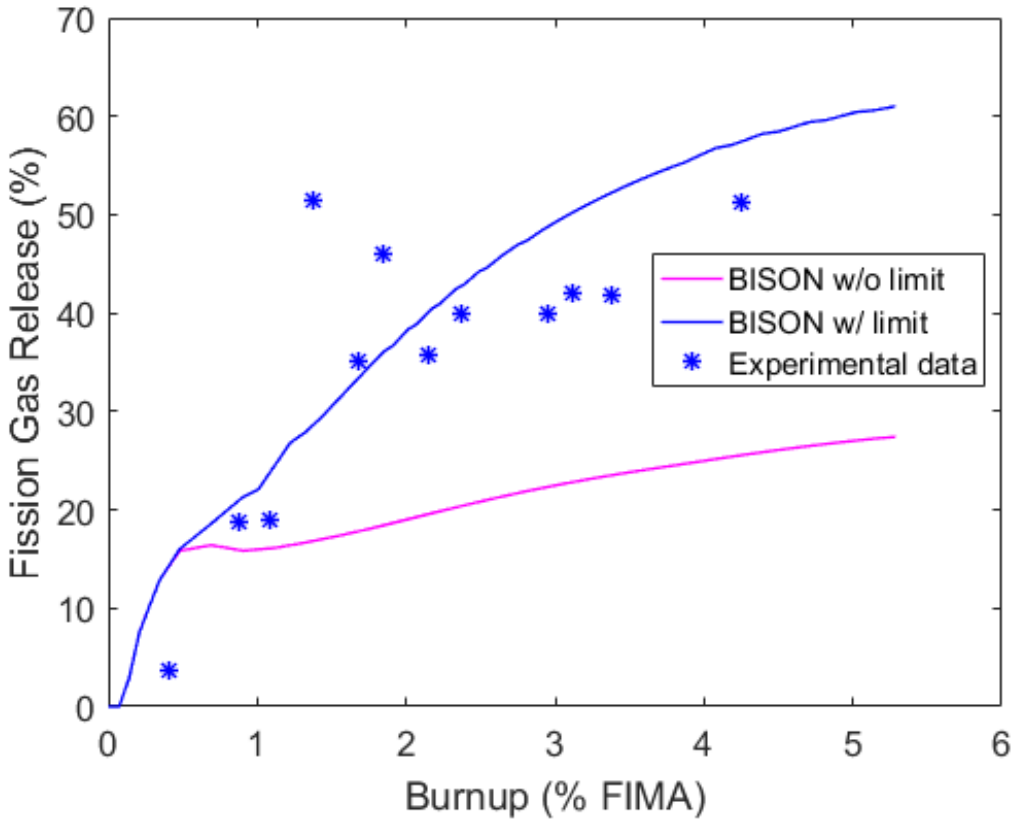

Figure 6.3: *FGR* during the irradiation for MK-I core irradiated irradiated at 75 MW in the JOYO reactor. Experimental data from Shimada et al. [41] and Karahan [16]. A constant grain radius of 8 μm has been assumed. The purple line refers to the standard BISON version without any limitation on bubble growth and coalescence processes; the blue line corresponds to the case that uses the lower limit for the bubble number density at the grain boundary N_{lim} (Eq. 3.1), corresponding to a value of $8.7{\times}10^{10}$ bubbles m^{-2}.

$$\delta n_{\text{fgr}} = \frac{n_0 N_0}{A_{\text{gf},0}} \left[\left(\omega + \frac{2\pi D_v \delta_g}{\Omega S n_{\text{v},0}} t \right) \left(\frac{\delta C}{3 N_0} a \right) \right]^{2/3} \tag{6.2}$$

where δn_{fgr} (atoms) is the variation of number of fission gas atoms released to the fuel rod free volume after the perturbation, n_0 (atoms bubble^{-1}) is the number of fission gas atoms per grain-face bubble in the stationary point, N_0 (bubbles m^{-2}) is number density of grain-face bubbles per unit surface in the stationary point, $A_{\text{gf},0}$ (m^2) is the

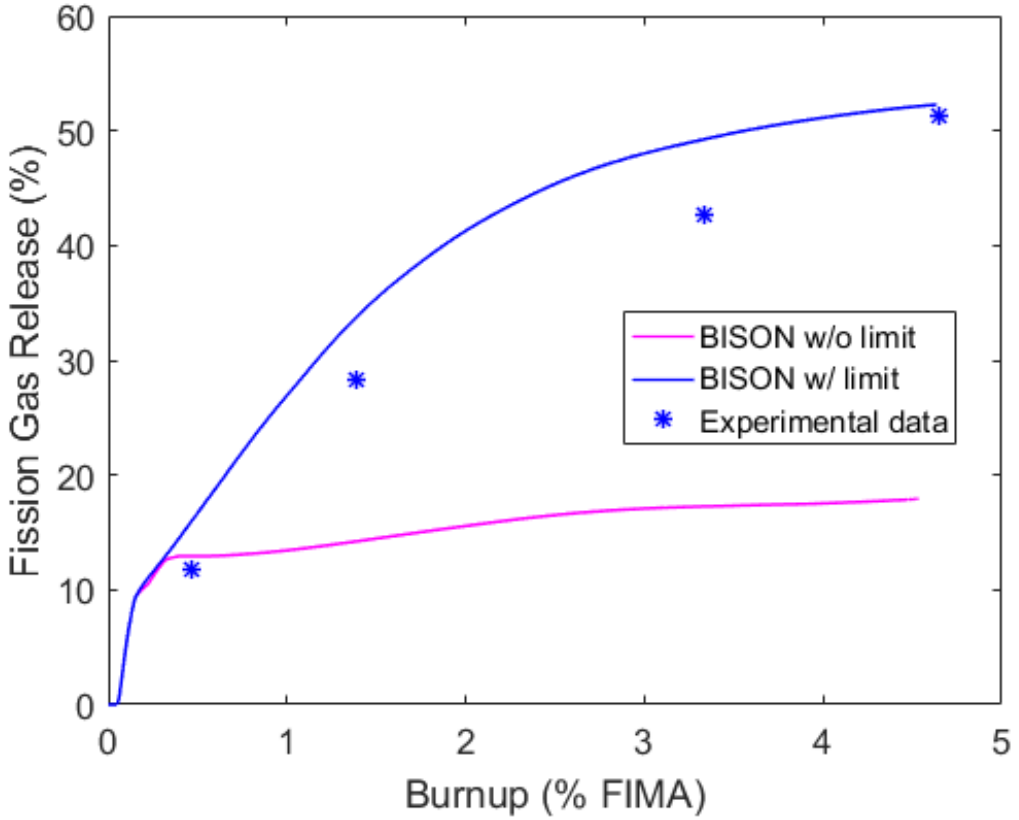

Figure 6.4: *FGR* during the irradiation for MK-II core irradiated in the JOYO reactor. Experimental data from Shimada et al. [41] and Karahan [16]. A constant grain radius of 8 μm has been assumed. The purple line refers to the standard BISON version without any limitation on bubble growth and coalescence processes; the blue line corresponds to the case that uses the lower limit for the bubble number density at the grain boundary N_{lim} (Eq. 3.1), corresponding to a value of 8.7×10^{10} bubbles m^{-2}.

projected area of grain-face bubbles, ω (m^3) is the Van der Waals' volume of a fission gas atom, D_v (m^2 s^{-1}) is the vacancy diffusion coefficient in grain boundaries, δ_g (m) is the thickness of the diffusion layer in grain boundaries, Ω (m^3) atomic (vacancy) volume in grain-boundary bubbles, S (-) is a model parameter (that depends on the fractional coverage), $n_{\text{v},0}$ (vacancies bubble^{-1}) is the number of vacancies per grain-face bubble in the stationary point and t (s) is the time.

Performing a derivative of Eq. 6.2 with respect to the grain radius a one can obtain:

$$\frac{\partial \delta n_{\mathrm{fgr}}}{\partial a} = \frac{n_0 N_0}{A_{\mathrm{gf},0}} \left[\left(\omega + \frac{2\pi D_v \delta_g}{\Omega S n_{\mathrm{v},0}} t \right) \left(\frac{\delta C}{3 N_0} \right) \right]^{2/3} \left(\frac{2}{3 a^{1/3}} \right) \tag{6.3}$$

Eq. 6.2 describes the dependency of the FGR from the grain boundaries to the rod free volume on $a^{2/3}$. This effect is due to the decrease of the surface-to-volume ratio of the grain with the increase of the grain radius a. Looking at the derivative (Eq. 6.3) one can observe that this process is limited since the $\frac{\partial \delta n_{\mathrm{fgr}}}{\partial a}$ follows a law proportional to $a^{-1/3}$.

After this analytical study, I also investigated the effect of the grain-size on the results performing some further simulations. Fig. 6.5 shows a comparison between the case using the current version of BISON without any limitation on bubble growth and coalescence processes and the one with N_{lim} proposed in this work, also considering two different constant values of grain radius: 5 and 10 μm for the L09 pin; 4 and 8 μm for MK-I and MK-II cores. These values lay in the range that goes from 4 to 10 μm referred to a realistic size for the grain characteristic dimension after the restructuring [2].

Looking at Fig. 6.5, one can make some observations.

- The FGR for the cases using the limitation N_{lim} with a lower grain radius (black line) is higher than in the case with a higher grain radius (blue line). This result means that the effect of a smaller grain on the improved coalescence due to the dependence of N_{lim} on a (Eq. 3.1) and on the intra-granular diffusion (Eq. 6.1) is stronger than the contrary effect of a on the grain boundary gas behavior seen in Eq. 6.2.

- In Figs. 6.5a-6.5b, even if there is no limitation to bubble growth and coalescence, the intra-granular diffusion effect (Eq. 6.1) prevails again (red line versus purple line) on the surface-to-volume effect described for the grain boundary gas behavior (Eq. 6.2). However Fig. 6.5c shows that this is valid only until a certain value of burnup (the purple line crosses the red one). This happens because at a sufficiently high level of burnup the gasses accumulate on the grain boundaries, removing significance to the intra-granular diffusion respect to the surface-to-volume effect.

- Again up to a certain burnup the case with N_{lim} with larger grain (blue line) has a lower release compared to the case with no limitations and with a smaller grain (red line). This shows that until that value of burnup the intra-granular effect is stronger, but beyond that point the effect on the grain boundary gas

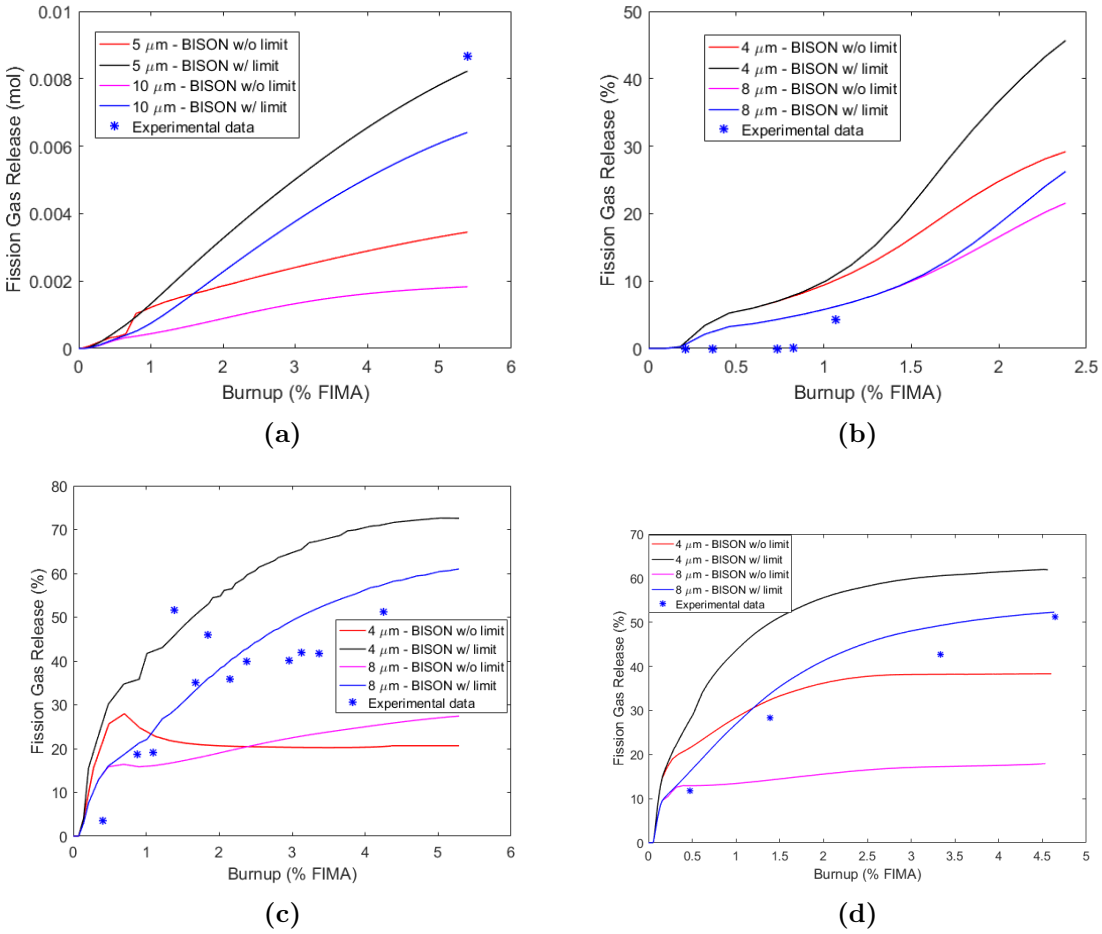

Figure 6.5: Sensitivity analysis performed varying the grain radius in a realistic range after the restructuring (from 4 μm to 10 μm). Fig. 6.5a refers to the fuel pin L09 from the FO-2 assembly; Figs. 6.5b-6.5c show the sensitivity analysis for MK-I core irradiated at 50 MW and at 75 MW respectively, while the simulations for MK-II core are illustrated in Fig. 6.5d.

behavior (Eq. 6.2) is dominant. Furthermore, beyond that level of burnup, the blue line reaches the lower bound of bubbles at the grain-boundary (Eq. 3.1), and, as consequence, its release results higher. This is shown in Fig. 6.5a and Fig. 6.5c, while in Fig. 6.5b a sufficiently high level of burnup is not reached.

6.2 Pore migration

Utilizing the pore migration model implemented in BISON and described in Section 3.2 it has been possible to simulate the central void formation for the L09 fuel pin and for the pins irradiated in the B14 test.
Due to the heavy mesh density required to resolve central void formation, a multi-application approach is presented, where the equation for porosity is separated from the energy equation and solved on separate meshes. The results from each domain are transferred back and forth, in a Picard iteration scheme, which ensures tight convergence. This feature has been used for its numerical stability.
All the fuel rods were modeled as a smeared fuel pellet stack for the integral simulations. The geometric parameters specified in Table 5.1 were used to create the meshes for these simulations. The smeared fuel was meshed as a single smeared fuel column with 20 radial elements and 100 axial elements.

Fig. 6.6 shows the comparison of all the specimens (both subjected to the X-ray CT and to the destructive examination) with the calculation results in a range of $\sigma \pm 20\%$. In these simulations I studied the impact on the results of the porosity threshold in order to consider a void. Fig. 6.6a refers to the same threshold used by Novascone et al [32] ($P > 0.3$); while Fig. 6.6b uses $P > 0.75$. It can be observed that there are not many differences between the results of these two different thresholds. This is due to the steep gradient of porosity that defines the central void region from the restructured zone. However, since the condition $P > 0.75$ matches better with the experimental data, I decided to consider this threshold for all the next analysis of this work.

In Figs. 6.7-6.11 it is possible to observe the steep gradient of porosity.

The black dotted line in Figs. 6.7-6.11 refers to the measured central void in the experiments, while the red dotted line (Fig. 6.7) provides the delimitation between the restructured and the as-fabricated regions. Only Gilpin et al. [12] provides information for the restructured region. As shown in these figures, performed at the end of each simulation, BISON is ableto describe this phenomenon with good results. As expected, each porosity profile is consistent with the temperature gradient which it refers to (Fig. 6.7b, Fig. 6.7d, Fig. 6.7f, Fig. 6.8b, Fig. 6.8d, Fig. 6.9b, Fig. 6.9d, Fig. 6.10b, Fig. 6.10d, Fig. 6.11b and Fig. 6.11d).
The tiny oscillations observed in some simulations like in Fig. 6.7a and Fig. 6.7c can be fixed with a finer mesh.

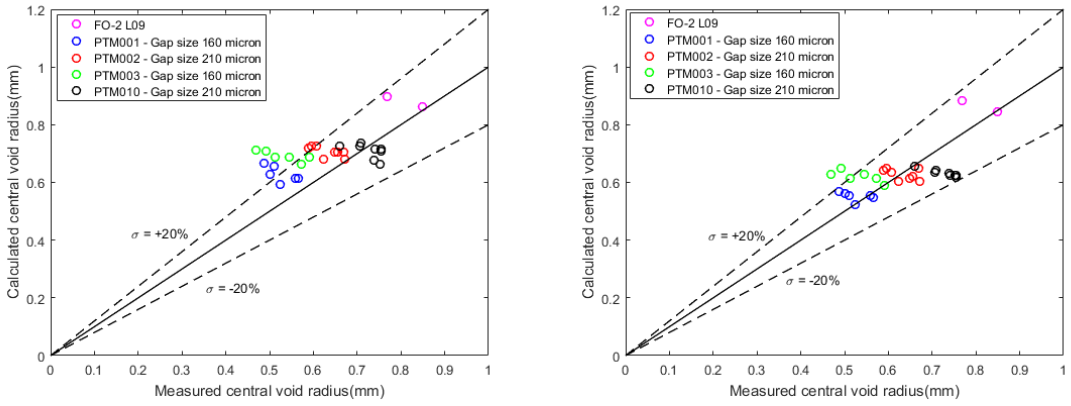

Figure 6.6: Central void radius (mm) measured versus calculated for FO-2 L09 and B14 experiment. Both the figures show all the specimens (both subjected to the X-ray CT and to the destructive examination) compared with the calculations in a range of $\sigma \pm 20\%$. The impact on the results of the porosity threshold in order to consider a void has been analyzed as follows: Fig. (a) refers to the same threshold used by Novascone et al. [32] ($P > 0.3$); while (b) uses $P > 0.75$.

6.2.1 B14 offset cases with 2D disk simulations

As shown by the ceramographs (Maeda, 2011 [27]) the fuel pins with an as-fabricated larger initial gap (PTM002 and PTM010) exhibit an off-centerd restructuring in the samples at the upper axial level of the fuel column (Fig. 5.3d and Fig. 5.3h). In order to reproduce this effect with BISON a 2D half disk mesh has been chosen as shown in Fig. 6.12. A high refined mesh (50 and 200 elements in the radial and circumferential directions, respectively) in the fuel block is required in order to avoid convergence issues.

Fig. 6.13 and Fig. 6.14 show the calculation results of the simulations performed with BISON in order to reproduce the off-centered void in the fuel pins PTM002 and PTM010 irradiated in the B14 experiment.

Table 6.1 shows the comparison between measured and calculated offset central void for the fuel pins PTM002 and PTM010. The offset from the center is normalized

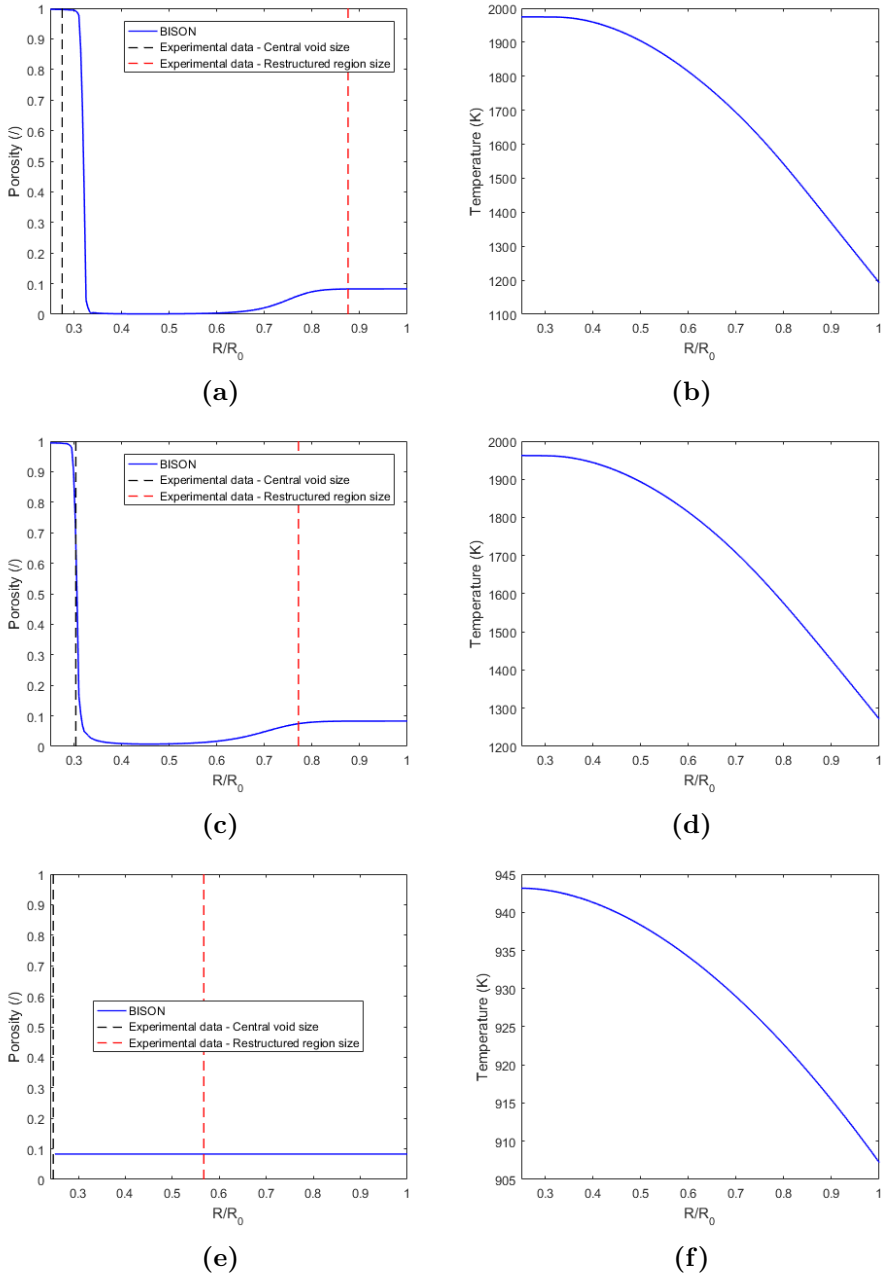

Figure 6.7: L09 fuel pin integral fuel rod simulation results. Porosity and temperature profiles over the relative radial position at the end of the simulations are shown: (a) and (b) refer to the sample H (mid plane); (c) and (d) to the sample J (3/4 of the fuel column); and (e) and (f) to sample L (the top of the fuel stack). R_0 is the outer radius of the fuel pellet. The black dotted line refers to the central void size measured in the experiment, where the pre-irradiated inner radius is 0.685 mm. The red dotted line instead provides the restructured region size measured at the end of the experiment [12]. Every curve begins from the inner radius of the annular fuel.

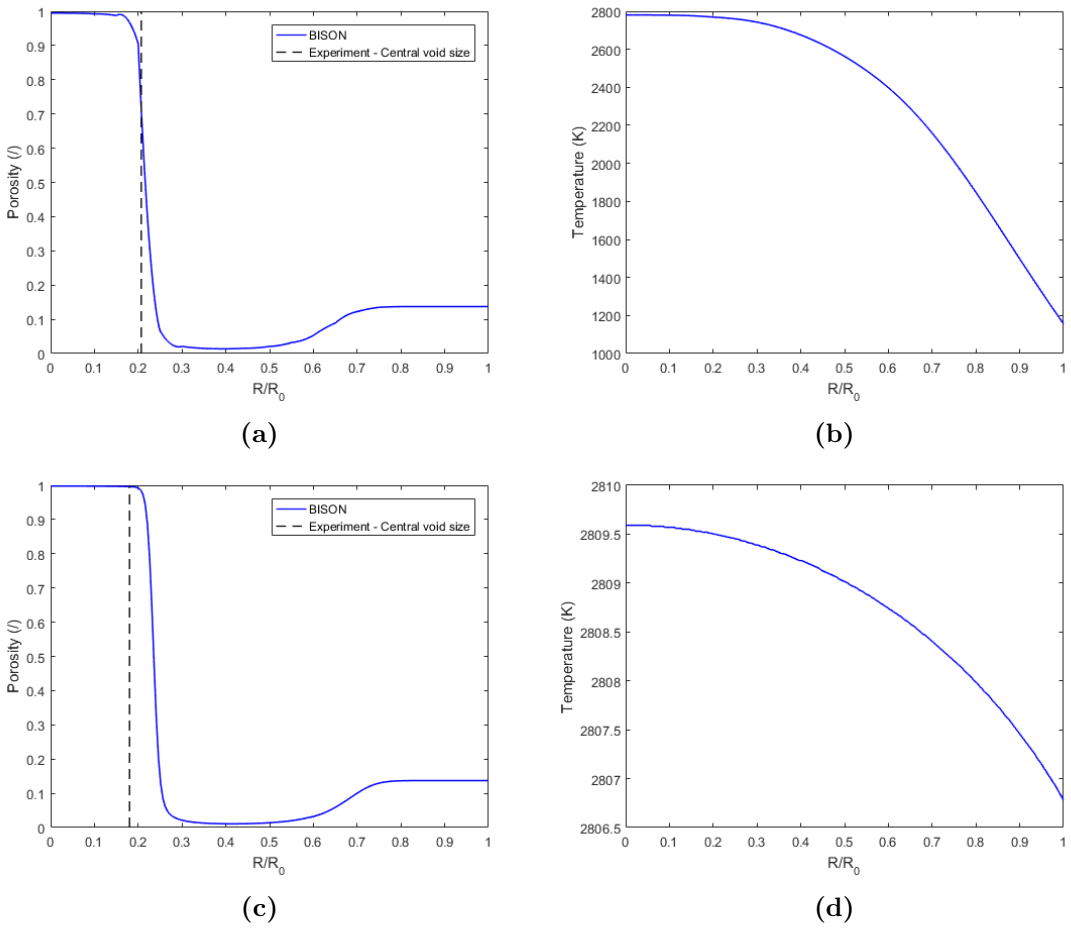

Figure 6.8: Calculation results for integral fuel rod simulation of the PTM001 fuel pin. Porosity and temperature profiles over the relative radial position for the simulations of the two samples destructively examined are shown: (a) and (b) refers to the sample at +33 mm from the core midplane; (c) and (d) to the sample at +97 mm from the core mid plane. R_0 is the outer radius of the fuel pellet. The black dotted line refers to the central void size measured in the experiment [27].

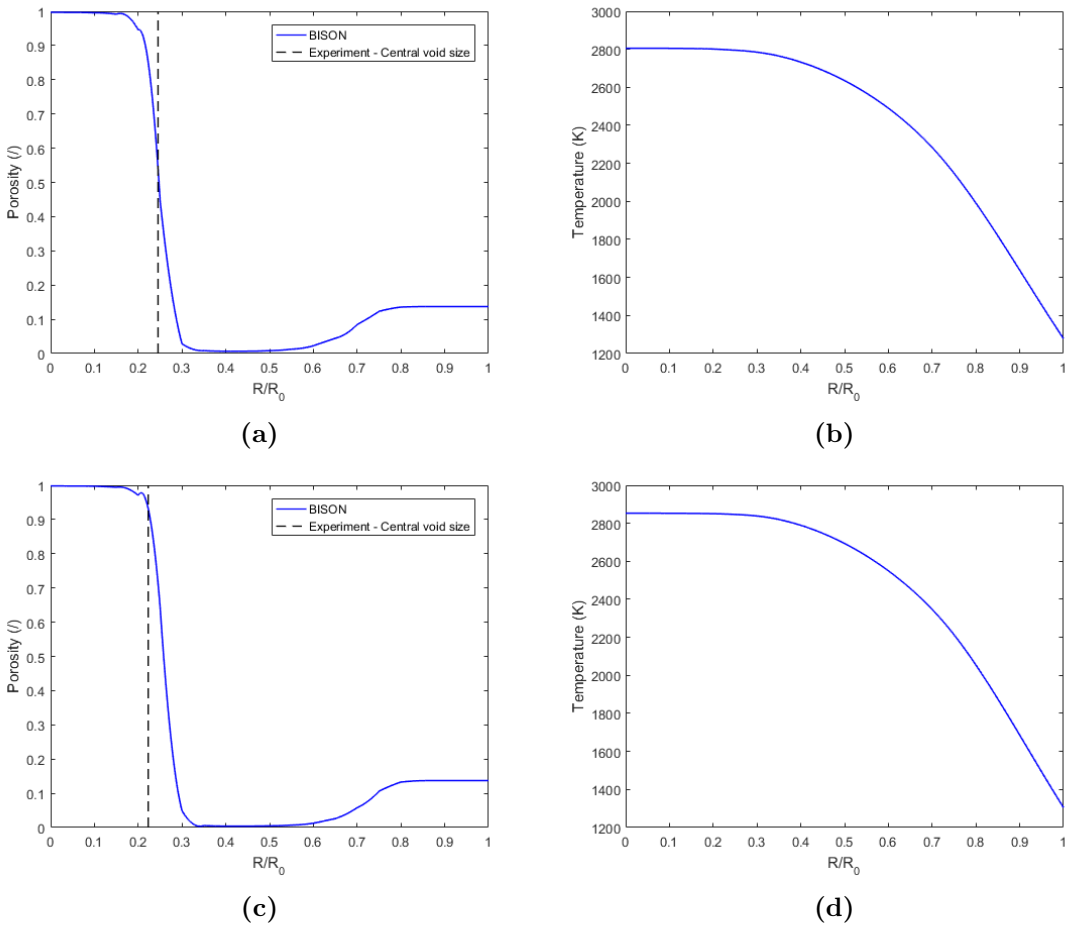

Figure 6.9: Calculation results for integral fuel rod simulation of the PTM002 fuel pin. Porosity and temperature profiles over the relative radial position for the simulations of the two samples destructively examined are shown: (a) and (b) refers to the sample at +27 mm from the core midplane; (c) and (d) to the sample at +99 mm from the core mid plane. R_0 is the outer radius of the fuel pellet. The black dotted line refers to the central void size measured in the experiment [27].

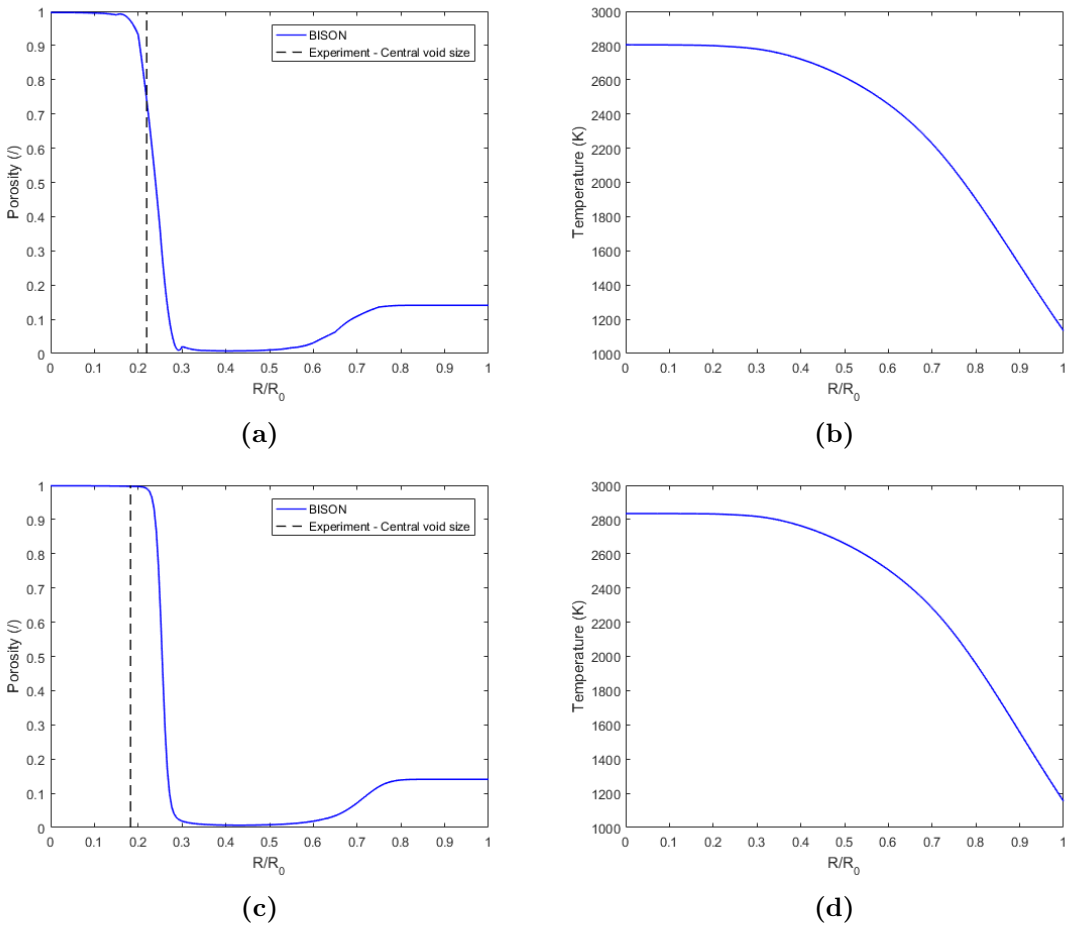

Figure 6.10: Calculation results for integral fuel rod simulation of the PTM003 fuel pin. Porosity and temperature profiles over the relative radial position for the simulations of the two samples destructively examined are shown: (a) and (b) refers to the sample at +33 mm from the core midplane; (c) and (d) to the sample at +97 mm from the core mid plane. R_0 is the outer radius of the fuel pellet. The black dotted line refers to the central void size measured in the experiment [27].

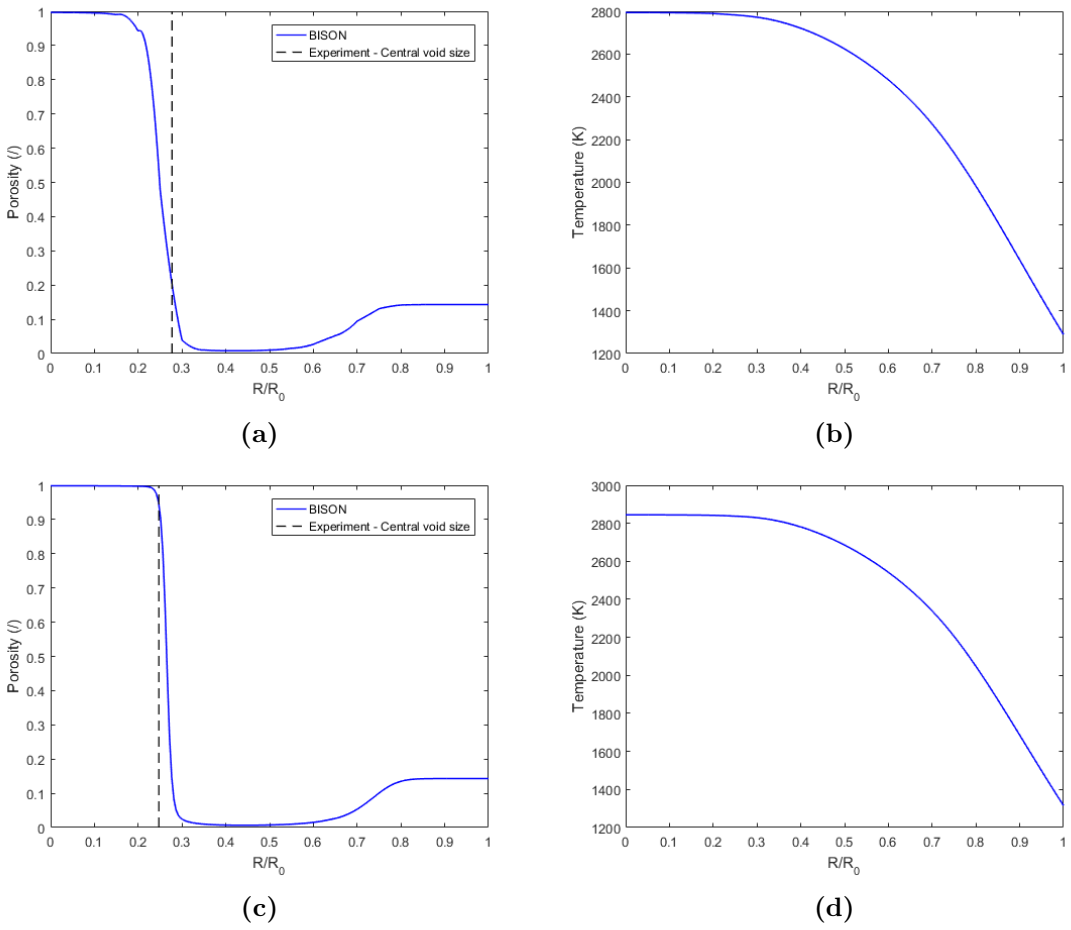

Figure 6.11: Calculation results for integral fuel rod simulation of the PTM010 fuel pin. Porosity and temperature profiles over the relative radial position for the simulations of the two samples destructively examined are shown: (a) and (b) refers to the sample at +25 mm from the core midplane; (c) and (d) to the sample at +97 mm from the core mid plane. R_0 is the outer radius of the fuel pellet. The black dotted line refers to the central void size measured in the experiment [27].

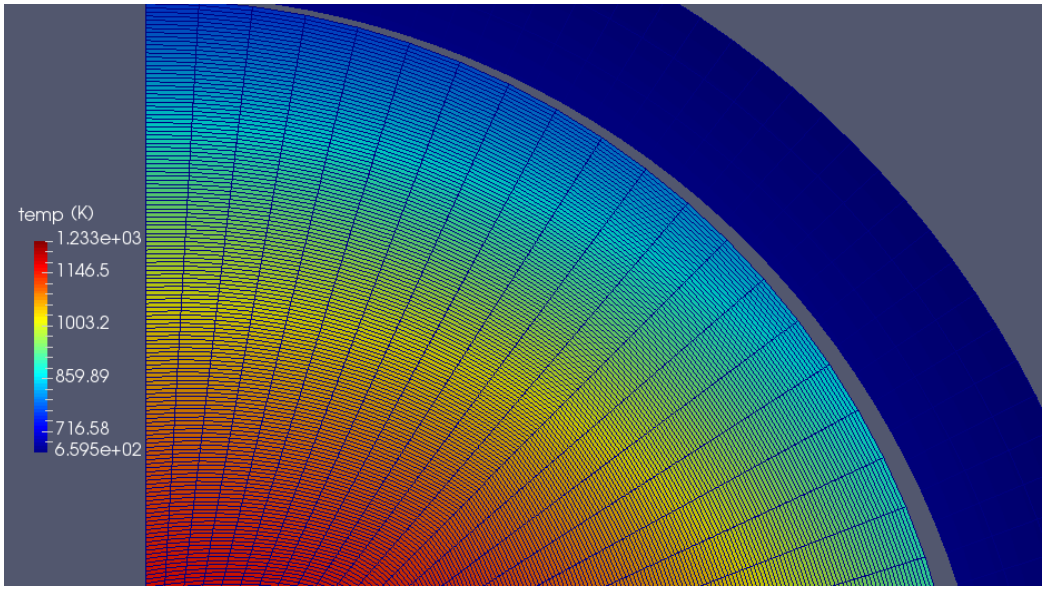

Figure 6.12: A section, with a temperature contour plot, of the half disk mesh utilized to describe the offset problem of the pin PTM002 from the B14 experiment.

to the fuel diameter. Here, one can observe that the model predicts with a good accuracy the size of the void, but the magnitude of the predicted offset from the center needs more investigation.

Table 6.1: Comparison between measured and calculated offset central void for the fuel pins PTM002 and PTM010.

		PTM002	PTM010
Measured	Central void diameter (mm)	1.19	1.32
	Offset/Fuel diameter (/)	0.03	0.035
Calculated	Central void diameter (mm)	1.249	1.31
	Offset/Fuel diameter (/)	0.08	0.085

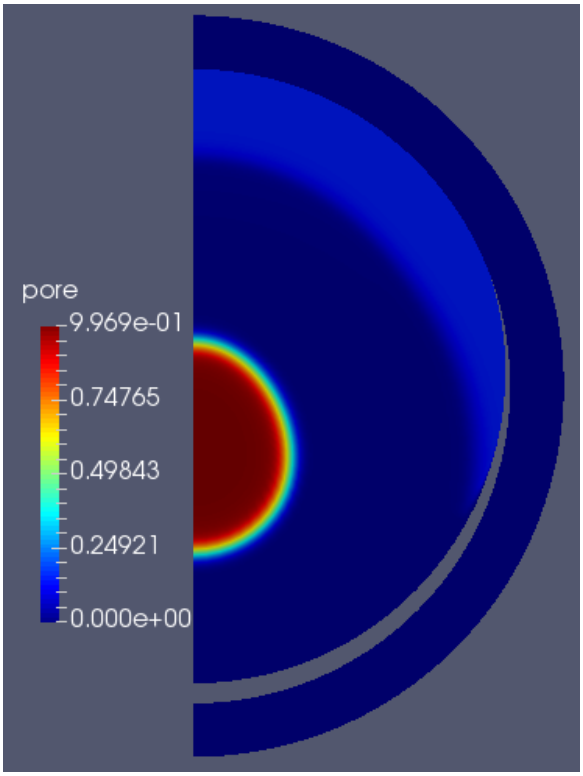

Figure 6.13: Calculation results for the offset case at +99 mm from the core mid plane for the fuel pin PTM002. The picture shows a porosity contour in the restructured fuel pellet.

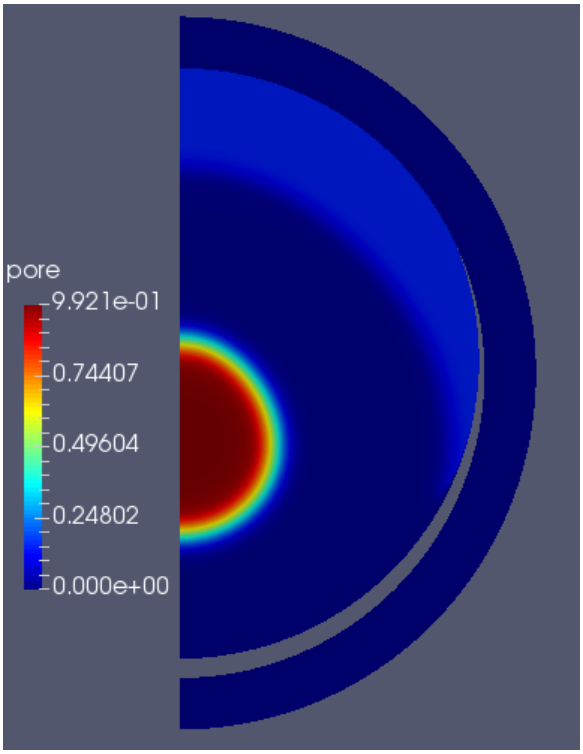

Figure 6.14: Calculation results for the offset case at +97 mm from the core mid plane for the fuel pin PTM010. The picture shows a porosity contour in the restructured fuel pellet.

6.3 Oxygen redistribution

After implementing the model described by Lassmann [26]; Section 3.3), it has been decided to test it with two simple one-dimensional examples, in order to study both the fuel cases (hypo- and hyper-stoichiometric).
Fig. 6.15 shows the results for two examples: the former for an hypo-stoichiometric fuel (Fig. 6.15a, typical for MOX fuels) and the latter about an hyper-stoichiometric case (Fig. 6.15b). In these examples a typical value of the fraction of plutonium q_0 for fast MOX fuels has been considered and it is equal to 25 Pu/(U+Pu) at%. The figures describe a behaviour of the oxygen redistribution very close to the one expected from the theory [33].

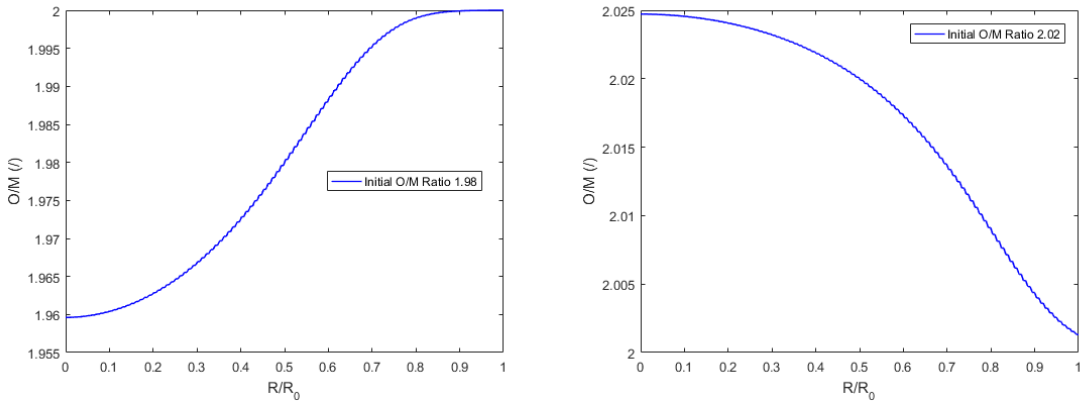

(a) **(b)**

Figure 6.15: (a) Hyper-stoichiometric case (O/M>2); (b) hypo-stoichiometric case (O/M<2). In both the examples it has been considered a solid pellet with a common value for fast MOX fuels for q_0 equal to 25 Pu/(U+Pu) at.%. The examples were performed just in a 1D problem.

In all the experiments analyzed so far in this work only B14 test presents useful data [13] for a validation of the oxygen redistribution model. These validation results are shown in Fig. 6.16. Since the few data coming from Ikusawa et al. [13] compare the oxygen-to-metal ratio O/M with the oxygen potential, for this validation it has been necessary to extrapolate the oxygen potential from the oxygen redistribution results performed with BISON. In order to accomplish this task, the following equation provided by Kato et al. [19] that puts in relation the O/M ratio with the oxygen

partial pressure p_{O_2}, has been taken into account:

$$O/M = 2 + \left[exp\left(-\frac{22.8 + 84.5 C_{Pu}}{R} \right) exp\left(\frac{105000}{RT} \right) (p_{O_2})^{1/2} \right] - K^{-1/5} \tag{6.4}$$

where the third term K has the definition:

$$\begin{aligned} K = & \left\{ exp\left(\frac{44 + 55.8 C_{Pu}}{R} \right) exp\left(-\frac{376000}{RT} \right) (p_{O_2})^{-1/2} \right\}^{-5} \\ & + \left\{ \left[exp\left(\frac{68.8 + 131.3 C_{Pu}}{R} \right) exp\left(-\frac{515000}{RT} \right) \right]^{1/2} (p_{O_2})^{-1/4} \right\}^{-5} \\ & + \left\{ \left[2exp\left(\frac{153.5 + 96.5 C_{Pu} + 331 C_{Pu}^2}{R} \right) exp\left(-\frac{891000}{RT} \right) \right]^{1/3} (p_{O_2})^{-1/3} \right\}^{-5} \\ & + \left\{ \left[exp\left(\frac{111.2 + 20 C_{Pu}}{R} \right) exp\left(-\frac{445000}{RT} \right) \right]^{1/2} (p_{O_2})^{-1/4} \right\}^{-5} + \left(\frac{C_{Pu}}{2} \right)^{-5} \end{aligned} \tag{6.5}$$

In Eqs. 6.4-6.5, T (K) is temperature, R (J mol^{-1} K^{-1}) the gas constant and C_{Pu} the plutonium content defined as:

$$C_{Pu} = \frac{Pu}{U + Pu + Am} + 2.5 \frac{Am}{U + Pu + Am} \tag{6.6}$$

Finally, in order to compute the oxygen potential $\Delta\overline{G}_{O_2}$ (J mol^{-1}), the following formulation is considered:

$$\Delta\overline{G}_{O_2} = RTln\,(p_{O_2}) \tag{6.7}$$

In Fig. 6.16, according to Ikusawa et al. [13] two kinds of MOX fuel have taken into account: the former containing Am (66 wt% of U, 31.6 wt% of Pu and 2.4 wt% of Am) and the latter just U and Pu (70 wt% of U and 30 wt% of Pu).

The two results, obtained with BISON and shown in Fig. 6.16 (green and black circles), refer to two samples at a normalized radius of 0.33 at a temperature of 1673 K (the same of the experiment performed by Ikusawa et al. [13]).
The results are consistent with the experimental data (Fig. 6.16) because the simulation performed with a fuel bearing americium presents an higher value of oxygen potential, since this minor actinide tends to increase this parameter. This feature can be also observed looking at Eq. 6.6.

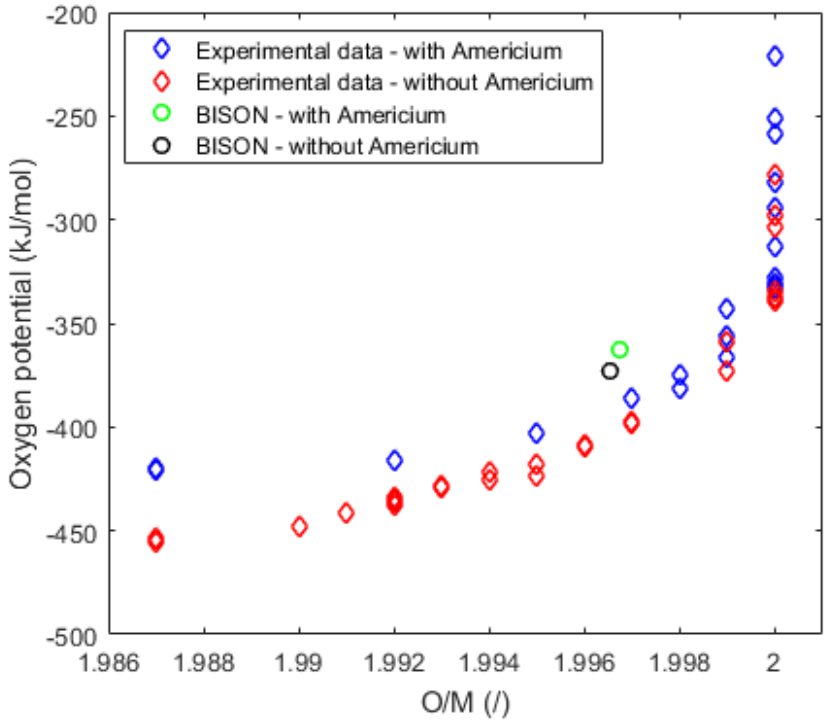

Figure 6.16: Calculation results for oxygen potential in B14 experiment. Validating the oxygen redistribution implemented in BISON with the data from Ikusawa et al. [13] in two kinds of MOX fuel: the former containing Am (66 wt% of U, 31.6 wt% of Pu and 2.4 wt% of Am) and the latter just U and Pu (70 wt% of U and 30 wt% of Pu).

CHAPTER 7. CONCLUSIONS AND FUTURE PROSPECTS

In this thesis, I analyzed three important phenomena that take place (or they are enhanced) in the MOX fuel under the harsh operative conditions of fast reactors.

For the fission gas release I proposed an improvement to the current version of the model already implemented in BISON. Hence, I focused the work on testing this new feature in LWR conditions to demonstrate the effective transferring of predictive capability of the modified model in these conditions, and I validated it against integral irradiation experiments in fast reactor conditions.
As for the fission gas release, the results obtained with the limit proposed in Eq. 3.1 are encouraging. In particular, they demonstrate (as shown in Chapter 4) that at low temperatures the grain-face bubble growth and the consequent coalescence are far from their physical limits (Fig. 4.1), while at higher ranges those limiting effects occur (Fig. 4.2). The sensitivity analysis performed highlights the strong dependency of this phenomenon on the grain size.
Future efforts can be invested in the validations of more cases, and in the analysis of other kind of MOX fuels as well. For example, the model of Pastore et al. [36, 37] could be improved taking into the heterogeneity effect of the MOX fuels, due to the presence of plutonium agglomerates, on the fission gas release. This could be done implementing into the present model the outcomes from the studies of Koo et al. [24] and of Ishida and Korei [14].
Another open issue is the development of a grain growth model able to describe better this phenomenon at high temperatures, especially after the restructuring in order to define also the columnar grain region. So far, all the grains have been considered as spheres, but this approximation can be valid only for as-fabricated and equiaxed grain regions. The columnar grains, instead, present a cylindrical shape, hence in this case all the equations involved should be described with cylindrical coordinates. This improvement could be also useful for the sensitivity analysis prospect, because a grain growth model can feed directly Eq. 3.1 and therefore used for a more accurate sensitivity analysis.

As for the pore migration, the work was focused only on the validation side, as the current model of Novascone et al. [32] implemented in BISON was never validated against integral irradiation experiment before. Also, I took the chance to study how this model describes a case of offset restructuring.
The results of Fig. 6.6 show a good prediction of the central void size compared to the experimental data. Because of the steep porosity gradient that defines the fuel/void

interface (Figs. 6.7-6.11), it is required to use a relatively high density mesh. So far, this is a limitation of the finite element model employed.
Being Figs. 6.13-6.14 a first attempt to describe the offset central void, the results shown are encouraging. Also in these cases, the model describes with a good level of accuracy the size of the void, but the magnitude of the predicted offset from the center calls for more investigations (Table 6.1). Anyway, further validation cases are required in the future works.
Lastly, other relationships for the most uncertain quantity (i.e., the pore velocity) should be investigated and compared with the one provided by Sens [40] and used in this work.

To model oxygen redistribution, BISON required a proper model in order to describe this phenomenon. I focused my efforts on the implementation of the model provided by Lassmann [26] in the code. After testing it with simple one-dimensional examples, I validated it against data coming from the B14 experiment [13].
The main difficulty encountered in this topic was to find some experimental data to perform a validation study. Albeit this represents a first attempt to validate the model, Section 6.3 shows stimulating results for further investigations.
Furthermore, for some future prospects and improvements, Eq. 3.8 could be updated taking into account other two terms:

- A source term s (atoms m^{-3} s^{-1}), that considers the fission of uranium and plutonium as an oxidative process, since the fission products cannot bind all the oxygen atoms liberated by fissions;
- A flux of oxygen term J (atoms m^{-2} s^{-1}) from the fuel towards the cladding, since when the fuel cladding interaction occurs, the oxygen starts to penetrate in the cladding from the inner surface.

Therefore, after these considerations, also made by Kleykamp [20, 21, 22], Eq. 3.8 would become:

$$\frac{\partial c}{\partial t} + \nabla \cdot N_{\mathrm{ox}} D_{\mathrm{ox}} \left(\nabla c + c \frac{Q}{RT^2} \nabla T \right) - \nabla J \left(T_{\mathrm{clad}}, Bu \right) + s \left(T, Bu \right) = 0 \tag{7.1}$$

According to Adamson [1], the flux term J depends strongly on the cladding temperature and for a stainless steel cladding examined in Adamson [1] below 500°C the cladding will not be subjected to oxidation from the inner side. The source term s depends on the burnup Bu. In particular, it is known that the O/M ratio increases with the burnup [20]. The oxygen potential is increasing too with the Bu, due to the increasing of the O/M ratio. Because of this increment of the oxygen potential, some fission products (like molybdenum) are not able to bind the free oxygen atoms

anymore (stagnation in the oxidation of the fission product Mo). This will lead to a further increment in the overall O/M ratio, and above some burnup levels, the fuel tends to become slightly hyper-stoichiometric [44].

APPENDIX

A. Analytic sensitivity analysis of grain boundary gas behavior

In this Appendix, the analytic sensitivity analysis of grain boundary gas behavior, presented in Section 6.1, is derived.
This Appendix follows the work flow of Pastore et al. [36, 37] linearizing all the equations that describe the grain-faces gas behavior in order to obtain a relationship between the release and the grain radius.
Given the perturbation of the number of fission gas atoms per grain-face bubble δn (atoms bubble^{-1}):

$$\delta n = \frac{a}{3N_0}\delta C, \tag{A.1}$$

the perturbation on the pressure of the gas in bubble δp can be written as:

$$\delta p = \frac{k_B T}{\Omega n_{\mathrm{v},0}}\delta n. \tag{A.2}$$

Then the linearization of the equation that describes the vacancy absorption/emission rate at a bubble is:

$$\frac{d(\delta n_v)}{dt} = \frac{2D_v\delta_g}{k_B T\Omega S}\delta p. \tag{A.3}$$

Integrating Eq. A.3 in the time between 0 and t, one can obtain:

$$\delta n_v = \frac{2D_v\delta_g}{k_B T\Omega S}\delta p \cdot t. \tag{A.4}$$

Since Pastore et al. [36, 37] considers the fission gas release n_{fgr} depending on the number density of grain-face bubbles per unit surface N (bubbles m^{-2}) and on the projected area A_{gf} (m^2), it is necessary to linearize the equations that describe these two quantities.
So given that $A_{\mathrm{gf}} \sim V_{\mathrm{gf}}^{2/3}$, one can say:

$$\delta A_{\mathrm{gf}} = \left(\omega\delta n + \Omega\delta n_v\right)^{2/3}. \tag{A.5}$$

While the perturbation on the number density of grain-face bubbles per unit surface δN obtained is:

$$\delta N = -2N_0^2\delta A_{\mathrm{gf}}. \tag{A.6}$$

Finally the linearization of the fission gas release can be analyzed as:

$$\frac{d\left(n_{\mathrm{fgr},0}+\delta n_{\mathrm{fgr}}\right)}{dt}=\left(n_0+\delta n\right)\frac{N_0+\delta N}{A_{\mathrm{gf},0}+\delta A_{\mathrm{gf}}}\frac{d\left(A_{\mathrm{gf},0}+\delta A_{\mathrm{gf}}\right)}{dt}. \tag{A.7}$$

After performing some calculations and simplifications one can obtain:

$$\frac{d\left(\delta n_{\mathrm{fgr}}\right)}{dt}=\frac{n_0 N_0}{A_{\mathrm{gf},0}}\frac{d\delta A_{\mathrm{gf}}}{dt}. \tag{A.8}$$

An integration between 0 and t leads to:

$$\delta n_{\mathrm{fgr}}=\frac{n_0 N_0}{A_{\mathrm{gf},0}}\delta A_{\mathrm{gf}}. \tag{A.9}$$

Superposition of Eqs. A.1, A.2, A.4,A.5, A.6 and A.9 yields the final result, seen also in Section 6.1:

$$\delta n_{\mathrm{fgr}}=\frac{n_0 N_0}{A_{\mathrm{gf},0}}\left[\left(\omega+\frac{2\pi D_v \delta_g}{\Omega S n_{\mathrm{v},0}}t\right)\left(\frac{\delta C}{3N_0}a\right)\right]^{2/3}. \tag{A.10}$$

B. Materials and behavioral models used in the input files

The following material and behavioral models were used within the BISON application code repository to complete the simulations shown in this work:

Material and behavioral models	Description and reference	Experiments
MOXPoreContinuity	Pore migration is modeled by applying the concept of pore conservation [32].	All
MOXPoreDiffusion	Pore migration is modeled by applying the concept of pore conservation [32].	All
MOXPoreVelocity	Computes pore speed according to Sens [40]	All
MOXOxygenDiffusion	Computes oxygen redistribution according to Lassmann [26].	B14 - PTM001
MOXOxygenToMetalRatio	Computes O/M ratio according to Lassmann [26].	B14 - PTM001
FissionRateMOX	Computes fission rate for fast MOX fuel considering porosity.	All
ThermalMAMOX	Computes the thermal conductivity for minor actinide fast MOX fuel [18].	All
ComputeFiniteStrainElasticStress	Computes stress using elasticity for finite strains.	All
MAMOXElasticityTensor	Sets the Young's modulus and Poisson's ration for MAMOX fuel using values from JAEA [17].	All
MAMOXThermalExpansionEigenstrain	Computes eigenstrain due to isotropic thermal expansion in MA-MOX fuel using Kato et al. [17] correlations.	All
Sifgrs	Computes both fission gas swelling and release [36].	FO-2, MK-I and MK-II

ThermalHT9	Computes thermal properties of HT9 martensitic steel [7, 51].	FO-2
ComputeIsotropicElasticityTensor	Computes a constant isotropic elasticity tensor with constant Young's modulus E and Poisson's ratio ν. Where for HT9 martensitic steel: $E = 1.88 \times 10^{11}$ Pa and $\nu = 0.236$.	FO-2
ComputeThermalExpansionEigenstrain	Computes eigenstrain due to thermal expansion with a constant coefficient. Where for HT9 martensitic steel the thermal expansion coefficient is: $\alpha = 1.2 \times 10^{-5}$ K^{-1}.	FO-2
HT9CreepUpdate	Steady-state thermal and irradiation creep for HT9 [7].	FO-2
Thermal316	Computes thermal properties of stainless steel 316 [29].	B14, MK-I and MK-II
SS316ElasticityTensor	Calculates the Young's modulus and Poisson's ratio for Stainless Steel 316 cladding using relations as a function of temperature.	B14, MK-I and MK-II
SS316ThermalExpansionEigenstrain	Computes eigenstrain due to thermal expansion for Stainless Steel 316 using a function [31] that describes the mean thermal expansion as a function of temperature.	B14, MK-I and MK-II
SS316CreepUpdate	Steady state creep as sum of thermal and irradiation creep, following the models of Altenbach and Gorash [3], and Garner and Porter [11].	B14, MK-I and MK-II

REFERENCES

[1] M.G Adamson. Mechanisms of Fuel-Cladding Chemical Interaction: Us interpretation, 1977.

[2] J.B. Ainscough, B.W. Oldfield, and J.O. Ware. Isothermal grain growth kinetics in sintered UO_2 pellets. *Journal of Nuclear Materials*, 49(2):117 – 128, 1973.

[3] Holm Altenbach and Yevgen Gorash. High-temperature inelastic behavior of the austenitic steel AISI type 316. In *Advanced Materials Modelling for Structures*, pages 17–30. Springer, 2013.

[4] K. Forsberg A.R. Massih. Calculation of grain boundary gaseous swelling in UO_2. *Journal of Nuclear Materials*, 377(2):406 – 408, 2008.

[5] C. Baker. The fission gas bubble distribution in uranium dioxide from high temperature irradiated SGHWR fuel pins. *Journal of Nuclear Materials*, 66(3):283 – 291, 1977.

[6] C. Baker. The migration of intragranular fission gas bubbles in irradiated uranium dioxide. *Journal of Nuclear Materials*, 71(1):117 – 123, 1977.

[7] Compiled by: IFR Property Evaluation Working Group. Metallic fuels handbook. Argonne National Laboratory, June 1988.

[8] J.-Y. Colle, J.-P. Hiernaut, T. Wiss, O. Beneš, H. Thiele, D. Papaioannou, V.V. Rondinella, A. Sasahara, T. Sonoda, and R.J.M. Konings. Fission product release and microstructure changes of irradiated MOX fuel at high temperatures. *Journal of Nuclear Materials*, 442(1):330 – 340, 2013.

[9] D. R. De Halas and G. R. Horn. Evolution of uranium dioxide structure during irradiation of fuel rods. *Journal of Nuclear Materials*, 8(2):207–220, March 1963.

[10] S.B. Fisher, R.J. White, P.M.A. Cook, S. Bremier, R.C. Corcoran, R. Stratton, C.T. Walker, P.K. Ivison, and I.D. Palmer. Microstructure of irradiated SBR MOX fuel and its relationship to fission gas release. *Journal of Nuclear Materials*, 306:153 – 172, 2002.

[11] FA Garner and DL Porter. Irradiation creep and swelling of AISI 316 to exposures of 130 dpa at 385–400 c. *Journal of Nuclear Materials*, 155:1006–1013, 1988.

[12] L.L. Gilpin, R.B. Baker, and S.A. Chastain. Evaluation of the advanced mixed oxide fuel test FO-2 irradiated in Fast Flux Test Facility, May 1989.

[13] Yoshihisa Ikusawa, Koji Maeda, Masato Kato, and Masayoshi Uno. Oxide-Metal ratio dependence of central void formation of mixed oxide fuel irradiated in fast reactors. *Nuclear Technology*, pages 83–95, 2017.

[14] Masayoshi Ishida and Yoshio Korei. Modeling and parametric studies of the effect of Pu-mixing heterogeneity on fission gas release from mixed oxide fuels of LWRs and FBRs. *Journal of Nuclear Materials*, 210(1):203 – 215, 1994.

[15] C. Wise J.A. Turnbull, R.J. White. The diffusion coefficient for fission gas atoms in uranium dioxide. *IAEA-TC-699/3.5*, 1988.

[16] Aydin Karahan. *Modeling of thermo-mechanical and irradiation behavior of metallic and oxide fuels for sodium fast reactors*. PhD thesis, Massachusetts Institute of Technology, June 2009. https://tinyurl.com/y72vqvbn.

[17] M. Kato, Y. c, T. Sunaoshi, A. Nelson, and K. McClellan. Thermal expansion measurement of (U,Pu)O_{2-x} in oxygen partial pressure-controlled atmosphere. *Journal of Nuclear Materials*, 469:223–227, 2016.

[18] M. Kato, K. Maeda, T. Ozawa, M. Kashimura, and Y. Kihara. Physical properties and irradiation behavior analysis of Np- and Am-bearing MOX fuels. *Journal of Nuclear Science and Technology*, 48:646–653, 2011.

[19] Masato Kato, Masashi Watanabe, Taku Matsumoto, Shun Hirooka, and Masatoshi Akashi. Oxygen potentials, oxygen diffusion coefficients and defect equilibria of nonstoichiometric (U,Pu)$O_{2\pm x}$. *Journal of Nuclear Materials*, 487:424 – 432, 2017.

[20] H. Kleykamp. The chemical state of LWR high-power rods under irradiation. *Journal of Nuclear Materials*, 84(1):109 – 117, 1979.

[21] H. Kleykamp. The chemical state of the fission products in oxide fuels. *Journal of Nuclear Materials*, 131(2):221 – 246, 1985.

[22] H. Kleykamp. Post-irradiation examinations and composition of the residues from nitric acid dissolution experiments of high-burnup LWR fuel. *Journal of Nuclear Materials*, 171(2):181 – 188, 1990.

[23] Toshiaki Kogai. Modelling of fission gas release and gaseous swelling of light water reactor fuels. *Journal of Nuclear Materials*, 244(2):131 – 140, 1997.

[24] Yang-Hyun Koo, Byung-Ho Lee, Jin-Sik Cheon, and Dong-Seong Sohn. Modeling and parametric studies of the effect of inhomogeneity on fission gas release in LWR MOX fuel. *Annals of Nuclear Energy*, 29(3):271 – 286, 2002.

[25] W. J. Lackey, F. J. Homan, and A. R. Olsen. Porosity and actinide redistribution during irradiation of (U,Pu)O_2. *Nuclear Technology*, 16:120–142, October 1972.

[26] K. Lassmann. The oxired model for redistribution of oxygen in nonstoichiometric uranium-plutonium oxides. *Journal of Nuclear Materials*, 150(1):10 – 16, 1987.

[27] K. Maeda, K. Katsuyama, Y. Ikusawa, and S. Maeda. Short-term irradiation behavior of low-density americium-doped uranium-plutonium mixed oxide fuels irradiated in a fast reactor. *Journal of Nuclear Materials*, 416(1–2):158–165, September 2011.

[28] Koji Maeda, Kozo Katsuyama, and Takeo Asaga. Fission gas release in FBR MOX fuel irradiated to high burnup. *Journal of Nuclear Materials*, 346(2):244 – 252, 2005.

[29] Kenneth C. Mills. *Recommended Values of Thermophysical Properties for Selected Commercial Alloys*. Woodhead Publishing, 2002.

[30] F. A. Nichols. Theory of columnar grain growth and central void formation in oxide fuel rods. *Journal of Nuclear Materials*, 22(2):214–222, May 1967.

[31] M. Niffenegger and K. Reichlin. The proper use of thermal expansion coefficients in finite element calculations. *Nuclear Engineering and Design*, 243:356–359, 2012.

[32] Stephen Novascone, Pavel Medvedev, John W. Peterson, Yongfeng Zhang, and Jason Hales. Modeling porosity migration in LWR and fast reactor MOX fuel using the finite element method. *Journal of Nuclear Materials*, 508:226 – 236, 2018.

[33] D. R. Olander. *Fundamental aspects of nuclear reactor fuel elements*. Technical Information Center, Energy Research and Development Administration, 1976.

[34] T. Ozawa and T. Abe. Development and verifications of fast reactor fuel design code CEPTAR. *Nuclear Technology*, 156:39–55, 2006.

[35] Riley Parrish and Assel Aitkaliyeva. A review of microstructural features in fast reactor mixed oxide fuels. *Journal of Nuclear Materials*, 510:644 – 660, 2018.

[36] Giovanni Pastore, Lelio Luzzi, Valentino Di Marcello, and Paul Van Uffelen. Physics-based modelling of fission gas swelling and release in UO_2 applied to integral fuel rod analysis. *Nuclear Engineering and Design*, 256:75 – 86, 2013.

[37] Giovanni Pastore, L.P. Swiler, J.D. Hales, S.R. Novascone, D.M. Perez, B.W. Spencer, L. Luzzi, P. Van Uffelen, and R.L. Williamson. Uncertainty and sensitivity analysis of fission gas behavior in engineering-scale fuel modeling. *Journal of Nuclear Materials*, 456:398 – 408, 2015.

[38] C. Sari and G. Schumacher. Oxygen redistribution in fast reactor oxide fuel. *Journal of Nuclear Materials*, 61(2):192 – 202, 1976.

[39] I. Sato, K. Katsuyama, and Y. Arai. Fission gases and helium gas behavior in irradiated mixed oxide fuel pin. *Journal of Nuclear Materials*, 416:151–157, 2011.

[40] P. F. Sens. The kinetics of pore movement in UO_2 fuel rods. *Journal of Nuclear Materials*, 43:293–307, 1972.

[41] T. Shimada, T. Itaki, and Y. Nara. Operational experience of experimental fast reactor JOYO driver fuel, May 1989.

[42] M. V. Speight. A calculation on the migration of fission gas in material exhibiting precipitation and re-solution of gas atoms under irradiation. *Nuclear Science and Engineering*, 37(2):180–185, 1969.

[43] M. V. Speight and W. B. Beeré. Vacancy potential and void growth on grain boundaries. In *Metal Science*, volume 9, page 131–140, 1975.

[44] J. Spino and P. Peerani. Oxygen stoichiometry shift of irradiated LWR-fuels at high burn-ups: Review of data and alternative interpretation of recently published results. *Journal of Nuclear Materials*, 375(1):8 – 25, 2008.

[45] Melissa Teague, Michael Tonks, and Stephen Novascone. Microstructural modeling of thermal conductivity of high burn-up mixed oxide fuel. *Journal of Nuclear Materials*, 444(1):161 – 169, 2014.

[46] J.A. Turnbull, C.A. Friskney, J.R. Findlay, F.A. Johnson, and A.J. Walter. The diffusion coefficients of gaseous and volatile species during the irradiation of uranium dioxide. *Journal of Nuclear Materials*, 107(2):168 – 184, 1982.

[47] I. W. Vance and P. C. Millet. Phase-field simulations of pore migration and morphology change in thermal gradients. *Journal of Nuclear Materials*, 490:299–304, July 2017.

[48] R.J White. The development of grain-face porosity in irradiated oxide fuel. *Journal of Nuclear Materials*, 325(1):61 – 77, 2004.

[49] R.J. White and M.O. Tucker. A new fission-gas release model. *Journal of Nuclear Materials*, 118(1):1 – 38, 1983.

[50] R. L. Williamson, J. D. Hales, S. R. Novascone, M. R. Tonks, D. R. Gaston, C. J. Permann, D. Andrš, and R. C. Martineau. Multidimensional multiphysics simulation of nuclear fuel behavior. *Journal of Nuclear Materials*, 423(1–3):149–163, 2012.

[51] N. Yamanouchi, M. Tamura, H. Hayakawa, and T. Kondo. Accumulation of engineering data for practical use of reduced activation ferritic steel: 8%Cr-2%W-0.2%V-0.04%Ta-Fe. *Journal of Nuclear Materials*, 191–194:822–826, 1992.